UNIVERSITY OF CALIFORNIA, SAN DIEGO

Green's Function Analysis of Periodic Structures in Computational Electromagnetics

A dissertation submitted in partial satisfaction of the requirements

for the degree Doctor of Philosophy

in

Physics

by

Derek Van Orden

Committee in charge

Professor Vitaliy Lomakin, Chair
Professor Daniel Arovas, Co-Chair
Professor Yeshaiahu Fainman
Professor Michael Fogler
Professor Elizabeth Jenkins

2011

The dissertation of Derek Van Orden is approved, and it is acceptable in quality and form for publication on microfilm and electronically:

_____

_____

_____

_____

Co-Chair

_____

Chair

University of California, San Diego

2011

Dedication

This dissertation represents the bulk of my research work over the last four and a half years in Professor Lomakin's Computational Electromagnetics lab. Beyond the doctoral degree, it represents my evolution from an undergraduate student, who is fed problems to solve in courses, towards one who seeks out and tackles new, perhaps insurmountable problems within the research community. This transition has not only advanced my abilities but given me a newfound confidence in them. At each stage, this research work has been immensely interesting, providing new insights, challenges, and breakthroughs right to the end. I wish everyone could have this much fun in graduate school.

I 'd like to thanks my labmates for numerous fruitful discussion on topics ranging from numerical analysis to magnetic exchange interactions. Having been the first grad student in the lab, your arrivals were a welcome change.

I owe much to my parents, both doctors themselves, for their unflagging support and guidance during the various bumps along this road. From making me learn my times tables to paying my way through college, this would not have been possible without them.

Above all, this is dedicated to my advisor, Vitaliy Lomakin. Without his patience and training, especially during my first year and a half or so in the lab, there is no way I would have been able to accomplish as much as I did. Most of my publications began with great ideas he suggested, and were advanced with the help of his exceptional knowledge of electromagnetics and computation. It is a privilege to be his first graduated student, and it is with some regret that I finally move on. Thanks so much; I know that everything I learned here will serve me well in the future.

Table of Contents

List of Figures

Acknowledgements

The text of Chapter 3, in part, is a reprint of the material as it appears in the following publication: D. Van Orden and V. Lomakin, “Rapidly Convergent Representations for 2D and 3D Green’s functions for a Linear Periodic Array of Dipole Sources,” IEEE Transactions on Antennas and Propagation, Vol. 57, 1973-1984 (2009). The dissertation author was the primary researcher and the co-author listed in this publication directed and supervised the research which forms the basis for this chapter.

The text of Chapter 4, in part, is a reprint of the material as it appears in the following publication: D. Van Orden and V. Lomakin, “Rapidly convergent representation for the periodic Green's function of a linear array in layered media” accepted for publication in IEEE transactions on Antennas and Propagation, August 2011. The dissertation author was the primary researcher and the co-author listed in this publication directed and supervised the research which forms the basis for this chapter.

The text of Chapter 5 is, in part, a reprint of the material as it appears in the following publication: D. Van Orden and V. Lomakin, “Fundamental electromagnetic properties of twisted linear arrays” accepted for publication in IEEE Transactions on Antennas and Propagation, Vol. 59, 2824-2833 (2011). The dissertation author was the primary researcher and the co-author listed in this publication directed and supervised the research which forms the basis for this chapter.

Vita

2004	Bachelor of Science, Applied Physics, Rice University, Houston
2006	Master of Science, Physics, University of California, San Diego
2011	Doctor of Philosophy, Physics, University of California, San Diego

Publications

D. Van Orden and V. Lomakin, “Rapidly convergent representation for the periodic Green’s function of a linear array in layered media.” IEEE Transactions on Antennas and Propagation, accepted for publication August 2011.

D. Van Orden and V. Lomakin, “Fundamental Electromagnetic Properties of Twisted Periodic Arrays”, IEEE Transactions on Antennas and Propagation, Vol. 59, 2824-2833 (2011)

S. Li, D. Van Orden, and V. Lomakin. “Fast Periodic Interpolation Method for Periodic Unit Cell Problems.”, IEEE Transactions on Antennas and Propagation, Vol. 58, 4005-4014 (2010)

D. Van Orden, Y. Fainman, and V. Lomakin, "Twisted chains of resonant particles: Optical polarization control, waveguidance, and radiation”, Optics Letters, Vol. 35, 2579-2581 (2010).

D. Van Orden and V. Lomakin, “Rapidly Convergent Representations for 2D and 3D Green’s functions for a Linear Periodic Array of Dipole Sources.” IEEE Transactions on Antennas and Propagation, Vol. 57, 1973-1984 (2009)

D. Van Orden, Y. Fainman, and V. Lomakin, "Optical waves on nanoparticle chains coupled with surfaces." Optics Letters, Vol. 34, 422-424 (2009)

L. Feng, D. Van Orden, A. Maxim, Q. Wang, Y. Chen, V. Lomakin, and Y. Fainman, “Nanoscale optical field localization by resonantly focused plasmons.” Optics Express, Vol. 17, Issue 6, pp. 4824-4832 (2009)

Fields of Study

Major field: Physics

Studies in Computational Electromagnetics
Professor Vitaliy Lomakin

ABSTRACT OF THE DISSERTATION

Green's Function Analysis of Periodic Structures in Computational Electromagnetics

by

Derek Van Orden

Doctor of Philosophy in Physics

University of California, San Diego, 2011

Professor Daniel Arovas, Co-Chair
Professor Vitaliy Lomakin, Chair

Periodic structures are used widely in electromagnetic devices, including filters, waveguiding structures, and antennas. Their electromagnetic properties may be analyzed computationally by solving an integral equation, in which an unknown equivalent current distribution in a single unit cell is convolved with a periodic Green's function that accounts for the system's boundary conditions. Fast computation of the periodic Green's function is therefore essential to achieve high accuracy solutions of complicated periodic structures, including analysis of modal wave propagation and scattering from external sources.

This dissertation first presents alternative spectral representations of the periodic Green's function of the Helmholtz equation for cases of linear periodic systems in 2D and 3D free space and near planarly layered media. Although there exist multiple representations of the periodic Green's function, most are not efficient in the important case where the fields are observed near the array axis. We present spectral-spatial representations for rapid calculation of the periodic Green's functions for linear periodic arrays of current sources residing in free space as well as near a planarly layered medium. They are based on the integral expansion of the periodic Green's functions in terms of the spectral parameters transverse to the array axis. These schemes are important for the rapid computation of the interaction among unit cells of a periodic array, and, by extension, the complex dispersion relations of guided waves. Extensions of this approach to planar periodic structures are discussed.

With these computation tools established, we study the traveling wave properties of linear resonant arrays placed near surfaces, and examine the coupling mechanisms that lead to radiation into guided waves supported by the surface. This behavior is especially important to understand the properties of periodic structures printed on dielectric substrates, such as periodic microstrip lines and leaky wave antennas. We proceed to analyze "twisted" linear periodic arrays, consisting of particles that are sequentially and discretely rotated about the array axis by a constant angle. Such periodic structures support two transverse wave modes with distinct polarization and radiation behavior, which couple to circularly polarized sources with opposite handedness. These structures offer a new dimension of polarization control to linear waveguiding structures.

Chapter 1 Introduction

1.1 Motivation

The objective of computational electromagnetics is to solve Maxwell's equations with programmable computers in order to study the interaction of electromagnetic waves with complex structures and media. This field of study originated in the 1960s with the advent of digital computers, and was motivated largely by the military defense industry for the purposes developing of radar, antenna, and, later, stealth technology. Since then, however, the applications of computation work have grown enormously, and include wireless communications, high-speed circuits, optical and photonic devices, and even medical diagnosis and treatment. As the applications for electromagnetic systems have grown, so too has the need for advanced numerical techniques that are capable of fast, high accuracy analysis of complex systems. Computational analysis is particularly challenging for the field of Electromagnetics, which is governed by vector differential equations and boundary conditions. As a result, computer memory requirements and long run times are a limiting factor in the simulation of large-scale structures. Acceleration schemes allowing for more efficient analysis are therefore a subject of continued interest in multiple engineering disciplines.

Periodic electromagnetic structures play an important role in many microwave and optical devices, including gratings, antennas, filters, and waveguiding structures. Simulation tools for periodic systems have become even more important with the recent interest in artificial metamaterial structures, including electromagnetic band gap materials.

Linear periodic arrays, in particular, are useful for their ability to support guided wave modes, which allows for efficient transmission of electromagnetic signals, and also radiating leaky-wave modes, which may be exploited to construct antennas in the microwave regime or far-field couplers in optics. Because of their wide ranging applications, there is a strong interest in efficient simulation tools for periodic electromagnetic systems, as well as explorations of their fundamental radiation and propagation behavior.

1.2 Review of Computation Methods in Electromagnetics

This section reviews the most commonly used "full-wave" numerical approaches used in computational electromagnetics. By full-wave solvers, we mean they solve Maxwell's equations without any simplifying approximations. This is to be distinguished, for example, from computations based on quasi-static approximations, where the wavelength λ is large compared to a structure's length scale, and ray and diffraction approaches, which are used in the short wavelength limit. Full wave solvers are required for accurate solutions a structure's length scale is on the same order as the wavelength, such as Mie scattering or antenna radiation. In this situation, all terms in Maxwell's equations, as well as the boundary conditions, must be included without simplification for accurate solutions.

There are three widely used full-wave computation methods in electromagnetics: the finite difference time domain method (FDTD) and the finite element method (FEM), both of which are differential methods, and the method of moments (MoM), an integral

equation formulation. All three methods had their basic mathematical foundations established before the advent of digital computers, and all three have been in continued use and development since the 1960s. The fact that three completely different approaches have coexisted for so long indicates that they are well suited to different classes of problems. A brief review of these methods is important to understanding the role of Green's function methods in computational electromagnetics.

A. Differential Methods

FDTD and FEM both involve closing the system of interest in a finite computational domain and finding the fields on a set of discrete grid points, called the mesh. The length scale of each mesh element is generally taken to be at most $\lambda / 10$ to properly account for the field variations, and is often chosen as $\lambda / 20$ or smaller for high-accuracy solutions. FDTD is a finite difference solver that solves Maxwell's equations directly in differential form by approximating spatial derivatives with finite differences on a uniform rectangular grid. The fields are then evolved in discrete time steps, with boundary conditions enforced at each material interface. It is the only widely used method for time domain problems (and, by extension, nonlinear systems). More than any other method, its limitations are well understood. The constraint of a uniform mesh makes evaluation inefficient for large systems with small geometrical features. The discretization introduces artificial dispersion, and the rectangular mesh cannot model curved surfaces well. Finally, the grid size and time steps must satisfy a certain ratio to ensure stability, making it inefficient for low-frequency systems. However, of the three

methods, it is by far the simplest to implement and parallelize, and remains a powerful method widely used in commercial solvers.

FEM is typically used for frequency domain problems, in which all field quantities are assumed to a have sinusoidal time dependence. FEM meshes the computational domain into (typically) triangular or tetrahedral elements for 2D and 3D systems, respectively, and is well suited to modeling of irregular structures. Unlike FDTD, the elements need not be equal in size, and may be tailored to the structure's expected field variations for greater computational efficiency. FEM works by expanding the unknown field quantities into basis functions within each element. Maxwell's equations are then solved as an equivalent variational, boundary value problem: the set of coefficients for the expansion functions that minimizes an appropriate functional gives the best approximation for the true fields. These coefficients are solved by inverting a sparse, banded matrix equation, either directly or iteratively.

Both FDTD and FEM are limited by the fact that the entire computational domain is meshed, making them inefficient for systems with large computational domains compared to the wavelength (i.e. electrically large separation between scatterers or surface problems). Furthermore, "open" problems, in which the system is exposed to free-space, require special handling. In such systems, careful consideration must be made to formulate mixed boundary conditions at the domain edges that simulate radiation into free space. Indeed, these boundary conditions require increasing the computational domain beyond the structure of interest, and with it the computational cost of evaluation.

B. Integral Equation Methods

The Method of Moments is an integral equation formulation based on surface and volume equivalence principles. In particular, the surface equivalence principle states that scattering from a homogenous object may be modeled as the radiation from an equivalent current distribution on the object's surface. For dielectric objects these surface currents are entirely fictitious, and may include both electric and magnetic currents, while for a perfect electrical conductor (PEC) these currents are the actual, physical induced currents. As a simple example, consider an excitation field $\mathbf{E}_{inc}(\mathbf{r})$ incident on a PEC scatterer. The boundary condition requires the tangential electric field to be zero at the object surface S. The induced surface currents $\mathbf{J}_s(\mathbf{r})$ must then act to cancel out the tangential component of $\mathbf{E}_{inc}(\mathbf{r})$ on S. That is,

$$-\hat{n} \times \mathbf{E}_{inc}(\mathbf{r}) = \hat{n} \times \int \mathbf{G}(\mathbf{r}, \mathbf{r}') \cdot \mathbf{J}_s(\mathbf{r}') dS, \quad \mathbf{r} \in S \tag{1.1}$$

where $\mathbf{G}(\mathbf{r}, \mathbf{r}')$ is the dyadic Green's function that gives the electric field resulting from the currents $\mathbf{J}_s(\mathbf{r}')$, and $\hat{n}$ is the unit vector normal to the surface. The objective of an integral equation solver is to find these surface currents. This formulation is known as the electric field integral equation (EFIE); an alternative representation can be derived based on the magnetic field (MFIE), but it is limited to closed surfaces and is not as widely used.

The Method of Moments works by expanding the unknown currents into a set of vector basis functions $\mathbf{J}_n(\mathbf{r})$ with expansion coefficients I_n. One can then take the dot

product of $\mathbf{J}_m(\mathbf{r})$ with each side of Eq. (1.1) and, using orthogonality of the basis functions, set up a matrix equation for the expansion coefficients I_n:

$$\mathbf{V} = \mathbf{Z} \cdot \mathbf{I}$$

$$V_m = -\int \mathbf{E}_{inc}(\mathbf{r}) \cdot \mathbf{J}_m(\mathbf{r}) dS \tag{1.2}$$

$$Z_{mn} = \int dS\, \mathbf{J}_m(\mathbf{r}) \cdot \int dS'\, \mathbf{G}(\mathbf{r}, \mathbf{r}') \cdot \mathbf{J}_n(\mathbf{r}')$$

The current expansion coefficients are found by inverting this system of equations, either directly or by iterative methods. It should be noted that MoM is not typically set up as in this simple example. In practice, the equation for the matrix elements Z_{mn} is reformulated into a "mixed potential" form, using Green's theorem and integration by parts, to avoid problematic singularities. Also, it is generally not possible to find a set of basis functions to cover the entire surface. Practically, the surfaces are meshed so the currents may be expanded into subdomain basis functions within each mesh element. For dielectric scatterers one must include magnetic currents as well. The basic approach, however, remains essentially the same. Once the equivalent surface currents are known, they may be convolved with the Green's function to solve for the fields anywhere in space.

Efficient implementation of MoM is complicated, and presents some technical challenges. The impedance matrix $\mathbf{Z}$ is often poorly conditioned, which slows down the computations greatly. Complicated preconditioners may have to be devised for large scale systems. Nonetheless, good implementations show fast convergence, and are capable of very high accuracy. A big advantage of this approach is that, for homogenous

media, only the object surfaces need be meshed, reducing the number of unknowns greatly for electrically large or geometrically complex systems. Furthermore, the boundary conditions are implicitly and exactly accounted for through the Green's function, so the radiation conditions characterizing open problems require no special modifications. As such, this method avoids phase errors, which are characteristic of differential equation methods. Importantly, problems with large "white spaces", such as the interaction between antennas separated far apart, are easily simulated. In addition, various complex backgrounds, such as layered media and waveguides, can be included in the Green's function, allowing the surface boundaries to be excluded from the problem discretization. For this reason this approach is widely used for antenna and scattering problems, where the surface currents on conductors and the far-field radiation are of interest.

It is within the context of MoM formulations that efficient Green's function representations are important. As the kernel of the integral equation, they figure largely into the cost of filling the impedance matrix for certain types of boundary conditions. The systems of interest for which a Green's function may be formulated include waveguides and resonators with Cartesian and cylindrical symmetry, planarly layered media, and periodic systems. A Green's function that accounts for the boundary conditions in these cases greatly reduces the number of unknown current elements. For electromagnetic structures near surfaces, for example, the reflections may be accounted for through the Green's function, so the surface layers need not be meshed as it is included explicitly in the integral equation formulation. In the case of periodic systems, a periodic Green's

function reduces the evaluation of currents to only a single unit cell. Furthermore, the interaction of a periodic system with a nonperiodic object, modeled as an equivalent surface current source, may be found using an “array-scanning” technique, in which the Green’s function is convolved with a plane wave expansion of the localized source field [1]. The computational cost of this technique method is often dominated by the periodic Green’s function evaluation, so fast evaluations are highly desirable.

Finally, Green’s functions methods allow a level of physical insight into physical systems that FEM and FDTD cannot match. As will be shown, a Green’s function may often be separated into contributions from the current source and scattering from different resonant modes supported by the system. In this way the contribution of different wave types may be considered independently, and their contribution to the total fields better understood. Green's functions may furthermore be used to find asymptotic approximations that facilitate physical understanding of field behavior in important limiting cases.

1.3 Dissertation organization

This dissertation has two main objectives. The first is to develop efficient representations of the periodic Green’s function for linear arrays in free space and near surfaces. The second is to use these methods to analyze the underlying physics of certain classes of resonant arrays. Chapter 2 presents a review of the basic properties of linear periodic structures in frequency domain electromagnetics. Although familiar to some readers, it establishes terminology and the basic methods of analysis that are used throughout the dissertation.

Chapter 3 presents a method for rapidly computing the periodic Green's function for a linear array of short dipole current sources in free-space. It is based on a spectral expansion of the Green's function into the direction transverse to the periodicity direction, and is formulated as a spectral integral. This integral is regularized for fast computation. This alternative representation is efficient for the important case where the fields are observed on or near the array axis, where traditional spatial and spectral representations of the Green's function break down. This case is necessary to analyze the interaction of a unit cell with all the other array elements, and is essential for scattering and propagation analysis. Extensions of this approach to doubly periodic arrays, which have periodicity in two directions, is discussed. The Green's function representations are used to investigate electromagnetic properties of a linear array of small metallic particles at optical frequencies.

Chapter 4 extends the work of chapter 3 to the case of a linear array of current sources near a planarly layered medium. This is case is encountered in the analysis of resonant arrays on dielectric substrates, such as periodic microstrip lines, antenna arrays printed on circuit boards, or arrays on a substrate for optical waveguidance and radiation. The Green's function for the reflected fields is represented as a spectral integral, as before, plus a series which accounts for the discrete spectrum of eigenmodes supported by the surface medium. This method is well suited to finding the reflected fields near the array and surface. This chapter further analyzes the propagation and radiation mechanisms of a resonant periodic array near a dielectric slab. It is shown that this structure typically supports two general types of traveling wave modes: one that is

confined to the array, and the other that radiates into the guided waves supported by the slab medium. The latter is mediated primarily by free-space interactions among resonant elements, while the former is mediated by the surface. This behavior allows greater understanding of the way in which periodic arrays leak energy into substrates.

Chapter 5 presents a new type of linear periodic array, one in which each element is sequentially rotated about the array axis relative to the previous element. Such "twisted" arrays are shown to support two distinct transverse wave modes that are efficiently excited by circularly polarized sources of opposite handedness. One is generally a confined mode, while the other will radiate for small to moderate twist rates. A Green's function is derived that accounts for the unique periodicity conditions for a twisted array of point current sources, and it is used to find the mode propagation constants of twisted nanoparticle arrays. Twisted arrays of half-wave dipoles are also simulated to show possible applications as leaky-wave antennas. This class of structure offers a dimension of polarization control for waveguiding and radiating periodic structures.

Chapter 6 summarizes the findings of the dissertation.

Chapter 2 Review: Green's Functions and Periodic Structures in Electromagnetics

2.1 Frequency Domain Electromagnetics

The fundamental assumption of frequency domain electromagnetics is that all fields and currents have the time dependence $e^{-i\omega t}$, where ω is the angular frequency of the source. This assumption is valid for all linear systems: if a structure is excited by a source with harmonic time dependence, all scattered fields and induced currents vary with the same frequency. Field vectors and currents are then represented as complex phasors that include the amplitude and phase of the real physical quantities, with the $e^{-i\omega t}$ factor suppressed. This convention is used throughout the dissertation. Maxwell's equations are then reduced to a set of partial differential equations with respect to spatial coordinates only:

$$\begin{aligned} \nabla \cdot \mathbf{E} &= \rho \,/\, \varepsilon \\ \nabla \cdot \mathbf{B} &= 0 \\ \nabla \times \mathbf{E} &= i\omega\mu\mathbf{H} \\ \nabla \times \mathbf{H} &= -i\omega\varepsilon\mathbf{E} + \mathbf{J} \end{aligned} \tag{2.1}$$

Note that the permittivity may be frequency dependent and complex valued. It is emphasized that the current density $\mathbf{J}$ and charge density ρ represent impressed current and charge sources.

With this formulation, a wave equation for the electric field may be expressed as

$$\nabla^2\mathbf{E} + \omega^2\varepsilon\mu\mathbf{E} = -i\omega\mu\mathbf{J} + \nabla\rho \,/\, \varepsilon \tag{2.2}$$

Using the continuity equation $\nabla \cdot \mathbf{J} - i\omega\rho = 0$, along with the definitions for the wave impedance $\eta = \sqrt{\mu / \varepsilon}$ and free-space wavenumber $k_0 = \omega\sqrt{\varepsilon\mu}$, the this may be rewritten as

$$\nabla^2 \mathbf{E} + k_0^2 \mathbf{E} = -ik_0\eta\left(\mathbf{I} + \frac{\nabla\nabla}{k_0^2}\right)\mathbf{J} \tag{2.3}$$

This is recognized as the Helmholtz equation. With an appropriate set of boundary conditions, its solution yields the complete fields in and around a structure resulting from a current source excitation.

2.2 Green's Functions in Electromagnetics

The scalar Green's function $G(\mathbf{r}, \mathbf{r}')$ that is used in MoM implementations is typically defined as the solution to

$$\nabla^2 G + k_0^2 G = -\delta(\mathbf{r} - \mathbf{r}') \tag{2.4}$$

To simplify the notation, we set $\mathbf{r}' = \mathbf{0}$ throughout the dissertation, without loss of generality. For most integral equation formulations of MoM, only $G(\mathbf{r})$ and its gradient are required to solve for the unknown current distribution. In cases where the Green's function depends on the wave polarization, as occurs for a current source near a surface, a full dyadic Green's function may be necessary to find the electric field resulting from all possible current orientations. The scattered electric field from a short dipole with dipole moment $\mathbf{p}$ may be found as $\mathbf{E}(\mathbf{r}) = \mathbf{G}(\mathbf{r}) \cdot \mathbf{p}$, where

$$\mathbf{G}(\mathbf{r}) = \frac{1}{4\pi\varepsilon}(k_0^2\mathbf{I} + \nabla\nabla)G(\mathbf{r}) \tag{2.5}$$

is the dyadic Green's function. The dyadic Green's function is also used to find the scattering from electrically small particles, which may be modeled as point dipole sources in response to an incident field. It is noted that the dyadic Green's function is defined here as the response to the dipole moment of a small current source, rather than the current density. This convention is used throughout the dissertation.

The solution to Eq. (2.4) for an isolated point source in free space may be found in closed form for two dimensional (2D) and three dimensional (3D) geometries:

$$G_0^{2D}(\boldsymbol{\rho}) = \frac{i}{4} H_0^{(1)}(k_0 \rho), \quad G_0^{3D}(\mathbf{r}) = \frac{e^{ik_0 r}}{4\pi r}, \tag{2.6}$$

where $H_0^{(1)}$ denotes the zeroth order Hankel function of the first kind. (Throughout the dissertation, the superscripts $2D$ and $3D$ denote two and three dimensional geometries, respectively.) The solutions are chosen to satisfy the outgoing "radiation" boundary conditions for open problems, which require an outward propagating wave far from the source. Although the free-space Green's function is useful for many problems, alternate Green's may be developed for more complicated environments, such as inside waveguides or near surfaces.

2.3 Periodic Boundary Conditions

In many areas of physics, the analysis of large, but finite periodic systems may be simplified by studying a single unit cell and applying periodic boundary conditions. This approach, which is equivalent to studying an infinite periodic system, often yields excellent approximations to the true solution. Furthermore, exact treatments of finite systems are frequently too computationally costly to be practical. For the analysis of

wave propagation in periodic structures, periodic boundary conditions also permit finding the dispersion relations of traveling wave modes, as will be shown in the next section.

In electromagnetics, the periodicity condition for a linear (1D) array requires that the currents and field quantities in each unit cell differ only by a constant phase shift. For an array oriented along the z axis with spacing L, the periodic Green's function must satisfy

$$G(\mathbf{r} + nL\hat{\mathbf{z}}) = e^{ik_{z0}nL} G(\mathbf{r}) \tag{2.7}$$

where n is an integer that counts the unit cells, and k_{z0} is a parameter that introduces a sequential phase shift to each unit cell. This phase shift may be introduced, for example, by a plane wave with incident angle θ with respect to the z axis, in which case $k_{z0} = k_0 \cos(\theta)$.

A linear periodic structure with period L also has a periodic spectrum, with angular period $2\pi / L$, with respect to the longitudinal spectral parameter k_z. This may be demonstrated using the Poisson summation formula, which relates a spatial series of some function $f(z)$ to a spectral series of its Fourier transform $\tilde{f}(k_z)$:

$$\sum_{n=-\infty}^{\infty} f(nL) = \frac{1}{L} \sum_{m=-\infty}^{\infty} \tilde{f}\left(\frac{m}{L}\right). \tag{2.8}$$

An important consequence of this spectral periodicity is that for each propagation wavenumber β that solves the source-free field equations, there exist an infinite number of solutions $\beta_m = \beta + 2\pi m / L$. These solutions are called diffraction modes, or Floquet modes. Equation (2.8) indicates that the fields resulting from a periodic system may be

thought of either as the spatial sum of contributions from each unit cell, or, alternatively, a spectral sum of contributions from each Floquet mode.

2.4 Traveling Waves on Periodic Structures

Traveling wave modes are a leading subject of interest in the study of periodic structures. They represent eigenmode solutions for periodic systems, which solve the field equations in the absence of external sources. Their field distributions therefore satisfy both the homogenous wave equation and periodicity conditions. In the microwave regime, arrays of metallic half-wavelength (resonant) dipoles support traveling waves that are bound to the array and propagate without radiation loss. Such arrays (tapered and truncated) are used as Yagi-Uda antennas radiating endfire beams along the periodicity axis [2]. In the optical regime similar phenomena are supported by arrays of plasmonic nanoparticles that are resonant even on a deeply subwavelength scale, thus enabling subwavelength particle array waveguides. Properly tuning the particle properties, distribution, and ambient environment allows controlling an array's waveguiding and radiation properties [3-8]. Computing the dispersion relations is essential to understanding a wave mode's propagation and radiation behavior, and also to finding its modal field distribution and currents.

Consider a linear array of particles that are sufficiently small compared to the wavelength λ that they may be treated as point dipole sources through their polarizability tensor $\boldsymbol{\alpha}$. The periodicity requires that the dipole moment $\mathbf{p}_n$ of the n^{th} particle, centered at $\mathbf{r}_n = nL\hat{\mathbf{z}}$, satisfies $\mathbf{p}_n e^{ik_{z0}L} = \mathbf{p}_{n+1}$. In addition, traveling wave modes

supported by the array must satisfy the electromagnetic equations with no external sources. This occurs only for certain discrete values of k_{z0}, denoted by β, which represent the mode propagation wavenumbers. These values of β are found by setting up and solving a self-consistent equation for the zeroth dipole moment $\mathbf{p}_0$, which is given by

$$\mathbf{p}_0 = \boldsymbol{\alpha} \cdot \mathbf{E}(\mathbf{0}) \tag{2.9}$$

where $\mathbf{E}(\mathbf{r})$ is the electric field resulting from all the other particles in the array. It may be found using the periodic Green's function, with the field contribution of $\mathbf{p}_0$ itself subtracted :

$$\mathbf{E}(\mathbf{0}) = \left(\mathbf{G}(\mathbf{0}, L, k_0, k_{z0}) - \mathbf{G}_0(\mathbf{0}, k_0)\right) \cdot \mathbf{p}_0 \tag{2.10}$$

Here the nonperiodic Green's function $\mathbf{G}_0(\mathbf{0}, k_0)$ represents the "self-term" that must be excluded, since the particle at the origin cannot interact with itself. (For clarity the Green's functions are written here as functions of all dependencies.) Combining Eqs. (2.9) and (2.10) yields the following self-consistent dispersion equation:

$$\det\left(\mathbf{G}(\mathbf{0}, L, k_0, k_{z0}) - \mathbf{G}_0(\mathbf{0}, k_0) - \boldsymbol{\alpha}^{-1}\right) = 0 \tag{2.11}$$

Solving this implicit equation for k_{z0} yields the modes dispersion relations, which give the dependence of the (generally complex) modal wavenumbers β on the free-space wavenumber k_0.

This special case of small scatterers, which applies to nanoparticles in optics [3] or short dipoles loaded with circuit elements in the microwave regime [9], permits

finding simple expressions for guided and radiated fields. For this reason it is considered throughout the dissertation to show general properties of different classes of resonant linear arrays. To find the dispersion for the more general case of large scatterers, one must set up an integral equation, as in Eq. (1.2) , and set the vector **V** to be zero. The propagation wavenumbers β of traveling wave modes are precisely those values of k_{z0} for which the impedance matrix **Z** has zero determinant. In this case and in Eq. (2.11), the dispersion equation may be solved iteratively e.g. using variations of Newton's method.

The solution to the dispersion equation for linear structures in three dimensional space has three independent solutions, corresponding to one longitudinal and two transverse dimensions with respect to the periodicity axis. In each case, a wave mode's phase behaves as $e^{i\beta z + ik_\rho \rho}$, where $k_\rho = \sqrt{k_0^2 - \beta^2}$ is the wavenumber component transverse to the array. Forward propagating modes have values of β with a positive real part. A corresponding positive imaginary part indicates dissipative or radiative losses in this direction, while for lossless modes β is purely real.

Traveling wave modes may be separated into two general classes. Those for which the mode wavenumber β and its higher diffraction orders satisfy $\left|\mathrm{Re}\{\beta_m\}\right| > k_0$ for all m do not radiate out of the array, and are called slow waves, or guided waves. Their fields are confined to the array, and decay exponentially away from the array axis. For most types of resonant arrays, β is very close to k_0 , except when excited very close to the resonance. We will refer to these systems as to "dense" arrays because the spacing

is small compared to the wavelength, so that the spectral spacing of diffraction modes $2\pi / L$ is large, and no β_m are found within the "light lines" between $-k_0$ and k_0. The second class of traveling wave modes satisfy $\left|\mathrm{Re}\{\beta_m\}\right| < k_0$ for some m radiate into free space, and are called fast waves, or leaky waves. They are supported by "sparse" arrays with a relatively large spacing. The angle of radiation θ_{rad} satisfies the phase-matching condition $\mathrm{Re}\{\beta_m\} = k_0 \cos(\theta_{rad})$. This radiation may be exploited to build antennas in the microwave regime, or diffraction gratings in optics. Considering the problem in reverse, this property allows far-field signals, such as an incident plane wave, to be coupled to the slow wave components in a periodic array.

As will be shown in chapter 3, the periodic Green's function has an infinite number of square-root branch cuts in the complex k_{z0} plane, resulting from the dependence on the transverse wavenumber component $k_{\rho m} = \sqrt{k_0^2 - \beta_m^2}$ for each Floquet mode. It can be shown that for small periodicities, for which no Floquet modes are radiating (i.e. $|\mathrm{Re}\{\beta_m\}| > k_0$), physical solutions correspond to values of β on the top Riemann sheet which is defined so that $k_{\rho m}$ has a positive imaginary part for all m. This condition enforces exponential decay away from the array, as required for slow waves. For larger periodicities, however, one or more of the Floquet modes become propagating, with $-k_0 < \mathrm{Re}\{\beta_m\} < k_0$ and the physical solutions are leaky waves that may correspond to β on an alternate Riemann sheet, with $\mathrm{Im}\{k_{\rho m}\} < 0$ for a small number of Floquet modes m. The fields for these leaky wave modes show exponential increase

transverse to the array. In order for them to be physical, they are observable only for observation angles (relative to the periodicity axis) at which the longitudinal decay rate along the array equals or exceeds the exponential increase out of the array [10].

Finding the dispersion relations for periodic systems requires a Green's function representation that can efficiently handle both complex values of k_{z0} and observation points close to and directly on the array axis. It must also be able to handle alternate Riemann sheets in order to find solutions that may reside there. Chapters 3 and 4 present Green's function representations that address these issues for the case of linear periodic arrays in free space and near surfaces.

Chapter 3 Green's Functions for a Linear Periodic Array in Free Space

3.1 Introduction

This chapter presents an alternative representation of the periodic Green's function (PGF) for an array of dipole current sources in two and three dimensional free space. It is well known that representations of PGFs based on direct spatial summations of single source (nonperiodic) Green's functions are extremely slowly convergent, and diverge when the periodicity is defined with a complex phase shift between elements [11]. The convergence can be improved by using spectral summations in terms of Floquet series. However Floquet series representations suffer from slow convergence in the important case where the observation point resides near the periodicity axis.

Several approaches have been proposed to accelerate the computation of PGFs. Some are based on spectral and spatial formulations with Poisson's, Kummer's, and Shank's transformations [11-15], which accelerate the original spatial and spectral series representations but do not lead to exponentially rapid convergence, and may be slow in various situations [11-12, 16]. Veysoglu's transformation [11-12, 16-17] and perfectly matched layer (PML) approaches [18-19] do show exponential convergence, but cannot handle complex phase shifts between unit cells, and may suffer from low-frequency breakdown. The Ewald approach, based on Ewald and Poisson's transformations, has been the best overall option for computing the PGF near the periodicity axis. It is fully convergent for complex values of the phase shift parameter, and leads to exponentially convergent series representations. However, it requires double summations, can suffer

high-frequency breakdown, and involves choosing a proper splitting parameter, which may be not straightforward to implement [11-12, 16, 20-29].

In this chapter we introduce a novel method for computing scalar and dyadic PGFs for 2D and 3D problems comprising a 1D periodicity with phase shifted conditions. The method is based on an alternative Green's function spectral expansion transverse to the periodicity axis, with the longitudinal (along the axis) spectral 1D PGF available in closed form. These representations lead to exponential computational convergence for any location near the array axis and for electrically small and large periodicities. Moreover, the introduced series have a clear physical interpretation, being expressed in terms of a small number of direct field contributions, a small number of Floquet modes, and a rapidly convergent integral representing the combined contribution of the remaining sources. Extensions to arrays with periodicity in two dimensions are discussed, which are highly efficient when coupled with Method of Moments solvers for large-scale systems.

3.2 Spectral representations of Green's functions

Consider a 1D periodic array of identical electric dipole sources in free space. The dipoles are arranged along the z axis with spacing L and directed along a general unit vector $\hat{\mathbf{p}}$ (Fig. 3-1). These are linear sources for 2D configurations and point sources for 3D problems. The scalar PGF G^{2D} is a function of the two spatial variables x and z, while G^{3D} depends only on z and $\rho = (x^2 + y^2)^{1/2}$. The symmetry of the problem allows formulations involving separation of variables in the longitudinal (z) and

transverse (ρ or x) directions. The scalar (and thus dyadic) PGFs exhibit the phase shifted periodicity property with respect to the periodicity L as given in Eq. (2.7).

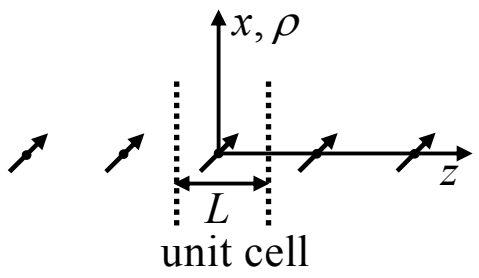

Fig. 3-1 Structure configuration representing a linear periodic array of arbitrarily directed dipole sources.

The periodic Green's function may be represented as an infinite spatial sum of free-space Green's functions, given in Eq. (2.6), taken over all unit cells.

$$G^{2D,3D}(\mathbf{r}) = \sum_{n=-\infty}^{\infty} e^{ik_{z0}nL} G_0^{2D,3D}(\mathbf{r} + nL\hat{\mathbf{z}}) \tag{3.1}$$

For lossless ambient media (i.e. real k_0) the series in Eq. (3.1) converge extremely slowly, and for complex values of k_{z0} they do not converge at all. Therefore, more efficient representations for constructing the PGFs are to be developed.

A. Longitudinal Spectral Expansion

Using separation of variables, the periodic Green's function may be represented as a series in which each term is a product of two functions: a function of z that satisfies the periodicity condition, and an unknown function of ρ or x to be determined:

$$G^{2D}(\mathbf{r}) = \sum_{n=-\infty}^{\infty} f_m^{2D}(x) e^{i\left(k_{z0}+2\pi m/L\right)z}, \quad G^{3D}(\mathbf{r}) = \sum_{n=-\infty}^{\infty} f_m^{3D}(\rho) e^{i\left(k_{z0}+2\pi m/L\right)z} \tag{3.2}$$

These expressions may be inserted into the Helmholtz equation in Eq. (2.4). Using the orthogonality of the exponential term, one may formulate and solve a differential equation for the unknown functions $f_m^{2D}(x)$ and $f_m^{3D}(\rho)$, considering only outward propagating phase behavior. These functions can be shown to be solutions of the Helmholtz equation with the dimensionality reduced by one. The longitudinal expansions become the well-known Floquet series representation:

$$\begin{aligned} G^{2D}(\mathbf{r}) &= \frac{1}{L}\sum_{m=-\infty}^{\infty} \frac{i}{2k_{xm}} e^{ik_{zm}z} e^{ik_{xm}|x|}, \\ G^{3D}(\mathbf{r}) &= \frac{1}{L}\sum_{m=-\infty}^{\infty} e^{ik_{zm}z} \frac{i}{4} H_0^{(1)}(k_{\rho m}\rho), \end{aligned} \tag{3.3}$$

where $k_{zm} = k_{z0} + 2\pi m/L$ and $k_{\{x,\rho\}m} = (k^2 - k_{zm}^2)^{1/2}$ are referred to as the longitudinal and transverse Floquet mode wavenumbers, respectively. In the complex k_{z0} plane, the square root resulting from $k_{\{x,\rho\}m}$ in each term results in an infinite number of branch cuts. The choice of the sign of the square root for each $k_{\{x,\rho\}m}$ depends on the application. In most cases the square root is chosen so that $\mathrm{Im}\{k_{\{x,\rho\}m}\} \geq 0$ for all m, resulting in exponential decay transverse to the array. In this case the PGF is said to be defined on the top Riemann sheet. In other cases, such as the analysis of complex dispersion relations of leaky-wave antennas, one may choose $\mathrm{Im}\{k_{\{x,\rho\}m}\} < 0$ for a finite number of Floquet modes m. This is necessary because some leaky-wave modes have propagation constants β that lie on a lower Riemann sheet with respect to one or more branch cuts.

The sum (3.3) converges exponentially fast when $|x|,\rho$ are large compared to the wavelength λ, with the number of terms required to achieve a high accuracy being greater than $L/(2\pi|\{x,\rho\}|)$. On the other hand, as $|\rho|,|x|\to 0$, the summations in (3.3) converge extremely slowly. However, it is this latter case, where the fields are observed along the axis of the sources, that is often of interest. Alternative spectral expansions must be considered.

B. Transverse Spectral Expansion

This section considers a spectral expansion of the Green's function transverse to the array axis. In this direction the only boundary condition is the radiation condition, requiring the phase to propagate outward. This spectrum is therefore continuous, and the expansion takes the form of a spectral integral. The argument of the integral is a product of one function of x,ρ that is known to satisfy the radiation condition, and an unknown function of z:

$$G^{2D}(\mathbf{r})=\frac{1}{2\pi}\int_{-\infty}^{\infty}g_z(z)e^{ik_x x}dk_x,\quad G^{3D}(\mathbf{r})=\frac{1}{4\pi}\int_{-\infty}^{\infty}g_z(z)H_0^{(1)}(k_\rho\rho)dk_\rho \tag{3.4}$$

Plugging these expressions into Eq. (2.4) results a 1D equation for $g_z(z;k_z)$.

$$\frac{d^2}{dz^2}g_z+k_z^2 g_z=-\delta(z) \tag{3.5}$$

The solution is the 1D periodic Green's function for the Helmholtz equation. It may be found as a geometric spatial series of exponential functions, taken over all unit cells.

$$g_z(z;k_z)=\sum_{n=-\infty}^{\infty}\frac{e^{ik_{z0}nL}e^{ik_z|z-nL|}}{-2ik_z}=\frac{1}{-2ik_z}\left(\frac{e^{ik_z|z|}}{1-e^{i(k_z-k_{z0}sign(z))L}}-\frac{e^{-ik_z|z|}}{1-e^{-i(k_z+k_{z0}sign(z))L}}\right) \tag{3.6}$$

The two terms of $g_x(x,k_x,k_{x0})$ in the brackets of Eq. (3.6) represent the contributions of the sources on each side of the origin. By eliminating one of these terms, the Green's function for a semi-infinite periodic system may easily be formulated. Finally, the symmetry of the spectral integrals with respect to k_x, k_ρ allow them to be reformulated as semi-infinite integrals.

$$\begin{aligned} G^{2D}(\mathbf{r}) &= \frac{1}{\pi}\int_0^\infty dk_x \cos(k_x x) g_z(z,k_z(k_x)), \\ G^{3D}(\mathbf{r}) &= \frac{1}{2\pi}\int_0^\infty dk_\rho k_\rho J_0(k_\rho \rho) g_z(z,k_z(k_\rho)). \end{aligned} \tag{3.7}$$

Here, $J_0(k_\rho\rho)$ is the zeroth-order Bessel function, and $k_x = (k^2 - k_{z,\rho}^2)^{1/2}$ is the longitudinal wavenumber.

The result of the transverse representation in (3.7) is identical to that in (3.3) if all square roots in (3.3) are defined on the upper Riemann sheet, i.e. if $\mathrm{Im}\{k_{\{x,\rho\}m}\} \geq 0$. To define the PGFs on the lower Riemann sheet associated with a wavenumber $k_{\{x,\rho\}M}$, the expression in (3.7) is modified as

$$\begin{aligned} G^{2D}(\mathbf{r}) &\to G^{2D}(\mathbf{r}) - \frac{2}{L}\frac{\cos(k_{xM}x)e^{ik_{zM}z}}{-2ik_{xM}}, \\ G^{3D}(\mathbf{r}) &\to G^{3D}(\mathbf{r}) - \frac{2}{L}\frac{1}{4i}J_0(k_{\rho M}\rho)\,e^{ik_{zM}z}. \end{aligned} \tag{3.8}$$

Here, $G^{2D,3D}(\mathbf{r})$ in the left and right-hand sides are PGFs defined on the lower and upper Riemann sheet of $k_{\{x,\rho\}M}$, respectively. This expression can be obtained by taking the difference between $G^{2D,3D}(\mathbf{r})$ on the lower and upper Riemann sheets. It is noted that in

practical situations, only a small number of lower Riemann sheets (typically 1) is required to be considered. The rest of the analysis in this chapter assumes that the PGFs are defined on the upper Riemann sheets of $k_{\{x,\rho\}m}$ for all m.

The integrands in the representation (3.7) show exponential decay in the $n = 0$ unit cell, owing the behavior of $g_z(z;k_z)$, even for the case $|\, x \,| = \rho = 0$, provided that $z \neq 0$. For this reason the longitudinal representation is the better choice for finding the fields at or near the axis of the sources. Numerical integration, however, is complicated by a number of factors. As $z \to 0$, the exponential decay of the integrand is weak, and the integral converges slowly. Also, the 1D PGF $g_z(z;k_z)$ has an infinite number of poles in the complex $k_{z,\rho}$ plane at $k_{\{x,\rho\}m} = \left(k_0^2 - (k_{z0} + 2\pi m/L)^2\right)^{1/2}$, which correspond to the Floquet mode wavenumbers $k_{zm} = k_{z0} + 2\pi m/L$. For lossless configurations and purely real k_{z0}, most of these poles are on the imaginary axis in the k_x, k_ρ plane. However, some may lie directly on the real axis, which is the integration contour, and introduce significant variations to the integrand. The rest of this chapter is therefore devoted to the regularization of the integrand and fast computation of the resulting integral.

3.3 Regularized Transverse Representation

The convergence of the integrals (3.7) can be improved by explicitly extracting the contribution of a certain number of sources in and around the unit cell of interest and evaluating them directly using the spatial PGFs in Eq. (2.6). The remaining infinite

sources may be evaluated using the transverse representation (3.7). To formulate this, the longitudinal spectral PGF $g_z(z,k_z)$ in (3.6) can be rewritten as

$$g_z(z,k_z)=\left(\sum_{n=-N_d}^{N_d}\frac{e^{ik_{z0}nL}e^{ik_z|z-nL|}}{-2ik_z}\right)+\frac{e^{ik_zL(N_d+1)}}{-2ik_z}\left(\frac{e^{-ik_{z0}L(N_d+1)}e^{ik_zz}}{1-e^{i(k_z-k_{z0})L}}+\frac{e^{ik_{z0}L(N_d+1)}e^{-ik_zz}}{1-e^{i(k_z+k_{z0})L}}\right) \quad (3.9)$$

Here, the first term in the right-hand side is a summation of free-space longitudinal spectral 1D PGF, taken over $2N_d+1$ sources residing at locations $z_n=nL$ around the origin. The second term in the right-hand of (3.9), which comprises the contribution from the remaining infinite number of sources, decays exponentially fast for large $k_{x,\rho}$. The resulting improvement of the integral's convergence indicates that within the unit cell of interest, most of the field variations result from a small number of nearby sources whose contribution may be readily evaluated in closed form. The fields resulting from the remaining infinite sources are slowly varying, and so the integral that accounts for them is relatively easy to evaluate numerically. It is stressed that with this modification the convergence is good for any observation coordinate z within the $n=0$ (zeroth) unit cell, including $z=0$. This latter case is important when evaluating the fields at the origin, with the $n=0$ source term excluded, as is necessary when finding the interaction of a single current source with the rest of the array, as in Eq. (2.11).

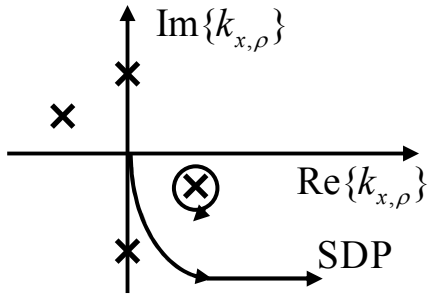

Fig. 3-2 The complex $k_{x,\rho}$ plane with poles and SDP

Next, to avoid the oscillatory behavior of the integrands in (3.7) , the integration path can be deformed from the original path along the real axis to the to the steepest descent path (SDP) [10, 30] (see Fig. 3-2) in the k_ρ and k_x planes. In general, the SDP path should pass through a saddle point whose position in the complex $k_{x,\rho}$ plane depends on $N_d L$, and the observation coordinates. Here, to obtain a robust scheme for any $\mathbf{r}$ close to the array, it is assumed that $N_d L > |\mathbf{r}|$, so that the $e^{ik_z L(N_d+1)}$ is the fastest varying term in the integrand. The saddle point is then given by $k_{x,\rho} = 0$. If poles are crossed while deforming the original integration path to the SDP, their corresponding residue contributions must be taken into account. To this end, the scalar PGFs can be written as

$$\begin{aligned} G^{2D}(\mathbf{r}) &= \sum_{n=-N_d}^{N_d} e^{ik_{z0}nL}\frac{i}{4}H_0^{(1)}(k_0 R_n) + \frac{2}{L}\sum_{m=1}^{N_p}\frac{\cos(k_{xm}x)e^{ik_{zm}z}}{-2ik_{xm}} + G_{SDP}^{2D}(\mathbf{r}), \\ G^{3D}(\mathbf{r}) &= \sum_{n=-N_d}^{N_d} e^{ik_{z0}nL}\frac{e^{ik_0 R_n}}{4\pi R_n} + \frac{2}{L}\sum_{m=1}^{N_p}\frac{1}{4i}J_0(k_{\rho m}\rho)e^{ik_{zm}z} + G_{SDP}^{3D}(\mathbf{r}). \end{aligned} \tag{3.10}$$

where $R_n = |\mathbf{r} - nL\hat{\mathbf{z}}|$. Here, the first sums represent contributions due to $N_d + 1$ sources located in and around the origin. The second sums represent the residue contributions of N_p poles crossed while the deforming the original integration path to the SDP. Comparing with the Floquet mode representation, these pole contributions are identified as combinations of the Floquet modes with symmetric behavior with respect to the direction transverse to the array axis (x and ρ directions).

The functions $G_{SDP}^{2D}(\mathbf{r})$ and $G_{SDP}^{3D}(\mathbf{r})$ in (3.10) are SDP integrals given by

$$\begin{aligned} G_{SDP}^{2D}(\mathbf{r}) &= \frac{1}{\pi}\int_{\mathrm{SDP}}\left(\frac{e^{-ik_{z0}L(N_d+1)}e^{ik_z z}}{1-e^{i(k_z-k_{z0})L}} + \frac{e^{ik_{z0}L(N_d+1)}e^{-ik_z z}}{1-e^{i(k_z+k_{z0})L}}\right)\frac{e^{ik_z L(N_d+1)}\cos(k_x x)}{-2ik_z}dk_x, \\ G_{SDP}^{3D}(\mathbf{r}) &= \frac{1}{2\pi}\int_{\mathrm{SDP}}\left(\frac{e^{-ik_{z0}L(N_d+1)}e^{ik_z z}}{1-e^{i(k_z-k_{z0})L}} + \frac{e^{ik_{z0}L(N_d+1)}e^{-ik_z z}}{1-e^{i(k_z+k_{z0})L}}\right)\frac{e^{ik_z L(N_d+1)}J_0(k_\rho \rho)}{-2ik_z}k_\rho dk_\rho. \end{aligned} \tag{3.11}$$

The deformation of the contour to the SDP may be expressed mathematically by a change of variables. Let the dimensionless variable s be defined through $k_z = k_0(1+is^2)$, with $k_{x,\rho} = k_0 s\sqrt{s^2-2i}$. The SDP is then the real axis in the complex s plane, with saddle point at $s = 0$. The integrals (3.11) are then expressed as

$$\begin{aligned} G_{SDP}^{2D}(\mathbf{r}) &= \int_0^\infty f^{2D}(s)e^{-\alpha s^2}\frac{ds}{\sqrt{s^2-2i}}, \\ G_{SDP}^{3D}(\mathbf{r}) &= \int_0^\infty f^{3D}(s)e^{-\alpha s^2}sds, \end{aligned} \tag{3.12}$$

where $\alpha = kL(N_d+1)$ and

$$
\begin{aligned}
f^{2D}(s) &= \frac{1}{\pi}\left(\frac{e^{-ik_{z0}L(N_d+1)}e^{-k_0 z(s^2-i)}}{1-e^{-ik_{z0}L}e^{-k_0 L(s^2-i)}}+\frac{e^{ik_{z0}L(N_d+1)}e^{k_0 z(s^2-i)}}{1-e^{ik_{z0}L}e^{-k_0 L(s^2-i)}}\right)\cos(k_0 x\, s\sqrt{s^2-2i}),\\
f^{3D}(s) &= \frac{1}{2\pi}\left(\frac{e^{-ik_{z0}L(N_d+1)}e^{-k_0 z(s^2-i)}}{1-e^{-ik_{z0}L}e^{-k_0 L(s^2-i)}}+\frac{e^{ik_{z0}L(N_d+1)}e^{k_0 z(s^2-i)}}{1-e^{ik_{z0}L}e^{-k_0 L(s^2-i)}}\right)J_0\left(k_0\rho\, s\sqrt{s^2-2i}\right).
\end{aligned}
\tag{3.13}
$$

The factor of $e^{-\alpha s^2}$ in each integral ensures a rapid decay of the integrand, and this decay is more significant for large N_d. Typically, a small N_d is adequate to render sufficient convergence, and for most practical problems only a small number of poles N_p need to be taken into account. An important difference between the integrands in (3.13) is that the integrand of G_{SDP}^{2D} has a branch cut $\sqrt{s^2-2i}$, which appears due to the variable transformation from $k_{x,\rho}$ to s, whereas the integrand of G_{SDP}^{3D} does not. As explained in Sec. 5.2, the presence of the branch cut may lead to a low-frequency breakdown for the 2D case and requires modifications in handing the low-frequency regime ($L \ll \lambda$). The absence of the branch cut in the integrand of G_{SDP}^{3D} is due to presence of the k_ρ factor in the integrand for this case.

In some cases, however, a pair of poles in the s plane, found at $s_m = \pm\sqrt{i(1-k_{zm}/k_0)}$, may reside near the saddle point at the origin. The variations introduced from these singularities can significantly slow the integral's convergence, despite the Gaussian decay factor. Such situations are encountered when the poles are within the contributing zone of the integrand, i.e. when $|s_m| < \Omega_p \Big/ \alpha^{1/2}$ with Ω_p being a parameter of order $O(1)$. This occurs when the phase shift factor k_{z0} is close to the free-

space wavenumber k_0. This situation is called the "blind angle" regime, as it occurs when a plane wave is incident on the structure with an angle θ that is very close to $\pi/2$. This case is important, as traveling wave modes on various types of resonant arrays have propagation wavenumbers close to k_0.

To smooth these variations, one notes that near a simple pole s_m, the functions $f^{2D,3D}(s)$ are well approximated by $\underset{s=s_m}{res}\{f^{2D,3D}(s)\}/(s-s_m)$. This latter term may be explicitly extracted from the integrands in (3.12) and integrated in a closed form. Recall that the symmetry of $g_x(x,k_x)$ with respect to $k_{z,\rho}$ and s leads to the existence of pairs of poles $\pm s_m$ that are symmetric about the origin in the complex s plane. Assuming that there are a total (typically small) number of $\tilde{N}_p$ pole pairs that reside near the saddle point $s=0$. One can then rewrite the SDP integrals as

$$\begin{aligned} G_{SDP}^{2D}(\mathbf{r}) &= \int_0^\infty \tilde{f}^{2D}(s)e^{-\alpha s^2}\frac{ds}{\sqrt{s^2-2i}} + \sum_{n=1}^{\tilde{N}_p} 2s_m \operatorname*{res}_{s=s_m}\{f^{2D}(s)\}I_m^{2D}\ , \\ G_{SDP}^{3D}(\mathbf{r}) &= \int_0^\infty \tilde{f}^{3D}(s)e^{-\alpha s^2}sds + \sum_{n=1}^{\tilde{N}_p} 2s_m \operatorname*{res}_{s=s_m}\{f^{3D}(s)\}I_m^{3D}\ . \end{aligned} \tag{3.14}$$

where

$$\tilde{f}^{2D,3D}(s) = f^{2D,3D}(s) - \sum_{m=1}^{\tilde{N}_p}\frac{2s_m \operatorname*{res}_{s=s_m}\{f^{2D}(s)\}}{s^2-s_m^2} \tag{3.15}$$

are non-resonant functions that have no singularities near the integration path. The integrals I_m^{2D} and I_m^{3D} in (3.14) are given by

$$
\begin{aligned}
I_m^{2D} &= \int_0^{\infty} \frac{e^{-\alpha s^2}}{s^2 - s_m^2} \frac{ds}{\sqrt{s^2 - 2i}} = \frac{\pi e^{-\alpha s_m^2} \operatorname{erfc}(-is_m\sqrt{\alpha}\,\operatorname{sign}(-is_m))}{2s_m\sqrt{s_m^2 - 2i}\,\operatorname{sign}(-is_m)} \\
&\quad + \int_0^{\infty} \frac{e^{-\alpha s^2}}{s^2 - s_m^2} \left(\frac{1}{\sqrt{s^2 - 2i}} - \frac{1}{\sqrt{s_m^2 - 2i}} \right) ds, \qquad (3.16) \\
I_m^{3D} &= \int_0^{\infty} \frac{e^{-\alpha s^2}}{s^2 - s_m^2} s ds = \frac{1}{2} e^{-\alpha s_m^2} \operatorname{Ei}(-\alpha s_m^2),
\end{aligned}
$$

where erfc is the complementary error function, and Ei is the exponential integral function [31]. The integrals for I_m^{2D} can be rapidly evaluated numerically using various adaptive integration methods. The integrand of the first integral for I_m^{2D} has a pole and a branch-cut singularity, whereas the second has only the branch-cut singularity, which allows for a simpler numerical evaluation. It is important to mention that the integrals and special functions in (3.16) do not depend on the observation location and need to be evaluated only once for a given problem. Therefore, they do not contribute significantly to the overall computational cost when implemented in a Method of Moments solver.

3.4 Numerical Implementation

The first integration terms in the right-hand side of (3.14) can be evaluated using various quadrature rules, e.g. those developed in Appendix A and B. The resulting SDP integrals are given by

$$
G_{SDP}^{2D,3D}(\mathbf{r}) = \sum_{q=1}^{N_q} \tilde{f}^{2D,3D}(s_q^{2D,3D}) e^{-\alpha\left(s_q^{2D,3D}\right)^2} w_q^{2D,3D} + \sum_{n=1}^{\tilde{N}_p} 2s_m \operatorname*{res}_{s=s_m} \{f^{2D,3D}(s)\} I_m^{2D,3D} \qquad (3.17)
$$

where $s_q^{2D,3D}$ are quadrature nodes for 2D and 3D problems given in the appendix, $w_q^{2D,3D}$ are corresponding quadrature weights, and N_q is the number of quadrature nodes (and weights). For the 2D case, the quadrature rules are defined differently for high-frequency ($\alpha \gg 1$, i.e. $L \sim \lambda$ or $L \gg \lambda$) and low-frequency ($\alpha \ll 1$, i.e. $\lambda \ll L$) regimes. For the high frequency regime ($\alpha \gg 1$), a simple equally-spaced node quadrature rule is very efficient (Appendix A). For the low-frequency regime, the square root $\sqrt{s^2 - 2i}$ varies much faster than the exponential term $\exp(-\alpha s^2)$, and requires a special treatment. As shown in Appendix B, the square-root term can be expanded over a series of cosine functions and this series can be truncated to result in a quadrature rule with a small number of quadrature nodes for any α. For the 3D case, an efficient quadrature rule is obtained in Appendix C based on the integrand expansion over Bessel function series. This rule applies to any periodicity (electrically small and large) without modification because the 3D integrand in (3.14) does not have a branch-cut singularity.

With this regularization of the integrals, the transverse spectral representations are highly efficient for computing the 2D and 3D PGFs for any observation location near the structure (whether for $x = \rho = 0$, or for $\mathbf{r} = 0$, or for x, ρ of several λ) and for any practical periodicities L (whether electrically small with $L \ll \lambda$, intermediate with $L \sim \lambda$, and electrically large $L \gg \lambda$). The combined number of quadrature nodes N_q, pole contributions N_p, extracted pole terms $\tilde{N}_p$, and direct components N_d is typically small to achieve any accuracy up to double precision.

Having established a procedure for calculating the scalar PGFs $G^{2D,3D}$, one may apply the dyadic operator in Eq. (2.5) to find the full dyadic PGFs $\mathbf{G}^{2D,3D}$. The dyadic operator, involving derivatives with respect to spatial coordinates, is brought inside the integrals in Eq. (3.7).

$$\begin{aligned}\mathbf{G}^{2D}(\mathbf{r}) &= \frac{i\eta}{\pi k_0}\int_0^\infty dk_x (k_0^2\mathbf{I}+\nabla\nabla)\cos(k_x x) g_z(z,k_z(k_x)),\\ \mathbf{G}^{3D}(\mathbf{r}) &= \frac{i\eta}{2\pi k_0}\int_0^\infty k_\rho dk_\rho (k_0^2\mathbf{I}+\nabla\nabla) J_0(k_\rho\rho) g_z(x,k_z(k_\rho)).\end{aligned} \tag{3.18}$$

The same process of regularization that is applied to the integrals for scalar Green's function case may be applied to each dyadic component, and the same quadrature rules for integration may be applied with no special modification. The implementation of the dyadic PGFs allows one to find all the electric-field components resulting from an infinite array of identical dipole sources oriented in any direction. To find the magnetic-field components a similar approach may be used, involving a different dyadic operator but this discussion is omitted for brevity.

3.5 Numerical Results

This section presents numerical analysis that shows how the formulations in Secs. 5 and 6 can be used to calculate scalar and dyadic 2D and 3D PGFs. It also studies the convergence rates of the obtained representations and shows that these representations are very efficient for a wide range of structure parameters. The numerical analysis starts with calculating 2D and 3D fields near a 1D array for different structure parameters and proceeds with the study of the error behavior.

Figure 3-3(a) shows the magnitudes of the scalar 3D PGF G^{3D} and the dyadic components, G_{zz}^{3D} and G_{yy}^{3D}, plotted very close to the z axis along the horizontal line $0 < z < 0.5L$ (half of the unit cell is sufficient due to symmetry). The calculations are done using Eq. (3.10) with $L = 2\lambda$, $y = 0$, $| x |= 10^{-3} L$, and $k_{z0} = (0.85 + .001i)k_0$. The contribution from the source at the zeroth unit cell (i.e. $G_0^{2D,3D}$, $\mathbf{G}_0^{2D,3D}$) is subtracted to avoid divergence at the unit cell center. Close to the z axis the off-diagonal components of $\mathbf{G}^{3D}$ vanish, while G_{yy}^{3D} and G_{xx}^{3D} are nearly equal. Physically, this indicates that as $\rho \to 0$ the electric fields from a periodic array of dipoles oriented transverse to the z axis are also transverse to the z axis. If the dipoles point along the array axis, so do the electric fields. Figure 3-3(b) shows $| G^{2D} |$ plotted along the same line, but for $x = 0$ and $x = 0.1L$. The corresponding dyadic components are not shown; for most 2D problems the fields may be separated into TE and TM components, each of which may be solved using the scalar PGF G^{2D}, so the dyadic operator $\mathbf{G}^{2D}$ is of limited interest.

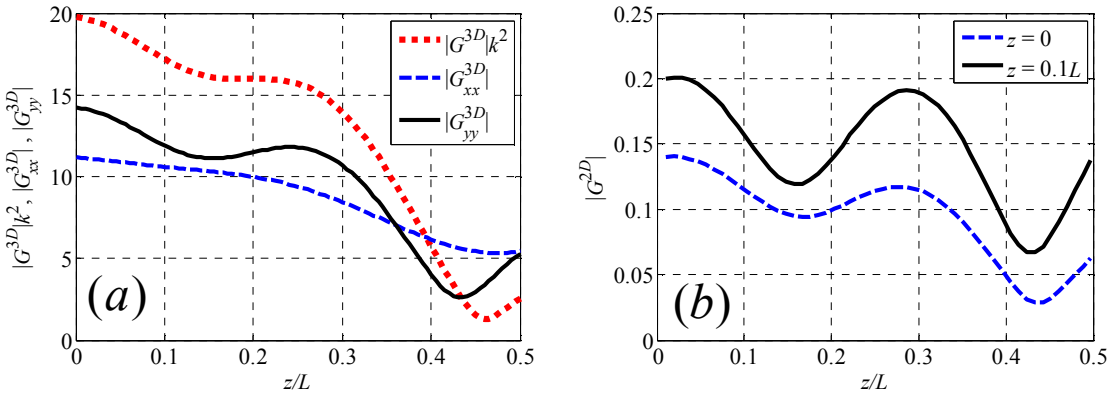

Fig. 3-3 (a) Magnitudes of the scalar PGF G^{3D} and the dyadic components G^{3D}_{zz} and G^{3D}_{yy} at $|x| = 10^{-3}L$, $y = 0$ and (b) the magnitude of the scalar PGF G^{2D} for two values of x.

To further demonstrate the rapid convergence of the transverse representation over a wide range of values of the period L, Figs. 3-4(a) and 3-4(b) show the relative error between the results of the longitudinal and transverse representations obtained via Eqs. (3.3) and (3.7) as a function of the number of quadrature nodes N_q used in the SDP integrations. The error of the transverse representation is defined as

$$\text{Error}^{2D,3D} = \left(\frac{\int_0^{L/2} | G^{2D,3D}_{\text{exact}}(\mathbf{r}) - G^{2D,3D}_{\text{numeric}}(\mathbf{r}) |^2 \, dz}{\int_0^{L/2} | G^{2D,3D}_{\text{exact}}(\mathbf{r}) - G^{2D,3D}_{0}(\mathbf{r}) |^2 \, dz} \right)^{1/2} \tag{3.19}$$

where $G^{2D,3D}_{\text{exact}}$ are obtained via (3.8) with a very large number of terms to achieve double-precision accuracy and $G^{2D,3D}_{\text{numeric}}$ are computed using the rapid transverse formulation with the SDP integrals evaluated with quadrature rules detailed in the Appendix. Note that in the denominator of (3.19) the zeroth direct term $G^{2D,3D}_{0}(\mathbf{r})$ is extracted from the reference

(numerically "exact") PGF $G_{\text{exact}}^{2D,3D}(\mathbf{r})$ to avoid division by a large number for $\mathbf{r} \to 0$. Without extracting this zeroth term, the resulting error would artificially become significantly lower for small $\mathbf{r}$. Calculations were done using $|x| = \rho = 10^{-3}L$, $k_{z0} = (0.85 + .001i)k_0$, $N_d = 5$ for three values of periodicity ranging from extremely small ($L = 10^{-6}\lambda$) to moderate ($L = 0.6\lambda$), and to very large ($L = 10\lambda$). Very small periods correspond to dense arrays, such as meshes. Moderate periods (on the order of a wavelength) are characteristic of filters as well as phased array, leaky-wave, and traveling/surface wave antennas. Large periods can also model certain antenna arrays. The truncation parameter Ω_s, defined in the Appendix, was chosen in the range from 2.4 to 6.2. It is evident that the results converge very rapidly with an increase of the number of integration nodes for any value of the period that would be of practical interest. The components of the dyadic PGFs show similar convergence behavior and, therefore, are not shown.

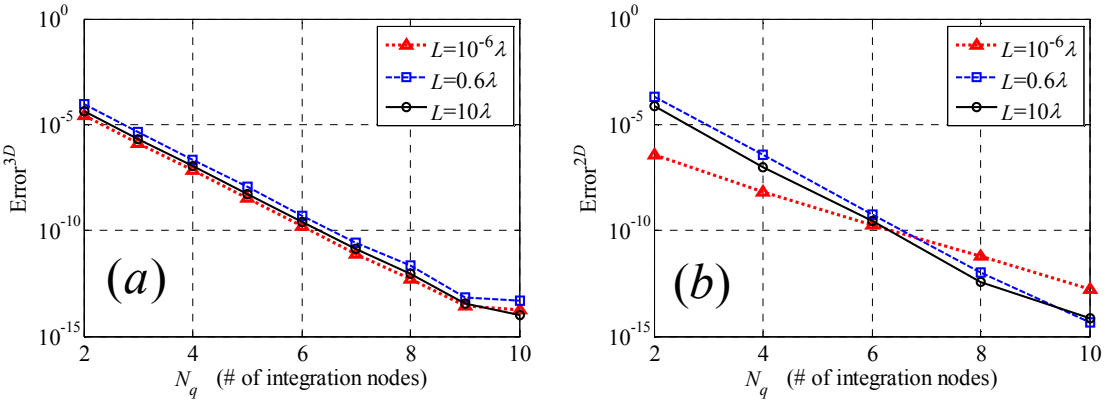

Fig. 3-4 Error of the PGFs (a) G^{3D} and (b) G^{2D} as a function of the number of integration nodes for three values of the spacing L.

Figures 3-4(a) and 3-4(b) study the convergence of the transverse representation for a range of observation distances x and ρ from the array for which the Floquet mode representations may still be impractical. The structure parameters are chosen as $L = 0.6\lambda$, $k_{z0} = (0.85 + .001i)k_0$, and Ω_s, fixed for each curve, ranges from 3.8 to 5.5. The error increases away from the array, which is associated with an increased rate of the integrands' variation for larger x and ρ. Clearly the largest errors are obtained for the smallest N_d and N_q ($N_d = 3$, $N_q = 6$). The error can be reduced by only a slight increase of N_d and/or N_q. It is also important to mention that very low errors with small N_d and N_q are obtained even for relatively larger displacement from the array ($\rho, x \sim 5\lambda$). This is an important property, as it can allow using the same formulation without switching it with other formulations (e.g. with the Floquet summation) for a wide range of structure parameters.

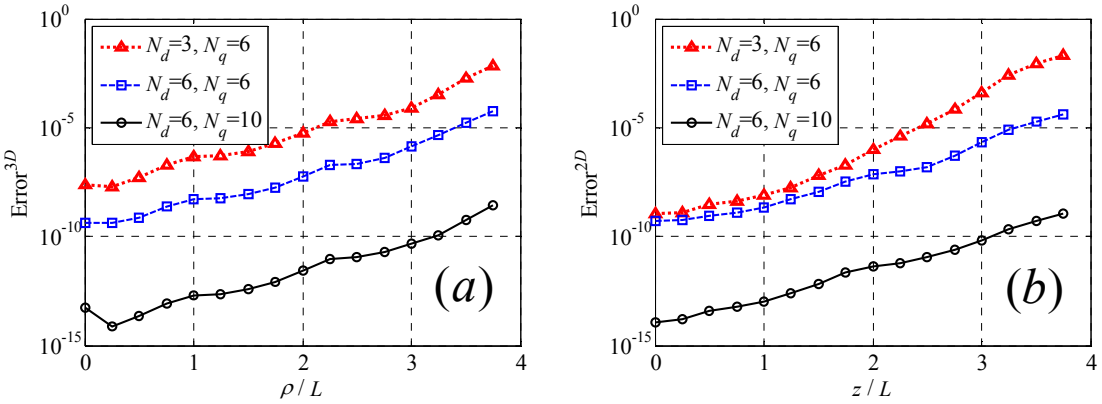

Fig. 3-5 Error of PGFs (a) G^{3D} and (b) G^{2D} as a function of distance from the array for different choices of convergence parameters.

3.6 Dispersion of Traveling Waves on Nanoparticle Arrays

This section uses the dyadic Green's function to compute the dispersion relations of traveling waves on linear arrays of nanoparticles. Such particles are known to support plasmonic resonances at wavelengths that may be large compared to the particle size. When arranged periodically, these particles can support traveling waves that are mediated by resonant interaction.

As an example, consider an infinite array of gold nanoshells of permittivity ε_m, assumed to follow the Drude model with parameters given by [32], with a silicon dioxide core of permittivity $\varepsilon_d = 2.37\varepsilon_0$, embedded in a silicon dioxide medium. The shell's inner and outer radii are r_1 and r_2 are $16nm$ and $23nm$, respectively, and the array spacing is $L = 80nm$. This structure supports independent longitudinal and transverse modes whose dispersion may be found by solving Eq. (2.11). Because the polarizability tensor $\boldsymbol{\alpha}$ is diagonal for these shells, the matrix equation separates out into one scalar equation for the longitudinal (z polarized) mode and two scalar equations for the two degenerate transverse modes. Their dispersion is shown in Fig. 3-6 for frequencies close to the shell static resonance at $495nm$. Also shown is the light-line, which marks the boundary between the slow (bound) and fast (radiating) modes. The transverse modes remain slow, while the longitudinal mode may radiate below the resonant frequency.

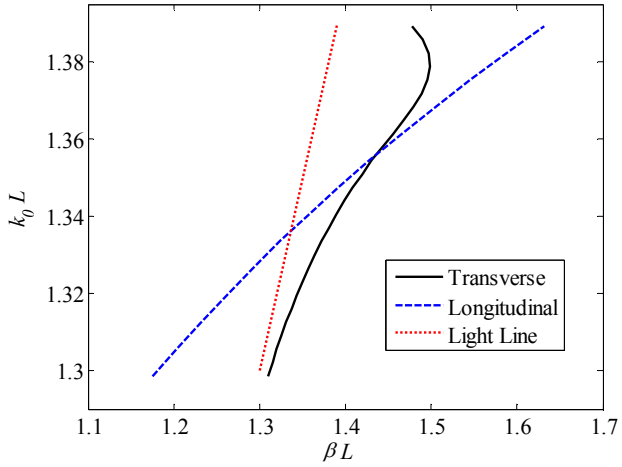

Fig. 3-6 Dispersion of the longitudinal and transverse wave modes supported by an infinite array of gold plasmonic nanoshells

3.7 Extensions to Green's Functions for Doubly Periodic Systems

The fast computation of the Green's function for a doubly periodic system, characterized by periodic boundary conditions along two dimensions, is also of strong interest. Consider a planar grid of sources oriented on the xy plane with spacing L_x and L_y in the x and y directions, and corresponding linear phase shift factors k_{x0} and k_{y0} (Fig 3-7). For simplicity, the unit cell of interest is centered at the origin. The Green's function G_{grid}^{3D} for this grid configuration may be solved using a Floquet series expansion:

$$G_{grid}^{3D} = \sum_{n,m=-\infty}^{\infty} \frac{e^{i(k_{xn}x+k_{ym}y+k_{znm}|z|)}}{-2ik_{znm}L_xL_y} \tag{3.20}$$

where $k_{xn} = k_{x0} + 2\pi n / L_x$, $k_{ym} = k_{y0} + 2\pi m / L_y$, $k_{znm} = \left(k_0^2 - k_{xn}^2 - k_{ym}^2\right)^{1/2}$. This representation, similar to (3.3), is efficient for observation points far from the array axis, but breaks down close to the xy plane.

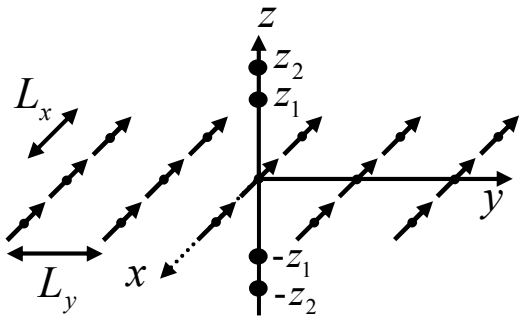

Fig. 3-7 A doubly periodic array of sources oriented on the xy plane.

The presented approach for finding the PGF for a linear periodic system is not readily extended to the case of a doubly periodic system. For 2D configurations, there is no transverse axis with radiation boundary conditions, so no efficient spectral integral may be formulated. For 3D systems, an integral formulation can be derived, but it is necessarily a doubly integral over two spectral parameters, only one of which can be transverse to the periodicity axes. For this case, the scalar periodic Green's function G_{grid}^{3D} for this grid array may be found by taking an infinite double summation of the single source Green's function G_0^{3D} over all elements. Using the integral identity (4.6), it takes the form

$$G_{grid}^{3D} = \frac{i}{8\pi^2}\sum_{n,m=-\infty}^{\infty} e^{ik_{x0}nL_x}e^{ik_{y0}mL_y}\int_{-\infty}^{\infty}\int_{-\infty}^{\infty} dk_z dk_y \frac{e^{ik_z z}e^{ik_y(y-mL_y)}e^{ik_x|x-nL_x|}}{k_x}$$
$$= -\frac{i}{2\pi^2}\int_{-\infty}^{\infty}\int_{-\infty}^{\infty} dk_z dk_y e^{ik_z z}k_y g_y(y,k_y)g_x(x,k_x) \tag{3.21}$$

where $k_x = \left(k_0^2 - k_z^2 - k_y^2\right)^{1/2}$. The integration can be accelerated using the method of steepest descent, but there are an infinite number of poles on the real k_y axis whose residue contributions would have to be added. Thus, one recovers the Floquet series in the y direction, requiring a large number of series terms for high accuracy when the observation point is near the xy plane. The advantages of such an approach over the Ewald method for planar periodic structures are not clear, and so it is not pursued.

However, another approach may be formulated, based on the observation that most of the field variations in the unit cell of interest result from a small number of neighboring unit cells, whose contribution is easily found in closed form. The fields resulting from the rest of the array are slowly varying. Although their field contributions near the xy plane are not easily evaluated using the Floquet series (3.20), they may easily be found at points $\pm z_1$ and $\pm z_2$, sufficiently far above and below the array. The fields at any point near the array can then be found by interpolating the fields from these four points. Because the cost of interpolation is small compared to the evaluation of series terms, this simple method can achieve high accuracy with a relatively small number of series term evaluations.

To illustrate this method, divide the Green's function G_{grid}^{3D} into near and far field components. The near field includes the $(2N_{dx}+1)(2N_{dy}+1)$ sources nearest the origin that are found within the rectangle defined by $|x| \le N_{dx}L_x$, $|y| \le N_{dy}L_y$, while the far field term accounts for the rest of the sources.

$$\begin{aligned} G_{near}(\mathbf{r}) &= \sum_{p=-N_{dx}}^{N_{dx}} \sum_{q=-N_{dy}}^{N_{dy}} e^{ik_{x0}pL_x + ik_{y0}qL_y} \frac{e^{ik_0 R_{pq}}}{4\pi R_{pq}} \\ G_{far}(\mathbf{r}) &= \sum_{n,m=-\infty}^{\infty} \frac{e^{i(k_{xn}x + k_{yn}y + k_{znm}|z|)}}{-2ik_{znm}L_xL_y} - G_{near} \end{aligned} \tag{3.22}$$

where $R_{pq}^2 = (x+pL_x)^2 + (y+qL_y)^2 + z^2$. Because $G_{far}(\mathbf{r})$ is a slowly varying function in the unit cell at the origin, it may be evaluated at the coordinates $(x, y, \pm z_1)$, $(x, y, \pm z_2)$ and interpolated to the observation coordinate (x, y, z). The scalar Green's function G_{grid}^{3D} and the components of the dyadic Green's function $\mathbf{G}_{grid}^{3D}$ are all either symmetric or antisymmetric with respect to z, so only two independent evaluations of $G_{far}(\mathbf{r})$ are necessary. The interpolation of $G_{far}(\mathbf{r})$ to the observation coordinate may be done using any available fast method, and $G_{near}(\mathbf{r})$ is readily evaluated directly from Eq. (3.22).

As an example, consider a planar array of sources with $L_x = \lambda / 5$, $L_y = 2.5L_x$, $k_{x0} = 1.01\,\mathrm{Re}\{k\}$, $k_{x0} = 0.5\,\mathrm{Re}\{k\}$, and observation point $x = y = 0.45L_x$, $z = 0$. (With the observation point directly in between the interpolation points, the interpolation is expected to be the *least* accurate.) The near field terms are chosen using the

parameters $N_{dx} = 6$, $N_{dy} = 4$, and the interpolation points satisfy $z_2 / z_1 = 1.1$. The Floquet series used to evaluate $G_{far}(x, y, z_1)$ and $G_{far}(x, y, z_2)$ is truncated at upper and lower limits $\pm n_{\max} = \pm M_x$, $\pm m_{\max} = \pm M_y$, which are chosen to satisfy the ratio $M_x / M_y = \mathrm{int}\left(\sqrt{L_y / L_x}\right)$, where *int* denotes the integer part. The interpolation points are chosen to be within a quarter wavelength of the xy plane. For higher accuracy solutions, they are moved closer to the xy plane and more Floquet series terms are computed. The accuracy of this method is assessed by comparing to a known reference solution. In this case, such a reference is found by adding a small amount of loss to the ambient space and directly summing very large number of spatial terms, found via Eq. (2.6). The loss is included as an imaginary part of the wavenumber k_0, such that $\mathrm{Im}\{k_0\} = -.01\,\mathrm{Re}\{k_0\}$. Figure 3-8 shows the relative error of this formulation compared to this reference as a function of the number of summation terms used in the evaluation of $G_{far}(x, y, z_1)$ and $G_{far}(x, y, z_2)$ combined, equal to $2(2N_{dx}+1)(2N_{dy}+1) + 2(2M_x+1)(2M_y+1)$. The interpolation is done using barycentric Lagrange interpolation, and its contribution to the total computation cost is negligible. The error is shown for the xx and zz components of the dyadic Green's function $\mathbf{G}^{3D}_{grid}$, and good convergence is easily achieved with around 10,000 summation terms.

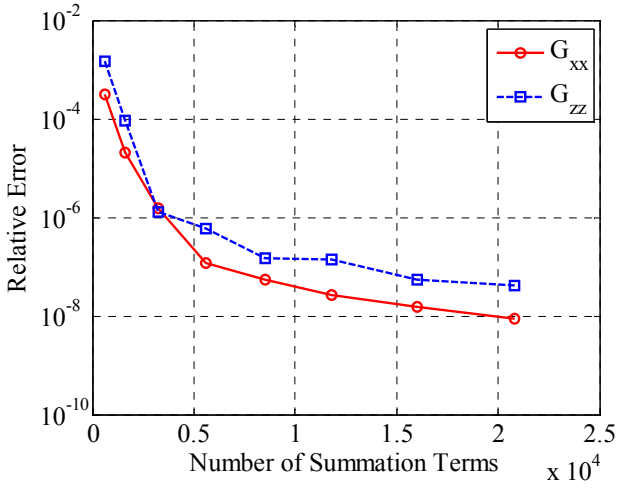

Fig. 3-8 Relative error versus number of summation terms used in the computation of the doubly periodic Green's function.

In the formulation presented, the Green's function was evaluated at a single observation point in the unit cell centered at the origin. Although simple to implement, this, approach does not typically outperform existing fast methods, such as the Ewald approach. However, practical integral equation solvers require computing the Green's function at many observation points in order to fill the impedance matrix **Z** in Eq. (1.2), and in these cases the interpolation method is much more efficient. For an arbitrary system with N unknown current elements in a unit cell, $N^2/2$ independent Green's function evaluations are typically required, contributing largely to the total computation time. The above interpolation method can be expanded to bypass this large computation cost. By choosing a grid of multiple interpolation points spanning the unit cell (rather than just four, as presented above), one can use interpolation to evaluate $\mathbf{G}_{grid}^{3D}$ anywhere in the unit cell. Thus, the series representing the near and far fields need be computed just

once for each interpolation point. The Green's function may then be found rapidly at any point in the unit cell as many times as needed by simply interpolating from these discrete points. This method is particularly advantageous for large-scale systems with very high N. In such cases the cost of evaluating the Green's function is negligible compared to the cost of solving the system of equations in Eq. (1.2), and so any available method can be used. For this reason simple Floquet summations are adequate, even for systems with periodicity along all three coordinate axes [33]. Another important feature is that this method is kernel independent; that is, it can be applied to periodic systems not only in free-space but also near surfaces or in waveguides. It could, in fact, be extended to analyze any type of N body problem with periodicity.

3.8 Conclusion

This chapter introduces rapid and accurate numerical implementations for scalar and dyadic PGFs for 2D and 3D configurations with 1D (linear) periodicities are introduced. The implementations are based on the expansion of the PGFs in terms of the continuous spectrum integrals over the transverse spectral parameters. To achieve a high convergence, the introduced integral representations are cast in a hybrid form in terms of (i) a small number of contributions due to sources located in and around the origin of a periodic unit cell of interest, (ii) a small number of the integrand pole residue contributions corresponding to symmetric combinations of Floquet modes generated by the array, and (iii) the remaining integrals evaluated along the SDP. The integrands of the SDP integrals are regularized by extracting the singular pole behavior near the saddle point of the integrand and integrating it in closed form. The resulting regularized

integrands exhibit a slowly varying dependence of the integration variable, which allows implementing highly efficient quadrature rules for the SDP integral evaluation. The integrals for the 2D case are further regularized by truncating the square-root behavior at low frequencies. Numerical simulations were executed to demonstrate strengths of the introduced approach. It was shown that the relative accuracy of 0.1% can be achieved with only about total number of 8 summation components. Double-precision accuracy can be achieved for a total number of about 25 summation components. Finally, extensions of this approach to systems with periodicity in two dimensions were discussed. An interpolation based approach was formulated that can be highly efficient when used in large-scale method of moments implementations, and can be extended to any large scale structure with periodicity.

3.9 Appendix: Quadrature Rules for Evaluating Integrals

For evaluating the SDP integrals in (3.14) one needs to construct a quadrature rule for integrals of the following form

$$\begin{aligned}\int_0^\infty \tilde{f}^{2D}(s)e^{-\alpha s^2}\frac{ds}{\sqrt{s^2-2i}} &= \sum_{q=1}^{N_q}\tilde{f}^{2D}(s_q^{2D})e^{-\alpha\left(s_q^{2D}\right)^2}w_q^{2D}\\ \int_0^\infty \tilde{f}^{3D}(s)e^{-\alpha s^2}sds &= \sum_{q=1}^{N_q}\tilde{f}^{3D}(s_q^{3D})e^{-\alpha\left(s_q^{3D}\right)^2}w_q^{3D}\end{aligned} \tag{3.23}$$

where s_q are the quadrature nodes, w_q are the corresponding quadrature weights, N_q is the number of the quadrature nodes, and $\tilde{f}^{2D,3D}(s)$ is an even function of s. Note that since the square-root $\sqrt{s^2-2i}$ is a complex valued function, the quadrature rule definition results in complex-valued weights.

Due to the exponential decay of the integrand, the upper integration limit of the integrals (3.23) can be truncated to a value $s_{\max}$, at which the integrand has a sufficiently low magnitude. This value can be chosen as $s_{\max} = \Omega_s \big/ \alpha^{1/2}$, where Ω_s is a parameter of $O(1)$ chosen as $\Omega_s = \sqrt{\log(1/\varepsilon)}$ with ε being a prescribed error of the integration truncation. For a given function, the accuracy of the developed quadrature rules depends on the parameter Ω_s. This parameter, through $s_{\max}$, determines the integral truncation error ε and the number of quadrature nodes N_q, which in turn determines how many expansion functions in a representation of $\tilde{f}^{2D,3D}(s)$ are integrated exactly. Large values of $s_{\max}$ require larger N_q to achieve a certain prescribed error, while small values of $s_{\max}$ result in a large integral truncation error. For a given N_q there is an optimal Ω_s (i.e. optimal $s_{\max}$) that leads to the minimal achievable error. Likewise, for a given Ω_s there is a minimal N_q that will lead to a minimal error. In practice one may choose N_q and Ω_s to be slightly greater than necessary to ensure sufficient convergence for any set of structure parameters.

A. 2D Case: High Frequency Regime ($\alpha \gg 1$, i.e. $L \sim \lambda$ or $L \gg \lambda$)

For $\alpha \gg 1$, the square root in (3.23) varies more slowly than the rest of the integrand. It is therefore assumed to be a slowly varying function that can be expanded

over a small number P of expansion functions in the truncated interval $s \in [0, s_{\max}]$. Taking into account the symmetry of the integrand, it can be expanded as

$$\frac{\tilde{f}^{2D}(s)e^{-\alpha s^2}}{\sqrt{s^2 - 2i}} = \sum_{p=0}^{P-1} a_p \cos\left(\frac{p\pi s}{2s_{\max}}\right) \tag{3.24}$$

Based on this expansion, a quadrature rule with equally spaced nodes

$$\begin{aligned} s_q^{2D} &= \frac{2s_{\max}(q + 1/2)}{(N_q - 1)};\ q = 1,\ldots,N_q, \\ w_q^{2D} &= \frac{(N_q - 1)}{2s_{\max}(q + 1/2)} \frac{1}{\sqrt{\left(s_q^{2D}\right)^2 - 2i}} \end{aligned} \tag{3.25}$$

integrates $P = 2N_q$ expansion (cosine) functions exactly. This simple quadrature rule, which leads to very high accuracy and convergence, is used in Eq. (3.14) to evaluate the SDP integral for the 2D case for the high-frequency regime.

B. Low Frequency Regime ($\alpha \ll 1$, i.e. $L \ll \lambda$)

In the low-frequency regime the square-root term $\sqrt{s^2 - 2i}$ in (3.23) varies much faster than the exponential term $\exp(-\alpha s^2)$ for s near the origin. To expand this square-root function in the truncated integration range ($s \in [0, s_{\max}]$), a large number of cosine functions is required

$$\frac{1}{\sqrt{s^2 - 2i}} = \sum_{p=0}^{\infty} b_p \cos\left(\frac{p\pi s}{2s_{\max}}\right) \tag{3.26}$$

Therefore, quadrature rules that assume slowly varying integrands, as in the high-frequency case, would lead to a low-frequency breakdown where no accurate solution

can be obtained. However, it is noted that the function $\tilde{f}^{2D}(s)e^{-\alpha s^2}$ still varies slowly and can be expanded over a small number P of cosine functions

$$\tilde{f}^{2D}(s)e^{-\alpha s^2} = \sum_{p=0}^{P-1} a_p \cos\left(\frac{p\pi s}{2s_{\max}}\right) \tag{3.27}$$

Therefore, the result of the integration in (3.23) will not change if the expansion of $\sqrt{s^2 - 2i}$ is truncated to the same number of P terms

$$\overline{h}(s) = \sum_{p=0}^{P-1} b_p \cos\left(\frac{p\pi s}{2s_{\max}}\right) \tag{3.28}$$

where $\overline{h}(s)$ is the truncated representation of $\sqrt{s^2 - 2i}$. The integrand with the truncated function $\overline{h}(s)$ can be expanded over $2P$ cosine functions

$$f(s)\overline{h}(s)e^{-\alpha s^2} = \sum_{p=0}^{2P-1} c_p \cos\left(\frac{p\pi s}{2s_{\max}}\right) \tag{3.29}$$

For such an integrand the following quadrature rule can be used

$$\begin{aligned} s_q^{2D} &= \frac{2s_{\max}(q + 1/2)}{(N_q - 1)}; \quad q = 1,..., N_q \\ w_q^{2D} &= \frac{(N_q - 1)}{2s_{\max}(q + 1/2)} \overline{h}(s_q^{2D}) \end{aligned} \tag{3.30}$$

to integrate exactly P expansion (cosine) functions. This quadrature rule is used for the low-frequency case ($\alpha \ll 1, L \ll \lambda$). It should be noted that the quadrature rule is efficient not only for $\alpha \ll 1$ but also for $\alpha \gg 1$. However, for $\alpha \gg 1$ the simple quadrature in (3.25) leads to a smaller number of quadrature nodes and, therefore, is used to obtain the results in the paper in this case.

C. 3D Case

The integrand for the 3D case in (3.23) is assumed to be a slowly varying function that can be expanded over a small number P of expansion functions in the truncated interval $s \in [0, s_{\max}]$. Taking into account the weighting function s, the semi-infinite integration range, and the behavior of the integrand in Eq. (3.13), $\tilde{f}^{3D}(s)e^{-\alpha s^2}$ can be expanded over an orthogonal set of Bessel functions

$$\tilde{f}^{3D}(s)e^{-\alpha s^2} = \sum_{p=1}^{P} a_p J_0\left(\frac{\chi_p s}{s_{\max}}\right) \tag{3.31}$$

where χ_p is the p^{th} zero of the Bessel function J_0. The basis functions $J_0\left(\chi_p s \big/ s_{\max}\right)$ are orthogonal over the range $s \in [0, s_{\max}]$ with respect to the weighting function s [31]. Following the conventional approach for deriving a quadrature rule for functions with a known expansion, the nodes s_q^{3D} and weights w_q^{3D} are found by solving the following system of equations

$$\int_0^{s_{\max}} J_0\left(\frac{\chi_p s}{s_{\max}}\right) s\,ds = \sum_{q=1}^{N_q} J_0\left(\frac{\chi_p s_q^{3D}}{s_{\max}}\right) w_q^{3D} \tag{3.32}$$

where, the integral in the left hand side is given in closed form by $\int_0^{s_{\max}} J_0(\chi_p s \big/ s_{\max}) s\,ds = s_{\max}^2 J_1(\chi_p) \big/ \chi_p$. Equations (3.31) represent a system of non-linear equations that can be solved for N_q nodes s_q^{3D} and weights w_q^{3D} (total $2N_q$ unknowns) using various modifications of Newton's method. Such solutions result in a Gaussian quadrature rule that integrates exactly $P = 2N_q$ expansion (Bessel) functions

$J_0\left(\chi_p s/s_{\max}\right)$. The quadrature rule obtained is used to evaluate the SDP integrals for the 3D case in (3.14).

3.10 Acknowledgements

The text of Chapter 3, in part, is a reprint of the material as it appears in the following publication: Derek Van Orden and Vitaliy Lomakin, "Rapidly Convergent Representations for 2D and 3D Green's functions for a Linear Periodic Array of Dipole Sources," IEEE Transactions on Antennas and Propagation, Vol. 57, 1973-1984 (2009). The dissertation author was the primary researcher and the co-author listed in this publication directed and supervised the research which forms the basis for this chapter.

Chapter 4 Green's Functions for a Linear Periodic Array Near a Planarly Layered Surface Medium

4.1 Introduction

This chapter extends the work of the previous chapter to the case of linear periodic arrays near planarly layered surfaces. This class of structures has important applications in microwave engineering and optics, such as antennas, waveguiding structures, frequency selective surfaces, gratings, and metamaterials [34-37]. Such structures are often fabricated on circuit boards by printing metallic patches and strips on a thin dielectric substrate. Simulating this class of structures using the method of moments requires a Green's function that that accounts for both the structure periodicity and the interactions with the surface. Fast methods to compute such a periodic Green's function (PGF) are essential for efficient integral equation solvers for periodic structures [38],[1]. Efficient computation of the Green's function may allow fast analysis of both scattering behavior and the complex dispersion properties of periodic arrays near surfaces.

A complete layered media PGF for a linear array can be represented as the sum of a free-space PGF, $\mathbf{G}_F$, which solves for a linear periodic structure in free-space, and a reflected fields PGF, $\mathbf{G}_R$, which accounts for the surface interaction. Fast evaluation of $\mathbf{G}_F$ was considered in chapter 3, and the purpose of this chapter is to present a method to efficiently evaluate $\mathbf{G}_R$. The problem of fast solvers for the reflected fields PGF $\mathbf{G}_R$ has

not been well studied. It may be represented as a direct spatial summation of single source (non-periodic) layered media Green's functions, which may be found via Sommerfeld integrations [30]. This infinite sum, however, converges very slowly, and diverges when a complex phase shift is applied between adjacent unit cells. The reflected fields may also be represented as an infinite sum of Floquet modes, but this series converges very slowly for the important case of observation points close to the array and the surface. This case is particularly important for periodic systems printed on surfaces, for which all source and observation points used to find the unknown equivalent currents are near the surface. To date, fast methods to accelerate the computation of $\mathbf{G}_R$ include a series representation based on perfectly matched layers [39], and an array-scanning technique that finds $\mathbf{G}_R$ from the doubly periodic layered medium Green's function [40]. The former method cannot evaluate the Green's function directly on the array axis, or with a complex phase shift between unit cells. Furthermore, it has not demonstrated high accuracy. The latter is very computationally costly, involving an integral over the Green's function for a free-space planar array, and detailed results have not yet been presented.

This chapter presents a fast method for computing the reflected fields PGF $\mathbf{G}_R$ for observation points close to a 1D array of electric dipole sources placed near a surface. The PGF for 2D and 3D configurations are formulated in terms of single and double spectral integrals, respectively, that are regularized to make it rapidly convergent, and a discrete spectrum of guided wave modes supported by the planarly layered medium. This representation can seamlessly handle source and observation points directly on the

surface, periodicities defined with complex phase shifts, and is fully applicable surfaces composed of lossy and gain media.

The representation of the reflected fields PGF $\mathbf{G}_R^{3D}$, solving for an array of point sources near a surface, is considerably more involved than the 2D case, which consists of an array of line sources. One reason is that in the 3D case, the surface breaks the cylindrical symmetry found in the free-space array. The spectral expansion of $\mathbf{G}_R^{3D}$ must therefore involve a double spectral integral in Cartesian coordinates, as opposed the single spectral integral found in chapter 3. The 2D Green's function $\mathbf{G}_R^{2D}$, in contrast, remains separable into the longitudinal and transverse coordinates, and requires only a single spectral integral, which is very similar to that formulated in Eq. (3.7) from the previous chapter. The second reason is that in the 3D case, a full dyadic Green's function must be formulated to account for all distinct polarization directions. For the 2D case, the fields may be decomposed into TE and TM components, whose contribution to the total field may be found using the scalar Green's function alone. For these reasons, the bulk of this chapter is devoted to the evaluation of $\mathbf{G}_R^{3D}$, while only one section near the end discusses the formulation and results for $\mathbf{G}_R^{2D}$.

4.2 Structure Configuration

Consider a linear, infinitely periodic array of electric dipole sources with spacing L oriented along the x axis, on or near a planarly layered medium. These are point sources for 3D configurations, as shown in Fig. 4-1, and line sources for 2D configurations. In

choosing the coordinate axes for this chapter, we follow a convention that the surface be parallel to the xy plane. Note that the periodicity axis is thus taken as the x axis, as opposed to the z axis, as in chapter 3. The electric dipole sources have dipole moments $\mathbf{p}_n = \mathbf{p}_0 e^{ik_{x0}nd}$, where k_{x0} is a (generally complex) phase shift parameter and n is an integer counting the sources. The moment $\mathbf{p}_0$ is the dipole moment of the source in the zeroth unit cell of the array, placed at the origin. The top surface of the medium is parallel to the xy plane, a distance h below the array. The surface has known transverse electric (TE) and magnetic (TM) reflection coefficients R^{TE} and R^{TM}, respectively. The reflection coefficients may be expressed as functions of k_0 and the spectral parameter k_z, whose ratio uniquely defines the angle of incidence for a plane wave.

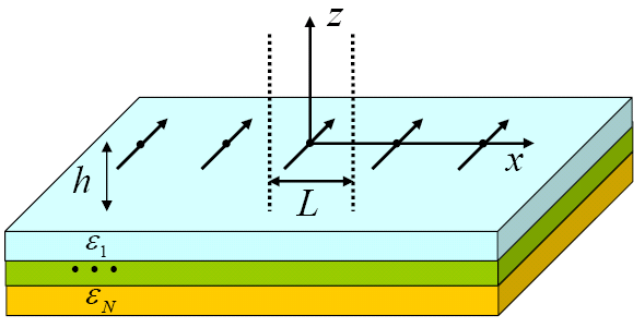

Fig. 4-1 A linear array of point dipole sources near a layered media background. The fields resulting from the array are found in the unit cell centered at the origin.

The electric fields resulting from this system for 2D and 3D of sources with current moment $\mathbf{p_0}$ may be expressed as

$$\mathbf{E}(\mathbf{r}) = \left(\mathbf{G}_F^{2D,3D}(\mathbf{r}) + \mathbf{G}_R^{2D,3D}(\mathbf{r} + h\hat{\mathbf{z}})\right) \cdot \mathbf{p_0} \tag{4.1}$$

where $\mathbf{G}_F$ and $\mathbf{G}_R$ are the dyadic Green's functions accounting for the free-space and reflected electric fields. The goal of this chapter is to present efficient representations of $\mathbf{G}_R^{2D}$ and $\mathbf{G}_R^{3D}$ for observation points close to the array and surface.

4.3 Spectral integral Representations of $\mathbf{G}_R^{3D}(\mathbf{r})$

A spectral representation of a free-space scalar Green's function G_F^{3D} may be used to find the layered medium PGF $\mathbf{G}_R^{3D}(\mathbf{r})$. The procedure is to expand G_F^{3D} into plane waves and find the dyadic PGF $\mathbf{G}_F^{3D}$ via a dyadic operator, given in Eq. (2.5). With $\mathbf{G}_F^{3D}$ expressed via a plane wave expansion, the components of $\mathbf{G}_R^{3D}$ may be found as the reflection of each plane wave from the layered medium. Section 4.3A briefly describes this procedure for the Floquet series representation of PGF, which is efficient for observation points far from the array axis and surface. Section 4.3B describes a new formulation that is efficient close to or on top of the surface.

A. Floquet Series Representation

Consider the Floquet series representation of the free-space PGF, which represents G_F^{3D} as an infinite sum of cylindrical waves:

$$G_F^{3D}(\mathbf{r}) = \frac{1}{L}\sum_{m=-\infty}^{\infty} e^{ik_{xm}x}\frac{i}{4}H_0^{(1)}\left(k_{\rho m}\sqrt{z^2+y^2}\right) \tag{4.2}$$

where $k_{xm} = k_{x0} + 2\pi m/L$ and $k_{\rho m} = (k_0^2 - k_{xm}^2)^{1/2}$ are the diffraction mode wavenumber components parallel to and transverse to the array axis, respectively. Each

cylindrical diffraction mode may be expanded into plane waves using an integral expansion of the Hankel function. The PGF then becomes

$$G_F^{3D}(\mathbf{r}) = \sum_{m=-\infty}^{\infty} e^{ik_{xm}x} \frac{i}{4\pi L} \int_{-\infty}^{\infty} dk_z \frac{e^{ik_z z} e^{ik_{ym}|y|}}{k_{ym}} \tag{4.3}$$

where $k_{ym} = (k_0^2 - k_{xm}^2 - k_z^2)^{1/2}$. This representation is well suited to finding the reflected fields Green's function. By applying the dyadic operator and inserting the TM reflection coefficient, the zz component of $\mathbf{G}_R^{3D}$ may be found as

$$G_{Rzz}^{3D} = \left(k_0^2 + \frac{\partial^2}{\partial z^2}\right) \sum_{m=-\infty}^{\infty} \frac{ie^{ik_{xm}x}}{4\pi\varepsilon L} \int_{-\infty}^{\infty} dk_z (-R^{TM}(k_z)) \frac{e^{ik_z z} e^{ik_{ym}|y|}}{k_{ym}} + DS_{zz}^{3D} \tag{4.4}$$

Here, DS represents the discrete spectrum of guided wave poles supported by the layered medium. It results from the fact that the complete expansion with respect to the k_z spectral parameter includes not only the continuous (plane wave) spectrum but also the discrete (guided mode) spectrum [30]. The evaluation of the discrete spectrum is discussed in Sec. 4-5.

This Floquet series is efficient for observation points far from the array and surface, e.g. for the far-field radiation from the array. However, it is very slowly convergent for observation points close to the array and surface.

B. Alternative Spectral Representation

The scalar PGF G_F^{3D} may also be represented as an infinite spatial sum of single-source Green's functions over all unit cells of the periodic system .

$$G_F^{3D}(\mathbf{r}) = \sum_{n=-\infty}^{\infty} e^{ik_{x0}nL} \frac{e^{ik_0\left|\mathbf{r}-n\hat{\mathbf{x}}L\right|}}{4\pi\left|\mathbf{r}-n\hat{\mathbf{x}}L\right|} \tag{4.5}$$

Using the Weyl identity, the Green's function for a single source may be expanded into plane waves as

$$\frac{e^{ikr}}{4\pi r} = \frac{i}{8\pi^2}\int_{-\infty}^{\infty}\int_{-\infty}^{\infty} dk_z dk_y \frac{e^{ik_z z}e^{ik_y y}e^{ik_x|x|}}{k_x} \tag{4.6}$$

with $k_x = (k_0^2 - k_z^2 - k_y^2)^{1/2}$. Using this expression in (4.5) yields an alternative representation of the scalar, free-space PGF.

$$G_F^{3D}(\mathbf{r}) = \frac{1}{4\pi^2}\int_{-\infty}^{\infty} dk_z e^{ik_z z}\int_{-\infty}^{\infty} dk_y e^{ik_y y} g_x(x,k_x,k_{x0}) \tag{4.7}$$

where $g_x(x,k_x,k_{x0})$ is the scalar PGF in 1D free-space.

$$g_x(x,k_x,k_{x0}) = \frac{i}{2k_x}\left(\frac{e^{ik_x|x|}}{1-e^{i(k_x-k_{x0}sign(x))L}} - \frac{e^{-ik_x|x|}}{1-e^{-i(k_x+k_{x0}sign(z))L}}\right) \tag{4.8}$$

The integral representation (4.7) may be extended to dyadics and used to find the fields reflected from a surface. For example, the zz component of $\mathbf{G}_R^{3D}$ may be found from $\mathbf{G}_R^{3D}$ by following the procedure outlined in [30]:

$$G_{Rzz}^{3D} = \left(k_0^2 + \frac{\partial^2}{\partial z^2}\right)\frac{1}{2\pi^2\varepsilon}\int_{-\infty}^{\infty} dk_z(-R^{TM}(k_z))e^{ik_z z}\int_0^{\infty} dk_y \cos(k_y y) g_x(x,k_x,k_{x0}) + DS_{zz}^{3D} \tag{4.9}$$

where symmetry has been used to reduce the integration over k_y to a semi-infinite integral. As in the Floquet series representation, DS^{3D} must be included to account for

the discrete spectrum of guided wave modes supported by the layered medium. Throughout the paper, equations and derivations are given for the zz dyadic component to demonstrate this alternative representation. However, this method is readily extended to all of the dyadic components. Their integral representations are given in Appendix A.

The integrands in (4.9) are highly oscillatory, making the integrals difficult to evaluate numerically. The strong variations result primarily from $g_x(x,k_x,k_{x0})$, which contains both rapidly varying exponential terms and poles that may reside close to the integration contour. The reflection coefficient also contains variations that complicate numerical integration. Section 4.4 is therefore devoted to the regularization and fast evaluation of these integrals, while section 4.5 discusses the evaluation of the discrete spectrum.

4.4 Rapid evaluation of Spectral Integral

The techniques for accelerating the double integral (4.9) are very similar to those used to accelerate the integrals (3.7) for the free-space linear PGF. First, a small number $2N_d+1$ sources near the unit cell may be explicitly extracted from the 1D PGF in Eq. (4.8), as in Eq. (3.9). The contribution from those sources may be computed separately using any fast method [10, 30, 41]. One may then deform the integration contours to the steepest descent path (SDP) and extract the resonant contributions of poles in the integrand. These latter techniques were also used for the free-space PGF in chapter 3, but in their implementation is more involved for the double integration considered here. The details are therefore presented in the next sections.

A. Steepest Descent Path Integration

The double spectral integrals used to evaluate the components of $\mathbf{G}_R$ may further be made rapidly convergent by deforming both integration contours to the steepest descent path (SDP) in the complex k_z and k_y planes, away from the real axes. This may be accomplished through the following change of variables:

$$\begin{aligned} k_z &= k_0 s_z \sqrt{s_z^2 - 2i}, \quad k_y = k_0 s_y \sqrt{s_y^2 + 2s_z^2 - 2i} \\ k_x &= \sqrt{k_0^2 - k_z^2 - k_y^2} = k_0(1 + i(s_z^2 + s_y^2)) \end{aligned} \tag{4.10}$$

The double integration is then taken along the real axes of the complex s_y and s_z planes, and the saddle point of this integration is located at $s_z = s_y = 0$. With this transformation, the term $e^{-jk_x L(N_d+1)}$ has exponential decay with respect to both integration variables, and the spectral integral I_{zz}^{SDP} for the zz component of $\mathbf{G}_R$ is expressed as

$$I_{zz}^{SDP} = \left(k_0^2 + \frac{\partial^2}{\partial z^2}\right)\frac{-k_0}{\pi^2 \varepsilon}\int_{-\infty}^{\infty} ds_z R^{TM}(k_z)\frac{s_z^2 - i}{\sqrt{s_z^2 - 2i}} e^{ik_z z}\int_0^{\infty} ds_y \frac{\cos(k_y y)}{\sqrt{s_y^2 + 2s_z^2 - 2i}}\tilde{g}_x(s_z, s_y),$$

$$\tilde{g}_x(s_z, s_y) = e^{ik_0 L(N_d+1)} e^{-k_0 L(N_d+1)(s_z^2+s_y^2)}\left(\frac{e^{-ik_{x0}L(N_d+1)} e^{ik_0(1+i(s_z^2+s_y^2))x}}{1 - e^{i\left(k_0(1+i(s_z^2+s_y^2)) - k_{x0}\right)L}} + \frac{e^{ik_{x0}L(N_d+1)} e^{-ik_0(1+i(s_z^2+s_y^2))x}}{1 - e^{i\left(k_0(1+i(s_z^2+s_y^2)) + k_{x0}\right)L}}\right) \tag{4.11}$$

The $\exp(-k_0 L(N_d + 1)(s_z^2 + s_y^2))$ term clearly shows that the integrand has Gaussian decay increasing with N_d. As the periodicity L decreases, this decay becomes weaker, requiring larger values of N_d for the same convergence.

In the process of deforming the integration contours, one or more poles of $\tilde{g}_x(s_z, s_y)$ may be crossed. It can be shown that this occurs only when k_{x0} has a nonzero imaginary part. In this case, the residues of the integrand at these poles must be accounted for. It is easily shown that these poles are found at $s_z^2 + s_y^2 = -i(k_{xm}^{\pm}/k_0 - 1)$, where $k_{xm}^{\pm} = \pm k_{x0} + 2\pi m/L$. (The $\pm$ sign distinguishes the poles resulting from the two terms of $\tilde{g}_x(s_z, s_y)$ in Eq.(4.11).) They exist in the combined space spanning two complex planes, and so the residue must be formulated as an integral in accordance with the residue theorem for higher dimension complex functions. It is shown in Appendix B that the residue of the m^{th} pole is

$$\underset{k_x = k_{xm}^{\pm}}{res}\{I_{zz}^{SDP}\} = \left(k_0^2 + \frac{\partial^2}{\partial z^2}\right)\frac{e^{\pm i k_{xm}^{\pm} x}}{4\pi i \varepsilon L}\int_{-\pi}^{\pi} R^{TM}\left(\sqrt{k_0^2 - k_{xm}^{\pm 2}}\,\sin\alpha\right)\exp\left(i\rho\sqrt{k_0^2 - k_{xm}^{\pm 2}}\,\cos(\alpha - \phi)\right) \tag{4.12}$$

where $\tan(\phi) = z/y$ and $\rho = (z^2 + y^2)^{1/2}$. It may be further shown that only the poles at k_{xm}^{+} can contribute if $\mathrm{Im}\{k_{x0}\} < 0$, while the poles at k_{xm}^{-} can contribute only if $\mathrm{Im}\{k_{x0}\} > 0$. For most cases of interest, only one or two poles contribute to the integral. However, for very large $k_0 L$ (e.g. greater than 15) the spectral spacing between the poles becomes small enough that more may have to be considered.

In general, the guided wave poles of the reflection coefficients are not crossed in the deformation to the SDP contours if the observation point is close to the array. If this

does occur (e.g. for observers removed from the array), however, the contribution of that pole to the discrete spectrum (see Sec. 4-5) must be excluded. The leaky wave poles of the reflection coefficients, in contrast, generally are crossed. These poles, which otherwise would not contribute to the discrete spectrum, must now be included, although in most cases their contributions are negligibly small.

The integral formulation of Eq. (4.11) assumes that the observation coordinates z and y are small compared to $L(N_d+1)$, in which case the saddle point of the SDP integrations lie near $s_z=0$ and $s_y=0$, as formulated in Eq. (4.10). As such, the presented integral representation is efficient for observation points relatively close to the array and surface (the separation should be smaller than $L(N_d+1)$). For larger values of z and y, the exponential and sinusoidal terms of the integrand become stronger and must be included in the SDP to regularize the integral. This leads to the saddle point moving off the origin, and, as a result, a larger number of residue contributions that must be included. Furthermore, in this case the integration over s_y cannot be reduced to a semi-infinite integral based on symmetry, as the reflection coefficient is not an even or odd function, so a fully infinite range must be included. These properties can be accounted for to result in a new spectral representation that is efficient also far from the array. However, for such large distances the Floquet mode representations of Sec. 4.3.A are already very efficient.

B. Extraction of Resonant Contributions of Poles

The poles of both the reflection coefficient and the 1D spectral PGF still contribute significant variations to the integrand in Eq. (4.11) if they are located near the saddle point of the SDP integration. These variations can significantly slow down numerical integration. This is especially true in the "blind angle" regime, where the phase shift parameter k_{x0} approaches the free-space wavenumber k_0 and the poles of $\tilde{g}_x(s_z, s_y)$ get very close to the saddle point. This case is particularly important to finding the complex dispersion relations of resonant arrays on surfaces, for which the propagation constant for traveling waves may be close to k_0. A further regularization of the integral is therefore required.

The resonant behavior resulting from the poles of $\tilde{g}_x(s_z, s_y)$ may be explicitly extracted from the integrand, making it slowly varying, and then integrated in closed form. To simplify the notation, the integrand of I_{zz}^{SDP} may be written as $R^{TM}(k_z(s_z))f_{zz}(s_z, s_y)\exp\left(-k_0 L(N_d+1)(s_z^2+s_y^2)\right)$. It is easily seen that the $f_{zz}(s_z, s_y)$ term is singular when $s_y = \pm s_{ym} = \pm(-i(k_{x0}/k_0 - 2\pi m/k_0 L - 1) - s_z^2)^{1/2}$. Near a pole singularity, $f_{zz}(s_z, s_y)$ may be well approximated by $res_{s_y=s_{ym}}\{f_{zz}(s_z, s_y)\}/(s_y - s_{ym})$, i.e. the residue of the function divided by its singular component. To extract the resonant contribution of $\pm s_{ym}$ for a given value of the integer m, one may subtract this term from the integral to regularize it and then separately integrate the subtracted terms in closed form:

$$I_{zz}^{SDP} = \int_{-\infty}^{\infty} ds_z R^{TM}(k_z(s_z)) \int_0^{\infty} ds_y \left(f_{zz}(s_z, s_y) - 2s_{ym} \frac{res_{s_y=s_{ym}} \{f_{zz}(s_z, s_y)\}}{s_y^2 - s_{ym}^2} \right) e^{-k_0 L(N_d+1)(s_z^2+s_y^2)} +$$

$$\int_{-\infty}^{\infty} ds_z R^{TM}(k_z(s_z)) \; res_{s_y=s_{ym}} \{f_{zz}(s_z, s_y)\} e^{-k_0 L(N_d+1)(s_z^2+s_{ym}^2)} \pi \frac{erfc\left(-i\sqrt{k_0 L(N_d+1)}\,\mathrm{sgn}(\mathrm{Re}\{-is_{ym}\})s_{ym}\right)}{-i\,\mathrm{sgn}(\mathrm{Re}\{-is_{ym}\})} \tag{4.13}$$

where $erfc$ denotes the complementary error function, and we have used the fact that $f_{zz}(s_z, s_y)$ is even in s_y to simplify the expression. The first term in Eq. (4.13) is the double integral that does not have variations resulting from the singularities at $\pm s_{ym}$. The second term is the integral of the resonant parts of $f_{zz}(s_z, s_y)$, and is represented as a 1D integral over s_z that displays a Gaussian convergence. For most cases, the contribution of only one pair of poles must be extracted, though this procedure is easily extended to cases where multiple poles of $\tilde{g}_x(s_z, s_y)$ are close to the saddle point.

It can also occur that the guided wave poles of R^{TM} are sufficiently close to the origin in the s_z plane to slow down the evaluation of I_{zz}^{SDP}, including both the double and single integrals in Eq. (4.13). This is generally the case for the TM reflected fields or for any "near-cutoff" guided mode. The resonant contribution of these poles may also be extracted to regularize the integrands. A complete analysis of the general case, in which poles of both R^{TM} and $\tilde{g}_x(s_z, s_y)$ are close to the saddle point of the integral, is somewhat involved technically; a detailed treatment is given in Appendix C. As the

electrical thickness of the multilayered medium increases, more poles of R^{TM} must be extracted to maintain a good convergence rate.

4.5 Discrete Spectrum

The discrete spectrum of guided modes must be included in the spectral expansion of the layered medium PGF. The propagation wavenumber k_{zn} of the n^{th} TM guided wave mode represents a pole in the TM reflection coefficient $R^{TM}(k_z)$. Such poles may be found numerically using a pole or root-finding algorithm for complex valued functions. The discrete spectrum of the n^{th} mode is found as the residue of the integral in Eq. (4.9) evaluated in the k_z plane at k_{zn}. The complete discrete spectrum DS_{zz}^{3D} of the zz component of $\mathbf{G}_R$ is then found by summing this residue over all poles k_{zn}:

$$DS_{zz}^{3D} = -\left(k_0^2 + \frac{\partial^2}{\partial z^2}\right)\frac{1}{2\pi^2\varepsilon}\sum_n \; 2\pi i \underset{k_z=k_{zn}}{res}\{R^{TM}(k_z)\}e^{ik_{zn}z}\int_0^\infty dk_y \cos(k_y y) g_x(x, k_{xn}, k_{x0}) \tag{4.14}$$

where $k_{xn} = (k_0^2 - k_{zn}^2 - k_y^2)^{1/2}$. The integral in Eq. (4.14) may be expressed in terms of the scalar PGF $G_F^{2D}(k_0, x, y, k_{x0}, L)$ for a linear array placed on the x axis in 2D free space. The expression for the discrete spectrum then simplifies to

$$DS_{zz}^{3D} = -\left(k_0^2 + \frac{\partial^2}{\partial z^2}\right)\frac{i}{\varepsilon}\sum_n \; \underset{k_z=k_{zn}}{res}\{R^{TM}(k_z)\}e^{ik_{zn}z}\, G_F^{2D}\left(\sqrt{k_0^2 - k_{zn}^2}, x, y, k_{x0}, L\right) \tag{4.15}$$

where the computation of G_F^{2D} is discussed in chapter 3 [42]. Note that G_F^{2D} is not evaluated at the free-space wavenumber k_0, but rather the guided wavenumber component $k_{\rho n} = (k_0^2 - k_{zn}^2)^{1/2}$, indicating that it accounts for radiation into that guided wave mode.

Although the expression (4.15) is accurate for the representation of Eq. (4.9), two important modifications are required for the accelerated integral representation of Eq. (4.11). First, in deforming the integration contours to the SDPs, the leaky wave poles are generally crossed and they must also be included in Eq.(4.15). On the other hand, if a guided wave mode is crossed, its contribution to the discrete spectrum must be excluded. Second, when a small number $2N_d + 1$ of sources near the unit cell of interest are excluded from the spectral integration, as described in Sec. 3.4.A, the same must be done for the discrete spectrum. That is, the computation of G_F^{2D} must be redefined so as not to include those source contributions.

4.6 Riemann Sheets

As with the free-space PGF, the reflected fields PGF $\mathbf{G}_R$ has an infinite number of branch cuts in the complex k_{x0} plane. These branch cuts result from its dependence on the transverse Floquet mode wavenumbers $k_{\rho m} = (k_0^2 - k_{xm}^2)^{1/2}$, where $k_{xm} = k_{x0} + 2\pi m/L$ in the Floquet series representation of Eq. (4.4) The discrete spectrum also contains square-root branch cuts of the form $(k_{xn}^2 - k_{xm}^2)^{1/2}$ for the n^{th}

guided wave mode, resulting from the 2D free-space periodic Green's function in Eq. (4.15). The sign of the square root is typically chosen so that $\mathrm{Im}\{k_{ym}\} \geq 0$ for all m, n, corresponding to diffraction modes that are proper, and decay exponentially away from the array. In this case the Green's function is said to be evaluated on the top Riemann sheet in the complex k_{x0} plane. To define a Green's function on an alternate Riemann sheet, one may choose $\mathrm{Im}\{k_{\rho m}\} < 0$ for a small number of Floquet modes. This choice may also be made with the discrete spectrum DS through the computation of $G_F^{2D}(\sqrt{k_0^2 - k_{zn}^2}, x, y, k_{x0}, L)$, which may also be represented as a Floquet series (Eq. (3.3)).

These branch cuts also exist in the spectral integral formulation of $\mathbf{G}_R$ (Eq.(4.9)) (or any representation of $\mathbf{G}_R$.) Mathematically, they result from the discontinuity of the integral in the k_y plane when the integration contour crosses a pole of the 1D PGF (see Appendix B). Up to this point, this integral representation of $\mathbf{G}_R$ has been presented for the top Riemann sheet. To define $\mathbf{G}_R$ on the lower Riemann sheet with respect to the m^{th} Floquet mode, one must evaluate $\mathbf{G}_R$ on the top Riemann sheet, then subtract the residue contribution of the m^{th} Floquet mode pole. That is, I_{zz}^{SDP} must be redefined as

$$I_{zz}^{SDP} \rightarrow I_{zz}^{SDP} - \underset{k_x = k_{xm}^{\pm}}{res} \{I_{zz}^{SDP}\} \tag{4.16}$$

where $\underset{k_x = k_{xm}^{\pm}}{res} \{I_{zz}^{SDP}\}$ is given in Eq.(4.12).

4.7 Numerical Implementation

This section discusses the numerical evaluation of the double SDP integrals of Eq. (4.11). The evaluation of the discrete spectrum via the 2D PGF, and of the contributions of the $2N_d+1$ sources near the unit cell both have well-known numerical implementations and are not discussed here. The SDP integral may be evaluated using a quadrature rule with equally spaced nodes for both integration variables. One may choose a discrete set of nodes s_{zq} and s_{yp} (with q and p integers) in the ranges $[-s_{z\max}, s_{z\max}]$ and $[0, s_{y\max}]$, where $s_{z\max}$ and $s_{y\max}$ are the truncation values for each integration. These finite ranges represent the contribution zones of the integrals, beyond which the integral has negligible value. The computation of the integral is then reduced to a discrete double summation, where each term is simply the integrand evaluated at nodes s_{zq}, s_{yp}, then multiplied by corresponding weights w_{zq}, w_{yp}. The integration of Eq. (4.11) then becomes

$$I_{zz}^{SDP} = \sum_{q,p}^{N_q,N_p} w_{zq} w_{yp} \left(k_0^2 + \frac{\partial^2}{\partial z^2}\right) \frac{-k_0}{\pi^2 \varepsilon} R^{TM}(k_z(s_{zq})) \frac{s_{zq}^2 - i}{\sqrt{s_{zq}^2 - 2i}} e^{-jk_z(s_{zq})z} \frac{\cos(k_y(s_{zq}, s_{yp})y)}{\sqrt{s_{yp}^2 + 2s_{zq}^2 - 2i}} \tilde{g}_x(s_{zq}, s_{yp}) \tag{4.17}$$

where N_q and N_p are number of nodes used in each integration. The error associated with this numerical integration depends on the number of nodes N_q and N_p used and the truncation values $s_{z\max}$ and $s_{y\max}$. Assuming that the exponential decay $\exp\left(-k_0 L(N_d+1)(s_z^2 + s_y^2)\right)$ dominates at the edge of the contributing zone, the

truncation values may be taken as $s_{z\max} = s_{y\max} = \Omega_s \big/ (\mathrm{Re}\{k_0\} \cdot L(N_d + 1))$ where $\Omega_s = O(1)$ is a dimensionless parameter, e.g. $\Omega_s = 6$ is generally sufficient for a single precision accuracy. The number of integration nodes N_q and N_p is then chosen to achieve the desired accuracy. In our implementation we choose $N_p \approx N_q \big/ 2$, as the integral over s_y is semi-infinite and requires half as many quadrature terms.

It should be noted that in addition to the double SDP integral, a small number of single integrals must be evaluated to find the residue contributions $res_{k_x = k_{xm}^{\pm}} \{I_{zz}^{SDP}\}$ and for the terms subtracted from I_{zz}^{SDP} to make it slowly varying (if required). These terms do not typically contribute significantly to the total computational cost, and may be evaluated using any integration method.

4.8 Numerical Results

This section presents results showing the accuracy and convergence of the proposed method for finding $\mathbf{G}_R^{3D}$. The case considered is an array of dipole sources placed directly on top of a dielectric slab in free space. Verification of this method to high accuracy presents some complications, however, as it requires a suitable reference solution found using either a Floquet series (Eq. (4.4)) or a spatial summation of single source Green's functions. Our method agrees well with the Floquet series representation only for very thin slabs, as the integrals required for the Floquet summation are problematic to evaluate. Even for thin slabs, single precision accuracy is hard to achieve.

For this reason we choose as a reference solution a spatial summation of single source Green's functions, assuming a small amount of loss in the ambient medium. This loss is realized by making k_0 complex, with $\mathrm{Im}\{k_0\} = -0.01\,\mathrm{Re}\{k_0\}$. Each term in the summation is evaluated to 10^{-12} accuracy. The introduced loss permits truncating the sum to 3000 terms, ensuring a truncation error of 10^{-11}.

Figure 4-2 shows the error of G_{Rxx} as a function of the number N_q of quadrature nodes used to evaluate the SDP integral. (The total number of summation terms in Eq. (4.17) is then $N_q N_p = N_q^2 / 2$.) Five sources in and near the unit cell are excluded from the integral and computed using the single source Green's function (i.e. $N_d = 2$) via the spectral method presented in [30]. The slab has relative permittivity $\varepsilon_d = 12.5 + .1i$, the array has spacing $L = 0.2\lambda$, and the dipoles are sequentially phase shifted with wavenumber $k_{x0} = 1.01\,\mathrm{Re}\{k_0\}$. The error is shown for three different values of the slab thickness $t:\ 0.1\lambda_d, 0.55\lambda_d$, and $1.05\lambda_d$, where $\lambda_d = \mathrm{Re}\{\lambda / \sqrt{\varepsilon_d}\}$ is the wavelength in the slab medium, for the observation point $x = 0.45L$, $y = z = 0.01L$.

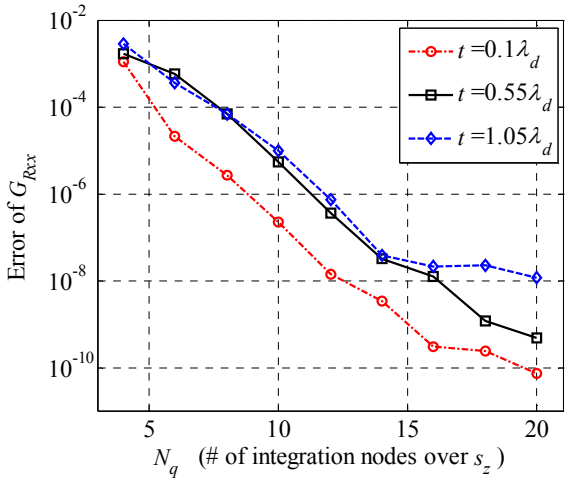

Fig. 4-2 Error of the field component G_{Rxx} versus N_q for array on top of a dielectric slab for 3 values of the slab thickness t.

It is evident that the convergence is fast for all slab thicknesses. The error is small even for very small values of N_q. For the slab thicknesses $0.1\lambda_d$, $0.55\lambda_d$, and $1.05\lambda_d$, the TM reflection coefficient has 1, 2, and 3 guided wave poles that must be included in the discrete spectrum, respectively, and 3, 4, and 4 poles whose resonant contribution must be subtracted to regularize the integrand for high accuracy solutions. Although these results are shown only for G_{Rxx}, the convergence rates of the other components of $\mathbf{G}_R$ are very similar.

Figure 4-3 shows the G_{Rxx}, G_{Ryy}, and G_{Rzz} field components over half the unit cell for a lossless version of the system considered above, with phase shift parameter $k_{x0} = (1.01 + .1i)k_0$ and slab thickness $t = 0.55\lambda_d$. Here the observation points are taken directly on both the surface and the array axis, and the source contribution at the

origin is excluded to avoid the field divergence. Unlike G_{Rzz}, the G_{Rxx} and G_{Ryy} components include both TE and TM fields.

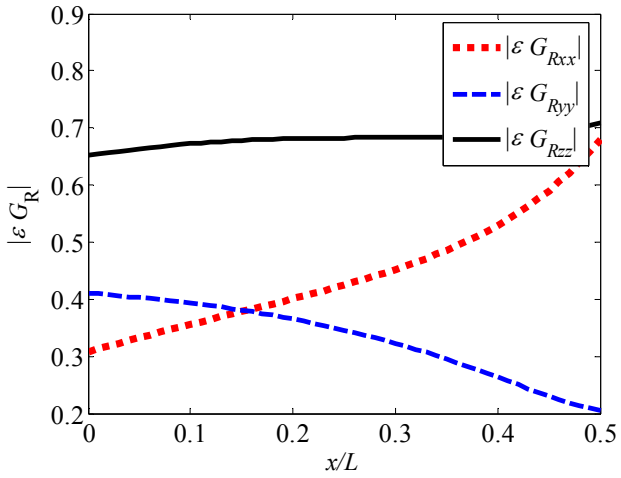

Fig. 4-3 Field components observed on the array axis and slab surface for a lossless system, plotted over half the unit cell with the source contribution at the origin removed.

Finally, Fig. 4-4 shows the convergence of the integral for a dense array with $L = .01\lambda$, in order to demonstrate low-frequency performance. The error of the PGF is shown at the observation point $x = 0.45L$, $y = z = 0.1L$ for three different values of N_d. A larger number of sources near the unit cell must be excluded from the integration and evaluated separately for the integral to achieve the same convergence as shown in Fig. 4-2. Therefore, the performance of the presented method deteriorates for very small periodicities. However, the performance is good for periodicities from several wavelength down to values as small as $\lambda/1000$, thus spanning the range used in most practical applications.

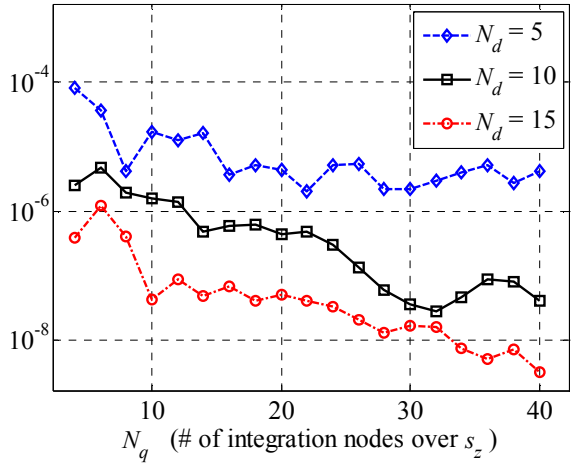

Fig. 4-4 Error of the field component G_{Rxx} versus N_q for a dense array with $L = .01\lambda$ on top of a dielectric slab for 3 values of the parameter N_d.

4.9 Evaluation of $\mathbf{G}_R^{2D}(\mathbf{r})$

This section considers the 2D version of the problem, in which a periodic array of line sources resides near a surface. Because the fields have no dependence in the y dimension, only the scalar PGF accounting for TE and TM reflections need be considered. Furthermore, there is only one dimension transverse to the periodicity axis, so the spectral representation involves only a single integral, similar to the free-space case discussed in chapter 3.

The Floquet series representation of the *free-space* Green's function G_F^{2D} is given by

$$G_F^{2D}(\mathbf{r}) = \frac{1}{L}\sum_{m=-\infty}^{\infty} \frac{i}{2k_{zm}} e^{ik_{xm}x} e^{ik_{zm}|z|}, \tag{4.18}$$

with $k_{xm} = k_{x0} + 2\pi m / L$ and $k_{zm} = \sqrt{k_0^2 - k_{xm}^2}$. This may easily extended to the case of an array of line sources near a surface. Finding the reflected fields scalar Green's function $G_R^{2D}(\mathbf{r})$ requires simply inserting the reflection coefficient into each series term, evaluated at the corresponding Floquet mode wavenumber component:

$$G_{R^{TE,TM}}^{2D}(\mathbf{r}) = \frac{1}{L}\sum_{m=-\infty}^{\infty} \frac{i}{2k_{zm}} e^{ik_{xm}x} e^{ik_{zm}|z|} R^{TE,TM}(k_{zm}). \tag{4.19}$$

As with the 3D case, however, this series converges very slowly when the observation point is close to the array and surface.

An alternative is to use the spectral representation of $G_F^{2D}(\mathbf{r})$ developed in chapter 3. $G_{R^{TE,TM}}^{2D}(\mathbf{r})$ is found by inserting the reflection coefficient into the spectral integral in (3.7) (recall the coordinate system has been changed) to find

$$G_{R^{TE,TM}}^{2D}(\mathbf{r}) = \frac{1}{2\pi}\int_{-\infty}^{\infty} dk_z R^{TE,TM}(k_z) e^{ik_z z} g_x(x, k_x) + DS_{R^{TE,TM}}^{2D} \tag{4.20}$$

where $k_x = \sqrt{k_0^2 - k_z^2}$ and $DS_{R^{TE,TM}}^{2D}$ represents the discrete sum of guided wave modes supported by the surface medium. The integral in Eq. (4.20) is simply a plane wave expansion of the fields, with $R^{TE,TM}(k_z)$ inserted to find the (TE,TM) reflection of each plane wave component. It may be regularized and evaluated using the exact same procedure outlined in chapter 3, sections 3.3 and 3.4, and detailed derivations are not provided here. The only modification that may be required is accounting for simple poles in the reflection coefficient that may reside near the saddle point of the integration. These poles correspond to guided and leaky wave modes in the surface medium, and their

contribution may be extracted and integrated in closed form using the same procedure used for the poles of $g_x(x,k_x(k_z))$. The discrete spectrum $DS^{2D}_{R^{TE,TM}}$ is simply found by taking the residue of the integrand in Eq. (4.20) for each guided wave pole $k_{zn}^{TE,TM}$, and summing them:

$$DS^{2D}_{R^{TE,TM}} = i\sum_n \underset{k_z=k_{zn}^{TE,TM}}{res}\{R^{TE,TM}(k_z)\}e^{ik_{zn}^{TE,TM}z}g_x(x,k_{xn}^{TE,TM}) \tag{4.21}$$

Because $g_x(x,k_{xn})$ is known in closed form, its evaluation is trivial.

Demonstrating the accuracy of this code is straightforward compared to the 3D case, as the Floquet representation (4.19) can easily be computed to high accuracy for $z>0$, even for lossless systems and complex k_{x0}. Figure 4-5 shows the convergence of $G^{2D}_{R^{TE}}$ and $G^{2D}_{R^{TM}}$ for the same configuration considered in Fig. 4-2, except the ambient medium is chosen to be lossless (i.e., real k_0) and $k_{x0}=(1.01-0.1i)k_0$.

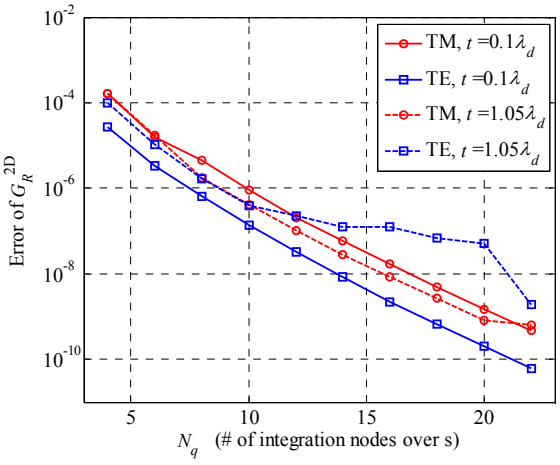

Fig. 4-5 Error of the field component $G^{2D}_{R^{TE,TM}}$ versus N_q for an array on top of a dielectric slab for 2 values of the slab thickness t. The structure has the same parameters considered in Fig. 4-2, except k_0 is real and $k_{x0}=(1.01-0.1i)k_0$

4.10 Traveling Waves on Resonant Arrays Near surfaces

With the periodic Green's function one can find the traveling wave modes of periodic arrays near surfaces. In this section we consider a 3D configuration consisting of an array of gold plasmonic nanoparticles with polarizability $\boldsymbol{\alpha}$ that are small enough compared to the wavelength that they behave as point dipole sources. The nanoparticles are embedded in an infinite dielectric medium, and situated near a slab of denser dielectric material (see Fig. 4-6). For a given problem geometry, one can solve the dispersion equation (2.11), modified to account for the surface interaction.

$$\det\left(\mathbf{G}_F^{3D}(\mathbf{0}) + \mathbf{G}_R^{3D}(2h\hat{\mathbf{z}}) - \mathbf{G}_0(\mathbf{0}) - \boldsymbol{\alpha}^{-1}\right) = 0 \tag{4.22}$$

As discussed in section 2.4, those values of k_{x0} that solve Eq. (4.22) represent the propagation wavenumbers of traveling wave modes supported by the periodic structure. If the polarizability tensor $\boldsymbol{\alpha}$ is diagonal (i.e. the particle principle axes are aligned with the coordinate axes defined in Fig. 4-1) the modes can be divided into separate TE and TM types. The Green's function $\mathbf{G}_R^{3D}(2h\hat{\mathbf{z}})$ used in this equation, which accounts for the surface interaction, has four matrix elements that are zero, corresponding to the off-diagonal elements associated with the y direction. If $\boldsymbol{\alpha}$ is diagonal, this indicates that the polarization states in the y direction (i.e. parallel to the surface but transverse to the array) are not coupled to polarization along the x and z directions. Wave modes polarized in this way therefore satisfy the scalar dispersion relation $G_{Fyy}^{3D}(\mathbf{0}) + G_{Ryy}^{3D}(2h\hat{\mathbf{z}}) - G_{0yy}^{3D}(\mathbf{0}) - 1/\alpha_{yy} = 0$. The surface interaction for this mode is dominated by the TE reflection coefficient. In contrast, the polarization states along the

x and z directions are coupled to each other through the surface interaction, which is dominated by the TM reflection coefficient. There are therefore two coupled dispersion equations for the TM traveling wave modes, and each solution has nonzero polarization components in the x and z directions.

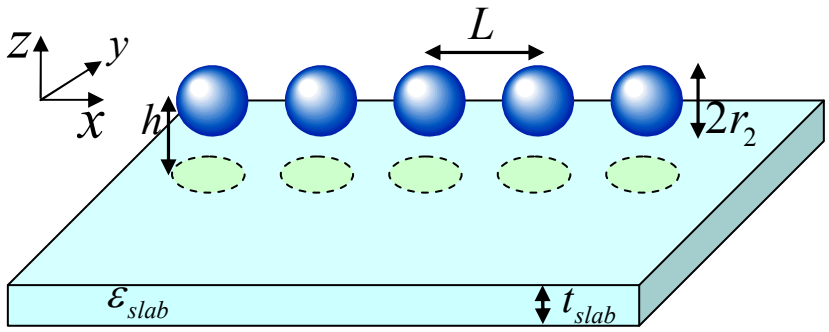

Fig. 4-6 A periodic array of nanoparticles oriented near a surface

Consider a nanoparticle chain near a slab that is sufficiently thin compared to the wavelength λ_d in the slab that it supports only one TM and one TE guided mode. For simplicity, the remainder of this section considers the y polarized traveling waves, though the general features also apply to the other wave types. Figure 4-7 shows, in the complex k_{x0} plane, the solutions of the dispersion equation for the y polarized traveling wave modes, along with the branch cuts. The square root branch cuts have branch points at the free-space wavenumber $\pm k_0$ and the TE mode wavenumber $\pm k_x^{TE}$. Recall that the latter branch points result from the evaluation of the discrete spectrum of $\mathbf{G}_R^{3D}$. Fig. 4-7 shows them with a small amount of loss added to the slab and ambient dielectric media to enhance visibility. (For the lossless case, each branch cut moves from the branch point to the origin along the real axis, then follows the imaginary axis.)

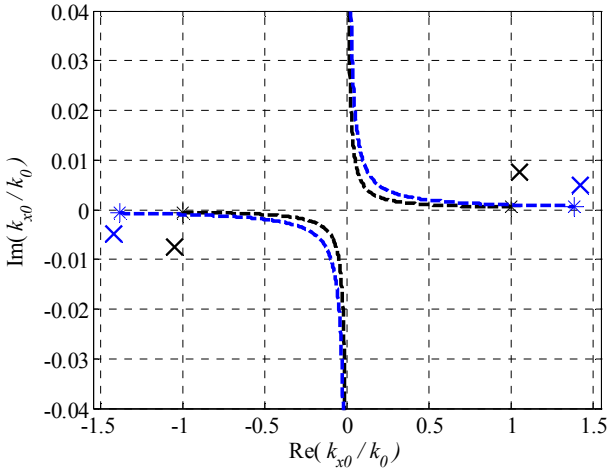

Fig. 4-7 Branch cuts of G_{Ryy}^{3D} and solutions of dispersion equation in complex k_{x0} plane

There exist two independent solutions to the dispersion equation for this y polarized case. Both solutions are found close to branch points, as is typically the case for resonant arrays. The first, found close to k_0, is mediated by free-space interactions among the array elements, and has wavenumber β_F. For a periodic array in free space, this solution and the branch cuts stemming from $\pm k_0$ would complete the picture. The surface interaction, however, introduces another solution, β_{TE}, found close to the branch point at k_x^{TE}, that represents a wave mediated by the slab's TE mode. For dense, lossless arrays, it is found directly on the real axis, indicating a slow wave mode with no radiative losses. The other solution, corresponding to free-space interaction, cannot be purely real. Because its real part is less than k_x^{TE}, it radiates into the TE guided wave mode. In this sense it is a leaky wave. Indeed, the solution itself is not found on the top Riemann sheet;

it is on the lower Riemann sheet with respect to the branch cut stemming from k_x^{TE}. Note that if this were not this case, this solution would essentially be blocked from the real axis by the branch cut, and would not be excitable or observable (see Fig. 4-7). This feature is typical of leaky-wave modes, except that in this case it results from radiation into the slab medium, not into free space.

The remainder of this section will demonstrate the radiation and propagation properties of this system by analyzing a finite nanoparticle array excited by an external source. Consider an array of N gold nanoshells of permittivity ε_m, assumed to follow the Drude model [32], with a silicon dioxide core of permittivity $\varepsilon_d = 2.37\varepsilon_0$. The shell's inner and outer radii are r_1 and r_2 and it is assumed that $r_1, r_2 \ll \lambda$, where λ is the vacuum wavelength. Individual nanoshells support plasmonic resonances whose resonant wavelengths are determined by ε_m and the ratio r_1/r_2. Each shell is located a distance h above a silicon slab of permittivity $\varepsilon_{slab} = 12.5\varepsilon_0$ and thickness t_{slab} (Fig. 4-6). The entire structure is embedded in a silicon dioxide medium. The first shell of the array is assigned a fixed polarization to simulate a localized source excitation. The periodic Green's function cannot be used to analyze this finite structure, so it is instead solved as an N body problem. The dyadic Green's function for a single source in a layered medium $\mathbf{G}_{R0}(\mathbf{r})$ is used to find the interaction among the shells, and to set up a self-consistent matrix equation for each nanoshell's polarization. $\mathbf{G}_{R0}(\mathbf{r})$ is found by evaluating the

Sommerfeld spectral integrals, which are accelerated using steepest descent path integration [30].

Consider an array with $N = 200$ shells with parameters $r_2 = 23nm$, $r_1 = 16nm$, $L = 80nm$, $h = 100nm$, $t_{slab} = 148nm$, and free-space wavelength $\lambda = 520nm$ (Fig. 4-6). For the chosen parameters the shells have a resonance at $\lambda = 495nm$, and the slab supports a single TE mode with wavenumber $k_x^{TE} = 1.39k_0$. After solving for the polarization of each nanoshell in response to the localized dipole excitation, we find the wavenumber content of the traveling wave modes propagating along the array by identifying the strong resonant peaks in the Fourier spectrum of shell polarization states. With the excitation pointing in the y direction, the polarization of all the shells is also directed along the y direction. Fig. 4-8 shows the spectrum corresponding to the discrete Fourier transform of y polarization states. The contribution of the 15 shells closest to the source is excluded so that the direct contribution of the source to the spectrum is minimized, thus highlighting the modal field contribution. The spectrum clearly shows two peaks, as expected. One is found near the free-space wavenumber, and the other near the TE guided mode wavenumber, as predicted.

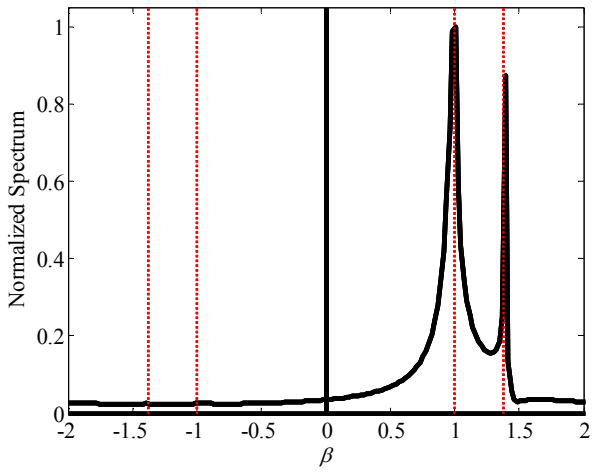

Fig. 4-8 Fourier Spectrum of TE polarization states for a plasmonic nanoparticle array excited by a localized source. Resonant peaks correspond to free-space and TE surface interactions.

The TM polarized case, which can be excited by a z directed dipole source, shows similar behavior. Figure 4-9 shows the dispersion relations for both TE and TM waves on this nanoparticle chain. They are found by tracking the spectral peaks in Fig. 4-8 for a range of free-space wavenumbers near (but below) the particle resonant frequency. The wavenumber of the TM guided mode supported by the slab has a lower propagation constant compared to the TE mode, so the corresponding wave supported by the array is closer to the light line.

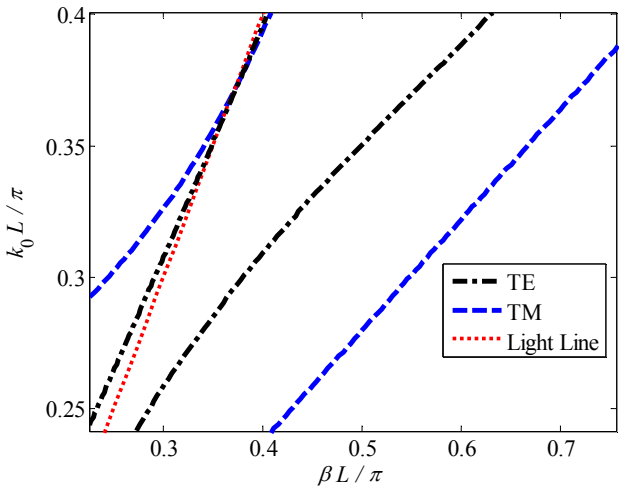

Fig. 4-9 Dispersion of TE and TM traveling wave modes supported by a nanoparticle array near a dielectric slab

The traveling wave modes that are mediated by free-space interaction radiate into the slab occurs an angle ϕ with the array axis that satisfies the phase matching condition $\cos(\phi_{rad}) = \mathrm{Re}\{\beta_F / k_x^{TE}\}$. For the parameters considered, this occurs at $\phi_{rad} = 0.75$ for the TE case. Figure 4-10 shows the electric field strength on an arc far from the array, a distance h above the array, resulting from a TE polarized wave. At this distance, the fields close to the surface are dominated by the guided wave component. The field pattern clearly shows a peak at an angle $\phi = 0.77$, close to the predicted radiation angle.

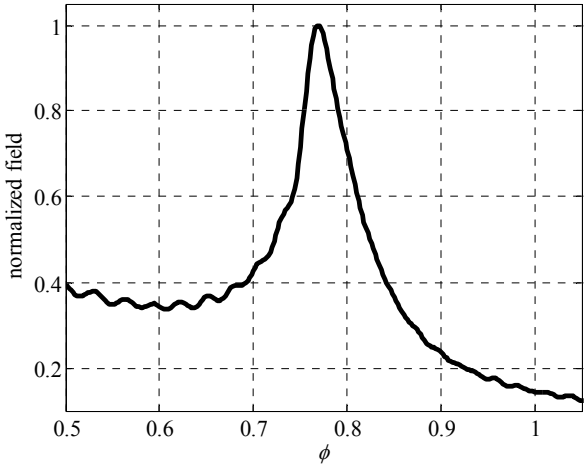

Fig. 4-10 Electric field strength versus observation angle, showing the radiation pattern of a nanoparticle chain into the TE guided mode of the dielectric slab.

For many practical applications, the radiation into the slab medium represents a type of power loss and, in finite slabs, interference resulting from reflections of the guided wave beam off the slab edges. However, the observed phenomena also suggest possible applications in devices that make use of coupling between guided waves and periodic structures, such as surface wave launchers and leaky-wave antennas [35, 43]. It presents the possibility of extending known methods of controlling radiation into free-space (i.e. antennas) to controlling radiation patterns into the guided waves supported by surfaces.

4.11 Conclusions

An alternative dyadic PGF representation has been presented to find the electric fields resulting from an array of electric dipole sources on or near a planarly layered medium. It is based on a plane-wave expansion of the scalar periodic Green's function,

formulated as a spectral integral, and a series that accounts for the discrete spectrum of guided wave modes. Formulations for both 2D and 3D configurations are presented. This representation is accurate for observation points close to and directly on the array axis and surface, including surfaces composed of gain and lossy media. It is furthermore accurate for complex phase shifts between sources and may be defined on alternate Riemann sheets with respect one or more Floquet modes. These properties make the spectral integral representation particularly well-suited to finding the complex dispersion relations of traveling wave modes supported by linear periodic arrays, as well as scattering by both near and far-field external sources. It has the potential to greatly accelerate the computational analysis and design of surface traveling wave structures and printed leaky-wave antennas.

This Green's function method may furthermore be used to study the ways in which traveling waves radiate into the guided wave modes of planarly stratified surfaces. The presented analysis shows that periodic structures support distinct wave modes: one that is mediated by free-space interactions, and is generally a leaky-wave with respect to the surface, and one or more that are mediated by the guided wave modes supported by the surface.

4.12 Appendix

A. Dyadic Components of $\mathbf{G}_R^{3D}$

This section extends Eq. (4.9) to all the dyadic components of $\mathbf{G}_R^{3D}$. Each of these integral expressions may be regularized and evaluated numerically as described in sections 4.4-4.7.

$$
\begin{aligned}
G_{Rzx}^{3D} &= \left(\frac{\partial^2}{\partial z \partial x}\right)\frac{1}{2\pi^2\varepsilon}\int_{-\infty}^{\infty} dk_z R^{TM}(k_z) e^{ik_z z}\int_0^{\infty} dk_y \cos(k_y y) g_x(x,k_x,k_{x0}) + DS_{zx}^{3D} \\
G_{Rxz}^{3D} &= -G_{Rzx}^{3D} \\
G_{Rzy}^{3D} &= \left(\frac{\partial^2}{\partial z \partial y}\right)\frac{1}{2\pi^2\varepsilon}\int_{-\infty}^{\infty} dk_z R^{TM}(k_z) e^{ik_z z}\int_0^{\infty} dk_y \cos(k_y y) g_x(x,k_x,k_{x0}) + DS_{zy}^{3D} \\
G_{Ryz}^{3D} &= -G_{Rzy}^{3D} \\
G_{Rxx}^{3D} &= \frac{1}{2\pi^2\varepsilon}\int_{-\infty}^{\infty} dk_z \left(-k_z^2 R^{TM}(k_z)\frac{\partial^2}{\partial x^2} - k_0^2 R^{TE}(k_z)\frac{\partial^2}{\partial y^2}\right)\frac{e^{ik_z z}}{k_0^2 - k_z^2} \\
&\quad \times \int_0^{\infty} dk_y \cos(k_y y) g_x(x,k_x,k_{x0}) + DS_{xx}^{3D} \\
G_{Ryy}^{3D} &= \frac{1}{2\pi^2\varepsilon}\int_{-\infty}^{\infty} dk_z \left(-k_z^2 R^{TM}(k_z)\frac{\partial^2}{\partial y^2} - k_0^2 R^{TE}(k_z)\frac{\partial^2}{\partial x^2}\right)\frac{e^{ik_z z}}{k_0^2 - k_z^2} \\
&\quad \times \int_0^{\infty} dk_y \cos(k_y y) g_x(x,k_x,k_{x0}) + DS_{yy}^{3D} \\
G_{Ryx}^{3D} &= \frac{1}{2\pi^2\varepsilon}\int_{-\infty}^{\infty} dk_z \frac{e^{ik_z z}}{k_0^2 - k_z^2}\left(-k_z^2 R^{TM}(k_z) + k_0^2 R^{TE}(k_z)\right)\frac{\partial^2}{\partial x \partial y} \\
&\quad \times \int_0^{\infty} dk_y \cos(k_y y) g_x(x,k_x,k_{x0}) + DS_{yx}^{3D} \\
G_{Rxy}^{3D} &= G_{Ryx}^{3D}
\end{aligned}
\tag{4.23}
$$

B. Residues of Double Spectral Integral

The simplest way to evaluate the residue of the integrals in Eq. (4.9) at the poles of $g_x(x,k_x,k_{x0})$ is to change the integration variables into a polar form through the following transformation:

$$k_z = k_\rho \sin\alpha, \quad k_y = k_\rho \cos\alpha, \quad k_x = \sqrt{k_0^2 - k_\rho^2} \tag{4.24}$$

The integral for the zz component then becomes

$$\frac{-1}{4\pi^2\varepsilon}\left(k_0^2 + \frac{\partial^2}{\partial z^2}\right)\int_{-\pi}^{\pi} d\alpha \int_0^{\infty} dk_\rho k_\rho R^{TM}(k_\rho \sin\alpha)\exp\left(ik_\rho \rho\cos(\alpha-\phi)\right) g_x\left(x, \sqrt{k_0^2 - k_\rho^2}, k_{x0}\right) \tag{4.25}$$

where $\tan(\phi) = z/y$ and $\rho = (z^2 + y^2)^{1/2}$. The important simplification here is that $g_x(x, k_x, k_{x0})$ does not depend on α, and has poles only in the k_ρ plane. One may simply evaluate the residue of the integrand in the k_ρ plane and then integrate this residue over the angular variable α to recover the result given in Eq.(4.12).

One problem that must be considered is how to determine if a pole is crossed by the double SDP integral (i.e., when a pole's residue contribution should be included). In our formulation the integration in the k_y plane is done first, but the integration path depends on k_z through the coordinate transform in Eq. (4.10). This means that a pole may be crossed in the k_y plane for some values of k_z, but not others. This transition, for a given pole, represents a discontinuity of the integrand in the k_z plane (i.e. the integrand of the second spectral integration). The m^{th} Floquet mode pole therefore has a corresponding pair of branch cuts in the k_z plane whose path is defined by $\mathrm{Im}\{k_0^2 - k_{xm}^2 - k_z^2\} = 0$. Note that these branch cuts also appear in the Floquet series representation of Eq.(4.4). The branch cuts have branch points at $k_{zm}^{\pm} = \pm(k_0^2 - k_{xm}^2)^{1/2}$. *A pole's residue contribution must be included if the SDP crosses this pair of branch cuts*

in the k_z plane. It may be shown that only the poles at k_{xm}^{+} can contribute if $\mathrm{Im}\{k_{x0}\} > 0$, while only the poles at k_{xm}^{-} contribute if $\mathrm{Im}\{k_{x0}\} < 0$.

It is interesting to note that the residue contribution may also be derived by finding the residue of the k_y integral (with k_z treated as a constant) and integrating it in the complex k_z plane. The integration path must start at the branch point $k_{zm}^{-} = -(k_0^2 - k_{xm}^2)^{1/2}$ and go to the other branch point $k_{zm}^{+} = (k_0^2 - k_{xm}^2)^{1/2}$, where it crosses to the lower Riemann sheet and returns to $k_{zm}^{-} = -(k_0^2 - k_{xm}^2)^{1/2}$. In the coordinate transform to the angular spectrum (4.24), the integrand does not explicitly contain these branch cuts, so the residue evaluation is more straightforward; the result, however, is the same.

C. Extracting Residue Contribution of Poles

Suppose that in order to regularize the double integral in (4.11), the resonant part of multiple poles of both $\tilde{g}_x(s_z, s_y)$ (found at $\pm s_{ym}$) and $R^{TM}(k_z(s_z))$ (denoted by s_{zn}) must be extracted from the integrand, then integrated separately. One may begin this process with Eq. (4.13), in which only the singularities at $\pm s_{ym}$ are subtracted. Both terms in Eq. (4.13) contain integrals over s_z that must be regularized with respect to the reflection coefficient. Following the same procedure, and extending it to the case of multiple poles of both terms, one obtains Eq. (4.26) below. The first two lines represent the nonresonant double integral. The third line is a single integral, in which the resonant

terms of $\tilde{g}_x(s_z, s_y)$ have been integrated. The fourth and fifth lines represent a regularized single integral over s_z, and the last term is simply a sum of the integrated resonant components from the previous term.

$$
\begin{aligned}
I_{zz}^{SDP} = & \int_{-\infty}^{\infty} ds_z R^{TM}(k_z(s_z)) \int_0^{\infty} ds_y \left(f_{zz}(s_z, s_y) - \sum_m 2s_{ym} \frac{res_{s_y=s_{ym}} \{f_{zz}(s_z, s_y)\}}{s_y^2 - s_{ym}^2} \right) e^{-k_0 L(N_d+1)(s_z^2+s_y^2)} \\
& - \sum_n \int_{-\infty}^{\infty} ds_z \int_0^{\infty} ds_y \left(f_{zz}(s_{zn}, s_y) - \sum_m 2s_{ym} \frac{res_{s_y=s_{ym}} \{f_{zz}(s_z, s_y)\}}{s_y^2 - s_{ym}^2} \right) \frac{res_{s_z=s_{zn}} \{R^{TM}(k_z(s_z))\}}{s_z - s_{zn}} e^{-k_0 L(N_d+1)(s_z^2+s_y^2)} \\
& + \sum_n \int_0^{\infty} ds_y \left(f_{zz}(s_{zn}, s_y) - \sum_m 2s_{ym} \frac{res_{s_y=s_{ym}} \{f_{zz}(s_{zn}, s_y)\}}{s_y^2 - s_{ym}^2} \right) res_{s_z=s_{zn}} \{R^{TM}(k_z(s_z))\} \pi \\
& \qquad \times \frac{erfc\left(-i\sqrt{k_0 L(N_d+1)}\, \mathrm{sgn}(\mathrm{Re}\{-is_{zn}\}) s_{zn}\right)}{-i\, \mathrm{sgn}(\mathrm{Re}\{-is_{zn}\})} e^{-k_0 L(N_d+1)(s_{zn}^2+s_y^2)} \\
& + \int_{-\infty}^{\infty} ds_z R^{TM}(k_z(s_z)) \sum_m res_{s_y=s_{ym}} \{f_{zz}(s_z, s_y)\} \pi \frac{erfc\left(-i\sqrt{k_0 L(N_d+1)}\, \mathrm{sgn}(\mathrm{Re}\{js_{ym}\}) s_{ym}\right)}{-i\, \mathrm{sgn}(\mathrm{Re}\{js_{ym}\})} e^{-k_0 L(N_d+1)(s_z^2+s_{ym}^2)} \\
& - \int_{-\infty}^{\infty} ds_z \sum_n \frac{res_{s_z=s_{zn}} \{R^{TM}(k_z(s_z))\}}{s_z - s_{zn}} \sum_m res_{s_y=s_{ym}} \{f_{zz}(s_{zn}, s_y)\} \\
& \qquad \times \pi \frac{erfc\left(-i\sqrt{k_0 L(N_d+1)}\, \mathrm{sgn}(\mathrm{Re}\{-is_{ym}\}) s_{ym}\right)}{-i\, \mathrm{sgn}(\mathrm{Re}\{-is_{ym}\})} e^{-k_0 L(N_d+1)(s_z^2+s_{ym}^2)} \\
& + \sum_m \pi \frac{erfc\left(-i\sqrt{k_0 L(N_d+1)}\, \mathrm{sgn}(\mathrm{Re}\{-is_{ym}\}) s_{ym}\right)}{-i\, \mathrm{sgn}(\mathrm{Re}\{js_{ym}\})} \sum_n res_{s_y=s_{ym}} \{f_{zz}(s_{zn}, s_y)\} \; res_{s_z=s_{zn}} \{R^{TM}(k_z(s_z))\} \\
& \qquad \times \pi \frac{erfc\left(-i\sqrt{k_0 L(N_d+1)}\, \mathrm{sgn}(\mathrm{Re}\{-is_{zn}\}) s_{zn}\right)}{-i\, \mathrm{sgn}(\mathrm{Re}\{-is_{zn}\})} e^{-k_0 L(N_d+1)(s_{zn}^2+s_{ym}^2)}
\end{aligned}
\tag{4.26}
$$

4.13 Acknowledgements

The text of Chapter 4, in part, is a reprint of the material as it appears in the following publication: Derek Van Orden and Vitaliy Lomakin, “Rapidly convergent

representation for the periodic Green's function of a linear array in layered media" accepted for publication in IEEE transactions on Antennas and Propagation in August 2011. The dissertation author was the primary researcher and the co-author listed in this publication directed and supervised the research which forms the basis for this chapter.

Chapter 5 Twisted Periodic Arrays

5.1 Introduction

This chapter presents a new type of periodic structure, a linear array of particles that are sequentially rotated about the array axis by a constant angle (Fig. 5-1(b,c)). These "twisted" arrays support both guided and leaky-wave modes, and offer a new dimension of polarization control to periodic structures. Such polarization control is an important aspect of manipulating and controlling electromagnetic waves. Chiral media, including optically active liquid crystals [44-46], and artificial surfaces and media [47-50] allow polarization control but are not intended to support waveguidance or radiation. Helical antennas rely on polarization rotation properties to support waveguidance and radiation [51]. Another class of structures resulting in optical activity and waveguidance is chiral waveguides [52] and chiral fibers [53-55]. Such configurations lead to optical activity properties similar to those of liquid crystals but with benefits of a guiding structure.

Twisted arrays have similarities with cholesteric liquid crystal media, chiral optical fiber gratings, and helical antennas. They are unique, however, in that their cross-sectional size can be small, they can support modes with a large wavenumber, and support both waveguidance and radiation. Unlike bulk media, these structures may exhibit leaky-wave radiation transverse to the axis of propagation. Because their symmetry is discrete, twisted arrays retain the properties of general periodic structures, including the existence of diffraction modes that may couple to form stopbands. In contrast, structures with continuous helical symmetry, such as chiral fiber gratings and helical antennas, do not exhibit diffraction modes [51].

This chapter presents a thorough analysis of the electromagnetic properties of twisted arrays. A theoretical analysis with both a dyadic Green's function and closed form analytical expressions for modal fields is given for a twisted array of small elements modeled as point dipole elements. Propagation and radiation properties of finite twisted arrays are then analyzed, including "tilted" arrays (Fig. 5-1(c)) in which the longitudinal modes are coupled to the twist. The analysis of finite twisted arrays is given both for small elements modeled via their polarizabilities and for half-wave dipole rods modeled as thin wires via an electric field integral equation solver.

5.2 Dispersion Equations of Twisted Arrays

Consider an array of asymmetric elements with spacing L oriented along the z axis, as in Fig. 5-1. (We revert to the convention of chapter 2, where the periodicity axis is the z axis.) The n^{th} element is rotated about the z axis by an angle $\phi_0 n$ such that positive values of the rotation increment ϕ_0 indicate a right handed twist. In the case where the elements are small compared to the wavelength, each particle behaves as a point dipole source with dipole moment $\mathbf{p} = \boldsymbol{\alpha} \cdot \mathbf{E}$ in response to an external field $\mathbf{E}$, where $\boldsymbol{\alpha}$ is the particle polarizability tensor. For plasmonic nanoparticles in the near-infrared or visible optical regime, each particle has distinct plasmonic resonances corresponding to different principal axes of $\boldsymbol{\alpha}$, while in the microwave regime, similar resonant properties can be supported by subwavelength rods loaded by a resonant lumped circuit. This section presents a dyadic Green's function for this system, and a resulting dispersion equation.

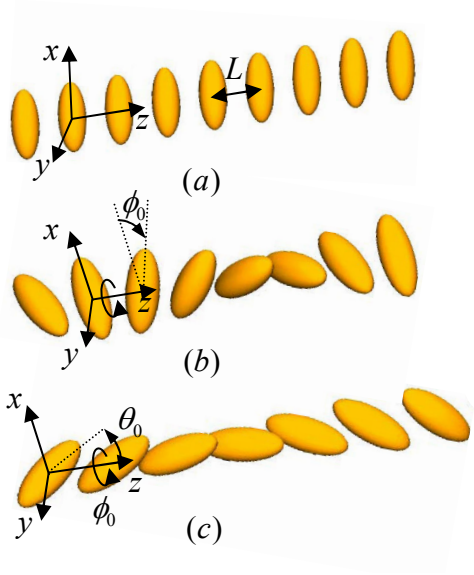

Fig. 5-1 : (a) A parallel array of asymmetric elements. (b) A twisted array with each particle sequentially rotated an angle ϕ_0 around the array axis. (c) A "tilted" twisted array, in which the major axis of each particle is tilted at an angle θ_0 with the array axis.

For a twisted array, the self-consistency equations and dispersion relations can be obtained by generalizing the derivations in chapter 2, section 4, to include the sequential rotation boundary conditions. In a twisted array the induced polarization of each particle must be symmetric under translation by L, a phase shift of $e^{ik_{z0}L}$, and a rotation by ϕ_0 about the z axis. That is, the dipole moment $\mathbf{p}_n$ of the n^{th} particle must satisfy

$$\hat{\mathbf{R}}_z\left(\phi_0\right)\mathbf{p}_n e^{ik_{z0}L} = \mathbf{p}_{n+1} \tag{5.1}$$

where $\hat{\mathbf{R}}_z$ is the matrix for rotations about the z axis. The symmetry properties in Eq. (5.1) are satisfied by particle dipole moments of the form

$$\mathbf{p}_n = \left(\begin{pmatrix}\cos(n\phi_0)\\ \sin(n\phi_0)\\ 0\end{pmatrix}p_{x0} + \begin{pmatrix}-\sin(n\phi_0)\\ \cos(n\phi_0)\\ 0\end{pmatrix}p_{y0} + \begin{pmatrix}0\\ 0\\ 1\end{pmatrix}p_{z0}\right)e^{ik_{z0}nL} \tag{5.2}$$

where the $n = 0$ particle has dipole moment $\mathbf{p}_0 = p_{x0}\hat{\mathbf{x}} + p_{y0}\hat{\mathbf{y}} + p_{z0}\hat{\mathbf{z}}$. The first two terms in Eq. (5.2) describe transverse dipole vectors that rotate at the same rate as the array elements. In cases where the polarizability along one axis is significantly greater than that along the others, as may occur near a resonance, one of these two terms will dominate. The third term represents the longitudinal wave component, and the extent to which it couples to the transverse components depends on the particle orientation, as will be discussed in subsequent sections.

The fields resulting from a twisted array can be found, similar to Eq. (3.1), as an infinite sum of dipole source contributions but with the dipole moments rotated according to Eq.(5.2):

$$\mathbf{E}(\mathbf{r}) = \sum_{n=-\infty}^{\infty} e^{ik_{z0}nL}\mathbf{G}_0(\mathbf{r} - nL\hat{\mathbf{z}}, k_0)\begin{pmatrix} p_{x0}\cos(n\phi_0) - p_{y0}\sin(n\phi_0) \\ p_{x0}\sin(n\phi_0) + p_{y0}\cos(n\phi_0) \\ p_{z0} \end{pmatrix} \tag{5.3}$$

Based on this equation, a new Green's function for twisted arrays may be developed by incorporating the sequential rotation of ϕ_0 into the linear phase shift applied to each array element. This is accomplished by expressing the sine and cosine functions in Eq. (5.3) in their exponential forms, and then absorbing them into the linear phase shift factor $e^{ik_{z0}nL}$ of the appropriate matrix elements. The resulting equation may be expressed in terms of the components of the dyadic periodic Green's function $\mathbf{G}(\mathbf{r}, d, k_0, k_{z0})$ evaluated with distinct phase shift factors. The expression for the electric field in Eq. (5.3) then becomes

$$\mathbf{E}(\mathbf{r}) = \frac{1}{2}\begin{pmatrix} G_{xx}^{+} + G_{xx}^{-} - i(G_{xy}^{+} - G_{xy}^{-}) & G_{xy}^{+} + G_{xy}^{-} + i(G_{xx}^{+} - G_{xx}^{-}) & 2G_{xz} \\ G_{yx}^{+} + G_{yx}^{-} - i(G_{yy}^{+} - G_{yy}^{-}) & G_{yy}^{+} + G_{yy}^{-} + i(G_{yx}^{+} - G_{yx}^{-}) & 2G_{yz} \\ G_{zx}^{+} + G_{zx}^{-} - i(G_{zy}^{+} - G_{zy}^{-}) & G_{zy}^{+} + G_{zy}^{-} + i(G_{zx}^{+} - G_{zx}^{-}) & 2G_{zz} \end{pmatrix}\mathbf{p}_0 \qquad (5.4)$$

where $\mathbf{G}^{\pm} = \mathbf{G}(\mathbf{r}, L, k_0, k_{z0} \pm \phi_0 / L)$. The matrix in Eq. (5.4) is interpreted as the dyadic Green's function $\mathbf{G}_{twisted}(\mathbf{r}, L, \phi_0, k_0, k_{z0})$ for a *twisted* array of dipole sources with spacing L, rotation angle ϕ_0, and linear phase shift $k_{z0}L$.

With the Green's function established, the traveling wave modes may be identified, as in section 2, by finding the fields resulting from the array at the origin and matching them to the dipole moment $\mathbf{p}_0$ of the particle centered there. The mode wavenumbers β are found by solving the resulting self-consistent equation, which is similar to Eq. (2.11) but with a new Green's function:

$$\det\left(\mathbf{G}_{twisted}(\mathbf{0}, L, \phi_0, k_0, k_{z0}) - \mathbf{G}_0(\mathbf{0}, k_0) - \boldsymbol{\alpha}^{-1}\right) = 0. \qquad (5.5)$$

Similar to the array of parallel elements considered in section 2.4, each independent solution of Eq. (5.5) has an infinite number of diffraction orders spaced by $2\pi / L$ in the complex k_{z0} plane. This is true despite the fact that the spacing L is not the spatial period of a twisted array in a Cartesian reference frame. In a helical coordinate system, however, the spacing L is the structure's period, which leads to the existence of diffraction orders. Note that Eq. (5.5) involves the components of three periodic Green's functions ($\mathbf{G}$, $\mathbf{G}^{\pm}$) with three different linear phase shift factors ($k_{z0}, k_{z0} \pm \phi_0 / L$). From the Floquet mode representation of the periodic Green's function (3.3) it is clear that the resulting determinant has branch points in the complex k_{z0} plane at $\pm k_0 + 2\pi m / L$,

$\pm k_0 - \phi_0 / L + 2\pi m / L$, and $\pm k_0 + \phi_0 / L + 2\pi m / L$, with m an integer. The presence of six branch cuts per Floquet mode is unique to twisted arrays, and must be considered when finding solutions to Eq. (5.5) (See Appendix).

5.3 Wave Properties of Transverse Twisted Arrays

We discuss the properties of different traveling wave modes by considering first the special case of particles arranged such that two principal axes of $\boldsymbol{\alpha}$ are transverse to the array axis with corresponding principal values $\alpha_{xx} \neq \alpha_{yy}$, as shown in Fig. 5-1(b), where α_{xx} and α_{yy} are the polarizability constants of a particle along the principal axes transverse to the array. In this case the longitudinal traveling waves are independent of the transverse waves, and are not affected by the sequential rotation. To simplify the analysis the longitudinal waves will be ignored, and the z component of all fields set to zero.

A. Dispersion Equations and Modal Fields

To find the dispersion relations of transverse twisted arrays we first note that both the periodic Green's function $\mathbf{G}(\mathbf{0}, L, k_0, k_{z0})$ and the single source Green's function $\mathbf{G}_0(\mathbf{0}, k_0)$ are diagonal matrices with $G_{xx} = G_{yy} \equiv G$ and $G_{0xx} = G_{0yy} \equiv G_0$ respectively. The dispersion equation (5.5) then reduces to

$$\begin{vmatrix} (G^+ + G^-) - 2G_0 - 2/\alpha_{xx} & i(G^+ - G^-) \\ -i(G^+ - G^-) & (G^+ + G^-) - 2G_0 - 2/\alpha_{yy} \end{vmatrix} = 0 \qquad (5.6)$$

This equation may be solved numerically (e.g. using Muller's method) for a given case of interest. Simulations reveal that it has two independent solutions: β^+, found near

$k_0 + \phi_0 / L$, and β^-, found close to $k_0 - \phi_0 / L$, which represent the wavenumbers of the two transverse modes. This is in direct contrast with non-twisted resonant arrays, for which solutions are typically found close to k_0. With the modal wavenumbers found, the dipole moment $\mathbf{p}_0$ characterizing each modal polarization vector may then be found up to a constant factor by solving $(\mathbf{G}_{twisted}(\mathbf{0}, L, \phi_0, k_0, \beta) - \mathbf{G}_0(\mathbf{0}, k_0) - \boldsymbol{\alpha}^{-1}) \cdot \mathbf{p}_0 = 0$. The resulting (linearly dependent) system of equations yields the ratio of the transverse components of $\mathbf{p}_0$ for a given mode:

$$\frac{p_{x0}}{p_{y0}} = \frac{i(G^+ - G^-)}{2/\alpha_{xx} + 2G_0 - (G^+ + G^-)} \tag{5.7}$$

where each Green's function component is evaluated at $k_{z0} = \beta$ for the mode in question. The dipole moments of all other array elements may then be found by Eq. (5.2).

The modal transverse polarization wave may be expressed in an alternative form by rewriting Eq. (5.2) as

$$\mathbf{p}_n = \frac{p_{x0} + ip_{yo}}{2} \begin{pmatrix} 1 \\ -i \end{pmatrix} e^{i(\beta + \phi_0/L)nL} + \frac{p_{x0} - ip_{yo}}{2} \begin{pmatrix} 1 \\ i \end{pmatrix} e^{i(\beta - \phi_0/L)nL} \tag{5.8}$$

where k_{z0} has been replaced with β. The expressions in Eqs (5.2) and (5.8) highlight different interpretations of the traveling wave. The first shows β as the propagation wavenumber with respect to the fixed axes of the elements themselves, i.e. with respect to the twisted coordinate system. The second expression shows the fields as they propagate in an untwisted, laboratory reference frame. In the latter expression, the modal polarization wave is represented as a sum of right-hand circularly polarized (RCP) and

left-hand circularly polarized (LCP) components. These components have distinct propagation wavenumbers $\beta \pm \phi_0 / L$ that are relevant to the observable excitation and radiation behavior of the supported modes.

The radiation and propagation properties of the two independent β^+ and β^- modes become more apparent when studying the corresponding modal electric field. Recalling the periodic Green's function is diagonal for observation points on the array's axis (with identical xx and yy components $G(z\hat{\mathbf{z}}, L, k_0, \beta)$), the electric field on the array's axis can be given by the following expression

$$\mathbf{E}(z\hat{\mathbf{z}}) = G^+(z\hat{\mathbf{z}})(p_{x0} + ip_{yo})\begin{pmatrix} 1 \\ -i \end{pmatrix} + G^-(z\hat{\mathbf{z}})(p_{x0} - ip_{yo})\begin{pmatrix} 1 \\ i \end{pmatrix} \tag{5.9}$$

This equation shows that the axial electric field preserves the general polarization properties of the polarization vector as described by Eq. (5.8) and it comprises two components with distinct propagation wavenumbers . For observation points off the array's axis, the electric field can be given in terms of a Floquet expansion series, found in terms of $\mathbf{p}_0$ by evaluating Eq. (5.4) and using the Floquet series representation of the periodic Green's function (see Eq. (3.3))

$$\begin{aligned} \mathbf{E} = & \frac{p_{x0} + ip_{y0}}{2}\begin{pmatrix} k_0^2 + \partial_{xx}^2 - i\partial_{xy}^2 \\ -i(k_0^2 + \partial_{yy}^2 + i\partial_{xy}^2) \\ \partial_{zx}^2 - i\partial_{zy}^2 \end{pmatrix} \sum_{m=-\infty}^{\infty} H_0^{(1)}(k_{\rho m}^+ \rho) e^{i\left(\beta + (2\pi m + \phi_0)/L\right)z} \\ & + \frac{p_{x0} - ip_{y0}}{2}\begin{pmatrix} k_0^2 + \partial_{xx}^2 + i\partial_{xy}^2 \\ i(k_0^2 + \partial_{yy}^2 - i\partial_{xy}^2) \\ \partial_{zx}^2 + i\partial_{zy}^2 \end{pmatrix} \sum_{m=-\infty}^{\infty} H_0^{(1)}(k_{\rho m}^- \rho) e^{i\left(\beta + (2\pi m - \phi_0)/L\right)z} \end{aligned} \tag{5.10}$$

Here, the electric fields have been separated into two distinct wave components with longitudinal and transverse wavenumbers $\beta + (2\pi m \pm \phi_0)/L$ and $k_{\rho m}^{\pm} = \left[k_0^2 - \left(\beta + (2\pi m \pm \phi_0)/L\right)^2\right]^{1/2}$, respectively (m is an integer). Each wave component has a distinct phase velocity along the array and a distinct decay rate out of the array.

B. Propagation and Radiation Behavior

The expression for the electric field distribution (5.10) helps to elucidate the physical behavior of the traveling wave modes. Consider the case of dense arrays, for which L is small enough that no higher diffraction orders radiate. The fields corresponding to the β^+ mode consist of two wave components with propagation wavenumbers $\beta^+ \pm \phi_0/L > k_0$. In terms of the representation in Eq. (5.8) for the modal polarization, these wave components correspond to the LCP and RCP parts of the mode. The corresponding transverse wavenumbers $k_{\rho m}^{\pm}$ are imaginary, and from Eq. (5.10) the electric fields decay exponentially away from the array. This mode represents a slow wave that propagates without radiation loss. For dense arrays with no dissipation losses, β^+ is therefore a purely real number. Being a slow wave, this mode cannot be coupled to a far-field excitation, but it can be excited by a source with a strong evanescent spectrum.

The β^- mode, in contrast, is comprised of a component with wavenumber $\beta^- + \phi_0/L > k_0$, corresponding to an evanescent field, and a component for which $|\beta^- - \phi_0/L| < k_0$ in the case of small to moderate twist rates (i.e. reasonably small

$\phi_0 / k_0 L$), corresponding to a propagating field. The former and latter components are RCP and LCP components in the representation (5.8) for the modal polarization. In such cases this mode is a fast leaky-wave mode whose LCP component radiates out of the array. The radiated wave direction makes an angle θ_{rad} with the array axis that satisfies the phase matching condition $k_0 \cos(\theta_{rad}) = \mathrm{Re}\{\beta^-\} - \phi_0 / L$. This mode can be efficiently excited by a source field that is matched to either its RCP or LCP wave component. That is, an RCP evanescent wave can be matched to its slow, RCP wave component, or an LCP propagating wave can be matched to its fast, LCP component. The polarization of the radiated wave may be found from Eq. (5.10) at observation points far from the array at an observation angle θ_{rad} with the array axis. At this distance the propagating fields are assumed to dominate, so the twisted Green's function may be well approximated by neglecting G^+ in Eq. (5.10) and including only the zeroth diffraction order of G^- (i.e., the $m = 0$ term in Eq.(5.10)), which is responsible for far-field radiation in this case. The radiated field observed in the $x - z$ plane is given by

$$\mathbf{E}(\mathbf{r}) \sim (i\hat{\mathbf{x}}' + \cos\theta_{rad}\hat{\mathbf{y}}) \frac{e^{ik_0(\sin\theta_{rad}\rho + \cos\theta_{rad} z)}}{\sqrt{\rho}} \tag{5.11}$$

with the primed coordinates defined through $\hat{\mathbf{x}}' = \hat{\mathbf{x}}\cos(\theta_{rad}) - \hat{\mathbf{z}}\sin(\theta_{rad})$, $\hat{\mathbf{z}}' = \hat{\mathbf{x}}\sin(\theta_{rad}) + \hat{\mathbf{z}}\cos(\theta_{rad})$, $x' = x\cos\theta_{rad} + z\sin\theta_{rad}$. The vector field components are given with respect to the radiation direction. This wave is elliptically polarized with ellipticity $e = \sec(\theta_{rad})$. A twisted array may therefore act as an antenna whose radiation angle and polarization are determined by the twist rate ϕ_0 / L . We note that for

sufficiently large twist rates the propagation wavenumber may satisfy $\mathrm{Re}\{\beta^-\} - \phi_0/L < -k_0$. In this case the β^- mode is a slow wave and the array does not radiate at all.

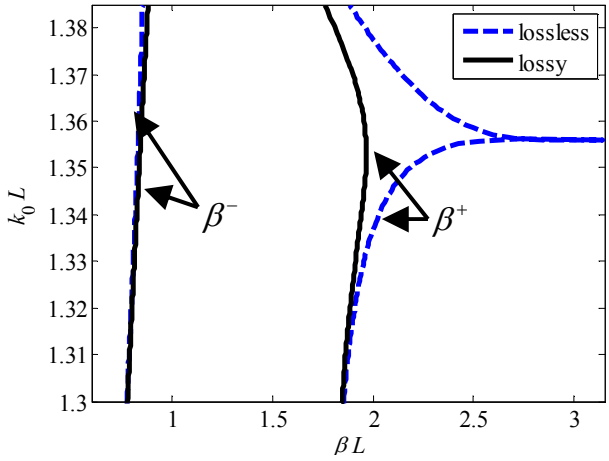

Fig. 5-2 Dispersion relations of an infinite, twisted array with spacing $L = 72\mathrm{nm}$ and rotation increment $\phi_0 = 30^\circ$. The array elements are gold prolate spheroids with major axes of length 33nm and minor axes of length 16.5nm.

To better characterize the modes we show the dispersion relations, found by tracking the mode wavenumbers over a range of values of the excitation wavenumber $k_0 = \omega/c$ for which waveguidance is supported. Fig. 5-2 shows the dispersion relations of the β^+ and β^- modes, found by solving Eq. (5.6) for an array of gold prolate spheroids with permittivity $\varepsilon_m(\omega)$, assumed to follow the Drude model with parameters given by [32]. The array is embedded in an infinite silicon dioxide medium. The dispersion of the two independent modes is shown for both realistic lossy particles and for lossless particles, for which case the Drude damping constant is set to zero. The array

has spacing $L = 72\text{nm}$, and twist angle $\phi_0 = 30^\circ$. Each spheroid has a major axis of length 33nm and minor axis of length 16.5nm, chosen to achieve both strong anisotropy and reasonably low loss. The long and short axes of each spheroid have plasmonic resonances at free-space wavelengths of 501nm and 298nm, respectively, and the range of k_0 is chosen close to but less than the resonance of the major axis at $k_0 L = 1.4$. The length of each spheroid is small enough compared to the wavelength to justify the dipole approximation for this structure [56].

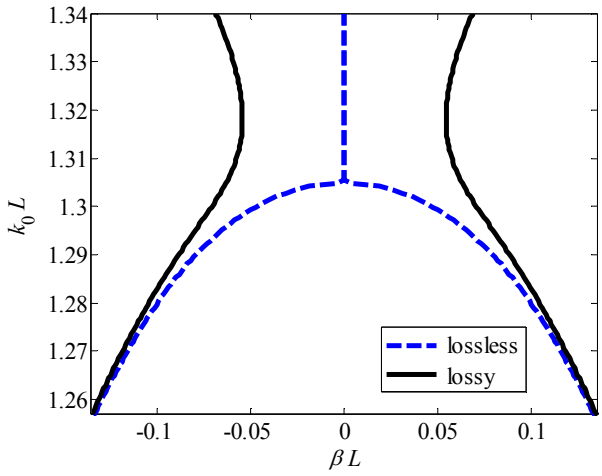

Fig. 5-3 Dispersion relations of the β^- mode of an infinite twisted array identical to that considered in Fig. 5-2, but with rotation increment $\phi_0 = 80^\circ$.

The dispersion relations of certain eigenmodes may exhibit stopbands of various types. These stopbands result from the coupling between modes that propagate in opposite directions. Mathematically, it occurs when two independent solutions of Eq. (5.6) approach the same point in the complex k_{z0} plane. In Fig. 5-2 the behavior of the β^+ mode results from interaction with the first diffraction order of the mode at $-\beta^+$,

found at $-\beta^+ + 2\pi/L$. In the lossless case, for which β^+ is purely real, this interaction results in a clear stop-band at $\beta^+ L = \pi$, where the wavenumbers of the two modes are equal. For the lossy case, in which β^+ has a nonzero imaginary part, this condition cannot be satisfied, though the strong coupling is clearly visible in the dispersion curves: as the two mode wavenumbers approach each other, each dispersion curve approaches the stopband point and then bends back away from it, indicating a change in group velocity and strong coupling (i.e. hybridization) with the counter-propagating diffraction mode. This type of stopband is unique to twisted structures with discrete periodicity. The β^- mode, in contrast, does not couple to the diffraction order at $-\beta^- + 2\pi/L$ except in the case of (often impractically) large spacings, for which waveguidance is not well supported. However, for large rotation rates it may couple directly to the mode with wavenumber $-\beta^-$, resulting in a stopband. Figure 5-3 shows the dispersion relations of the array considered before, but with $\phi_0 = 80^\circ$. For this large twist rate β^- is a purely real number in the lossless case, so a stopband forms at $\beta^- = 0$ where the two modes merge. It is noted that the dispersion relations in Figs. 5-2 and 5-3 are given for the wavenumber β with respect to the rotate coordinate system as discussed after Eq. (5.8). In the laboratory coordinate system the wavenumbers would appear shifted by ϕ_0/L. One result from here is that no open (i.e. broadside) stopbands are present with respect to the laboratory coordinate system. As is shown in Fig. 5-5, this property allows smoothly scanning the beams radiated by the twisted arrays through the broadside direction, thus eliminating the open stopband issue of typical leaky wave antennas. [57]

C. Finite Arrays

In this section we study propagation and radiation properties of twisted arrays composed of both nanoparticles at optical frequencies matching those considered for the infinite array analysis and (near) half-wave dipoles in the microwave regime. (The case of half-wave dipoles can be considered as a modification of a Yagi-Uda array with twisted rods). These results verify the properties of twisted arrays predicted by considering infinite arrays, characterize their source excited fields, and demonstrate that similar phenomena occur in different frequency ranges and for different arrays.

The nanoparticle array is excited by a waveguide excitation that consists of a periodic array of nanospheres connected to the twisted array at one end to form a continuous array, with a localized source placed at its opposite end. The nanosphere array has the same spacing as the twisted array, and each sphere has the same resonant wavelength as each ellipsoid's major axis. (An alternative source, such as a dielectric waveguide, could also be used to excite this array.) The periodic Green's function cannot be used to analyze this finite structure, so we use the dyadic Green's function for a single dipole source (found from Eqns. (2.6) and (2.5)) to model the array as collection of mutually interacting elements. A self-consistent matrix equation for each array element's polarization in response to the excitation field may then be set up and solved.

For the case of the microwave half-wave dipole array, the parameters are identical to the nanoparticle array (relative to the wavelength) to achieve the same general behavior, except that each microwave element is a perfect conducting rod of length $.38\lambda$ and radius $.005\lambda$, and is assumed to behave as a thin wire. The microwave array is excited by a pair of (near) half-wave dipole antenna sources at 300MHz, positioned at

right angles and phase shifted next to the left side of the array to create a circularly polarized excitation. The array response is modeled using an electric field integral equation solver in the thin wire approximation, using 11 basis functions per wire segment. [38].

Consider an array of 150 gold ellipsoids with the same array parameters as in the infinite case analyzed in the previous section. The source consists of 25 gold nanospheres and a dipole source with free-space wavelength $\lambda = 550\text{nm}$. This waveguide source creates an incident field with a propagation wavenumber slightly greater than the free-space wavenumber k_0. Inspection of Eqs. (5.8) and (5.9) reveals that an RCP waveguide source is therefore well matched to the β^- mode, whose RCP plane wave component has wavenumber $\beta^- + \phi_0/d$ close to k_0, while an LCP source is better matched to the β^+ mode.

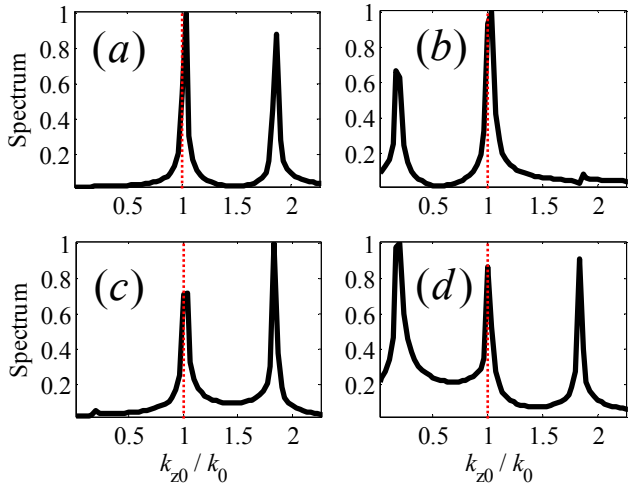

Fig. 5-4 Fourier spectrum of the transverse polarization component of a finite twisted array of gold prolate spheroids excited by a waveguide source with (a) LCP and (b) RCP polarization and wavelength 550nm. The same spectra for an array of half-wave dipoles in the microwave regime, excited by (c) LCP and (d) RCP antenna sources. The spectral peaks are spaced $2\phi_0/(k_0 L)$ apart. The array parameters are the same as in Fig. 5-2.

Taking the Fourier transform of a fixed, transverse polarization component of each spheroid element allows one to see the wavenumber content of the propagating fields. Fig 5-4 shows this spectrum for RCP and LCP source excitations, in which the dipole moment of the localized source is $\left(1,-i,0\right)$ and $\left(1,i,0\right)$, respectively. The response to a LCP source is two spectral peaks located near k_0 and $k_0+2\phi_0/L$, as predicted for the β^+ mode for infinite arrays. The same structure excited by a RCP source has a spectrum with peaks found near k_0 and $k_0-2\phi_0/L$, consistent with the β^- mode. (The small peak observed near $k_0+2\phi_0/L$ results from imperfect matching of the source to this mode.) In the microwave case, the spectrum is found by taking the Fourier transform of the transverse current moment at each rod's center. It is evident that the RCP excitation excites both modes in this case, most likely owing to the contribution of the near-field spectrum of the localized antenna source.

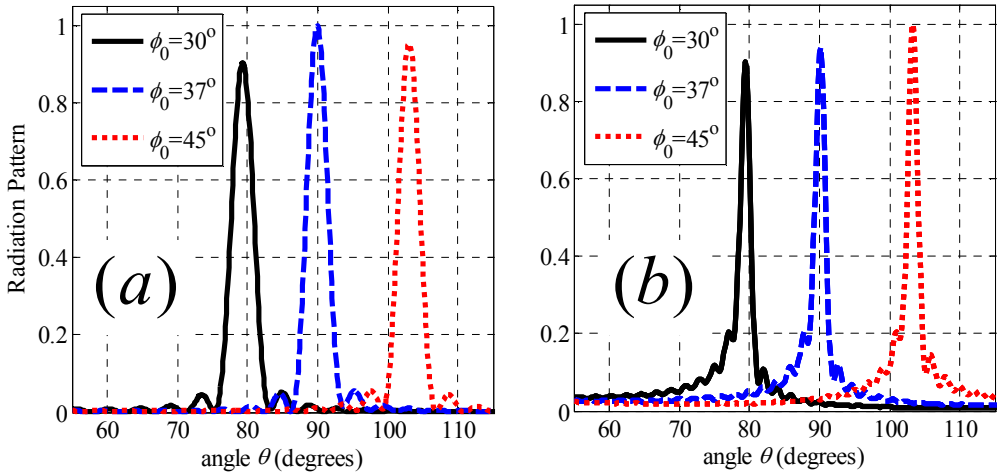

Fig. 5-5 (a) Radiation pattern resulting from the β^- mode of the finite twisted array of gold prolate spheroids considered in Fig. 5-4 with three distinct rotation increments. For $\phi_0 = 37^\circ$, the beam is radiated directly at broadside and is linearly polarized. For $\phi_0 = 30^\circ$ and $\phi_0 = 45^\circ$, the beams are directed in the forward and backward directions relative to the source, and are left and right handed elliptically polarized, respectively. (b) Radiation pattern from a twisted array of half-wave dipoles at 300MHz with the same rotation increments and spacing relative to the wavelength.

To verify the radiation properties we show in Fig. 5-5 the radiation pattern (i.e. the scattered far-field intensity as a function of the observation angle θ made with the array axis) for three values of the twist angle ϕ_0. For $\phi_0 = 37^\circ$, the beam is radiated directly at broadside and is linearly polarized. For $\phi_0 = 30^\circ$ and $\phi_0 = 45^\circ$, the beams are directed in the forward and backward directions relative to the source, and are left and right handed elliptically polarized, respectively, with ellipticity approximately given by $\sec(\theta_{rad})$. The peak directions are consistent with the predicted radiation angle for the β^- mode, given by $\theta_{rad} = \cos^{-1}\left(\mathrm{Re}\{\beta^-\}/k_0 - \phi_0/(k_0 L)\right)$. An important property is that the radiated beam does not exhibit an open stop-band behavior typical of many leaky wave

antennas, e.g. it does not change its width and shape as the radiation angle approaches 90^{o}. An open stopband behavior is also absent when frequency scanning the beam angle, which may be useful for applications in leaky wave structures.

The twisted arrays can also radiate end-fire beams, similar to Yagi-Uda antennas. Specifically, the β^{+} mode does not radiate at broadside, but still radiates into an endfire beam at $\theta = 0^{o}$. This radiation is similar to that from conventional Yagi-Uda antennas but it is of the LCP type (for the positive twist angle), similar to helical antennas. Figure 5-6 shows the endfire radiation from twisted nanoparticle and microwave arrays excited by LCP sources, confirming this behavior.

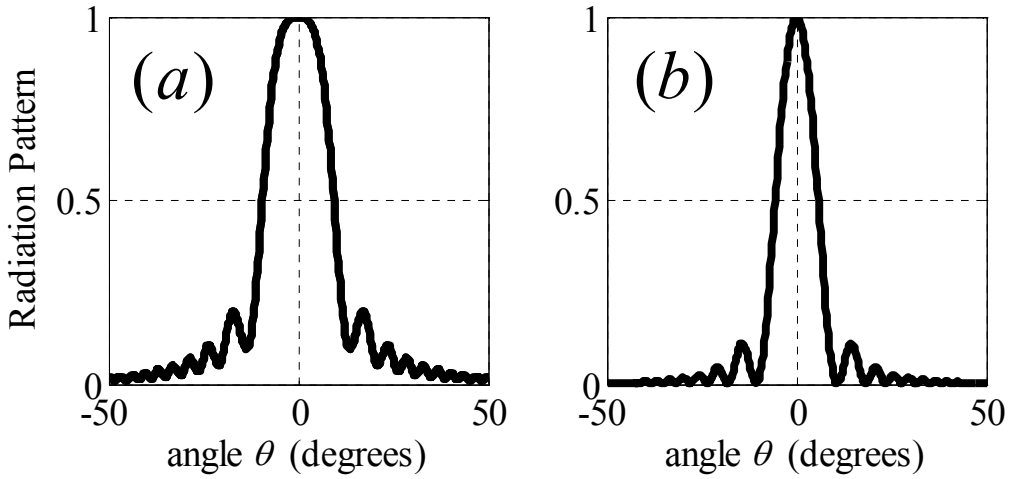

Fig. 5-6 Radiation pattern at endfire for the twisted (a) nanoparticle array (at $\lambda = 540$ nm) and (b) microwave array considered in Fig. 5-5, with LCP excitation.

5.4 Tilted Twisted Arrays

Consider now the more general case of nanoparticles oriented such that the principal axes of the polarizability tensor $\boldsymbol{\alpha}$ are not all parallel to or perpendicular to the array axis. In such cases, as shown in Fig. 5-1(c) (where the major axis of each ellipsoid

is "tilted" towards the array axis) the longitudinal mode is coupled to the transverse modes, so there now exist three independent modes that are coupled to the twist. Their wavenumbers may be found by solving Eq. (5.5), noting that the polarizability tensor $\boldsymbol{\alpha}$ must be appropriately rotated and is therefore no longer diagonal. The modal polarization wave now becomes

$$\mathbf{p}_n = \left(\frac{p_{x0} + ip_{yo}}{2} \begin{pmatrix} 1 \\ -i \\ 0 \end{pmatrix} e^{i\phi_0 n} + \frac{p_{x0} - ip_{yo}}{2} \begin{pmatrix} 1 \\ i \\ 0 \end{pmatrix} e^{-i\phi_0 n} + p_{z0} \begin{pmatrix} 0 \\ 0 \\ 1 \end{pmatrix} \right) e^{i\beta nL} \tag{5.12}$$

From Eq. (5.12) it is clear that the β^- and β^+ modes discussed in section 5.3 now have longitudinal components. However, their general radiation and polarization properties are otherwise largely unchanged. The third mode, mediated by the longitudinal component of the polarization, has a wavenumber $\beta^0 > k_0$ that is close to k_0, similar to a non-twisted resonant array. It is not, however, a slow wave; the propagation constant of its transverse LCP component generally satisfies $\left|\beta^0 - \phi_0 / L\right| < k_0$, and is therefore a leaky-wave mode that radiates at an angle satisfying $k_0 \cos(\theta^0_{rad}) = \mathrm{Re}\{\beta^0\} - \phi_0 / L$. An expression for the radiation from this component alone may be found from Eq. (5.4) by including only the longitudinal component of $\mathbf{p}_0$ and by neglecting all terms in the twisted Green's function except the zeroth diffraction orders of G_{xz}, G_{yz}, and G_{zz}. Unlike the radiation from the β^- mode, the radiation from the β^0 mode is linearly polarized.

To demonstrate the radiation properties of these twisted arrays, Fig. 5-7(a) shows the radiated electric field intensity for a finite array of gold prolate spheroids identical to that first considered in section 5.3C but with each spheroid "tilted" so that its major axis makes an angle of $\theta_0 = 85^\circ$ with respect to the array axis. Figure 5-7(b) shows similar results for the case of a tilted twisted array of half-wave dipoles in the microwave regime. The β^- mode radiates at the same angle as in the purely transverse case shown in Fig, 5-5, but there is an additional radiated beam that results from the β^0 mode. It is observed at an angle $\theta_{rad} = \cos^{-1}\left(\mathrm{Re}\{\beta^0\}/k_0 - \phi_0/(k_0 L)\right) = 53.2^\circ$. The angular separation between these two beams may be varied by changing the twist rate ϕ_0/L. This new radiation behavior results from the coupling of the formerly independent longitudinal mode to the transverse modes and their distinct propagation behavior.

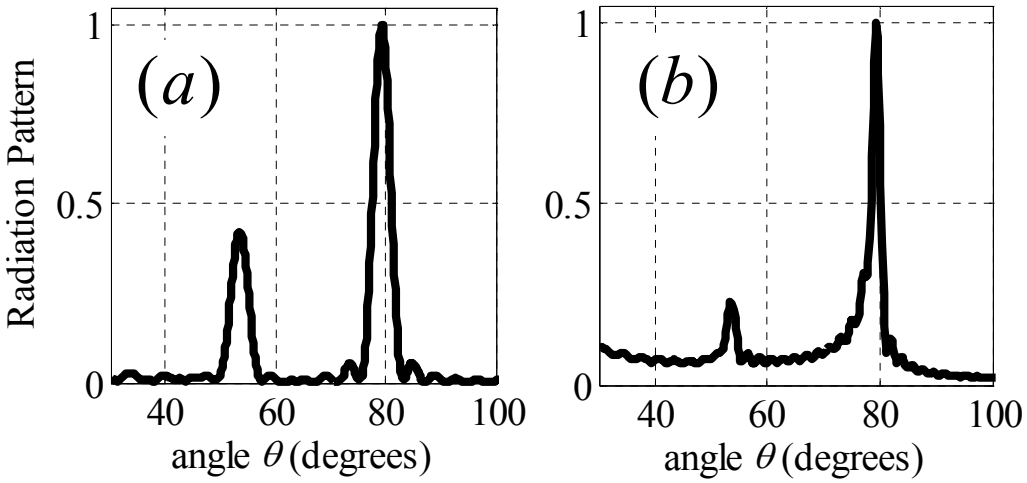

Fig. 5-7 Radiation pattern resulting from the β^- and β^0 modes of finite "tilted" twisted arrays of (a) gold prolate spheroids and (b) half-wave microwave dipoles excited by an RCP sources. In each case, the radiated beam on the left is linearly polarized, while that on the right is left handed elliptically polarized. The array parameters are as given in Fig. 5-4, but with tilt angle $\theta_0 = 85^\circ$ instead of 90°.

5.5 Extensions to Twisted Surface Structures

This section considers a twisted surface structure, consisting of many twisted linear arrays arranged parallel to each other to form a grid pattern. Consider a grid of particles oriented on the xy plane for which the (n,m) element, centered at $\mathbf{r}_{nm} = nL_x\hat{\mathbf{x}} + mL_y\hat{\mathbf{y}}$, is rotated about the x axis by an angle $n\phi_0$. (L_x and L_y denote the particle spacing in the x and y directions.) This planar structure extends the general features of twisted linear arrays to surface arrays, potentially enabling polarization control of surface waves supported by planarly layered media.

These "twisted surfaces" do not have the discrete rotation and translation symmetries as twisted arrays. A Green's function therefore cannot be formulated in the same manner of Eq. (5.4), and Floquet modes along the twist (x) direction will appear with spectral spacing determined not by the dense spacing L_x, but rather by the "long" period, encompassing enough particles along the twist direction such that the unit cell repeats itself in a cartesian reference frame. The additional Floquet modes introduced, however, are expected to contribute little to the overall field behavior in comparison to the β^+ and β^- modes identified for linear arrays in previous sections.

We simulate a twisted surface with parameters very similar to the linear arrays considered in figures 5-2 and 5-4: an array of 75×75 gold prolate spheroids, with major and minor axes of length 43nm and 21.5nm, embedded in a silicon dioxide medium. The twist increment in the x direction is $\phi_0 = 30^\circ$, and the spacing is $L_x = L_y = 120\text{nm}$. The structure is excited by a dipole source, placed at

$\mathbf{r}_{nm} = -L_x\hat{\mathbf{x}} + 37.5L_y\hat{\mathbf{y}}$ in order to generate traveling waves in the x direction, operating at free-space wavelength $\lambda = 550\text{nm}$. Figure 5-8 shows the spectrum of traveling waves generated by LCP and RCP dipole sources, found by taking the 2D Fourier transform of the z polarization component of each particle. The structure clearly supports wave modes similar to the β^+ and β^- modes discussed above. In both cases the source excites a cylindrical wave, and there are two dominant spectral peaks separated by $2\phi_0/(k_0L_x)$. This behavior suggests that the general features of twisted arrays can be extended to twisted surfaces, which could enable polarization control of surface waves.

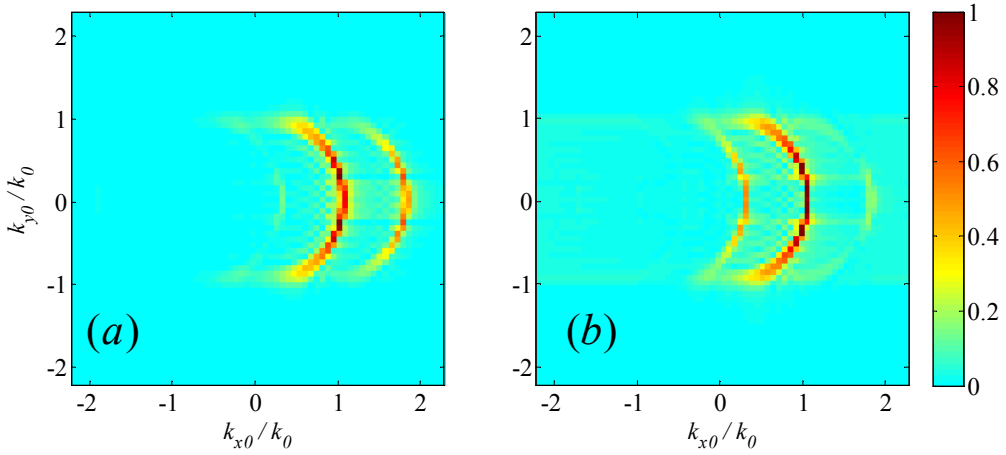

Fig. 5-8 Spectrum of traveling waves on a twisted array excited by a short dipole source with (a) LCP and (b) RCP polarization.

5.6 Conclusions

This chapter studies twisted resonant arrays characterized by a sequential rotation of each array element around the periodicity axis. Using the point dipole approximation, we derived a dyadic Green's function for these resonant array structures and used it to find the waveguiding modes and their dispersion. For densely spaced elements, we

identified two independent transverse modes with distinct polarization properties: one is a slow wave, while the other radiates for small to moderate twist rates. The angle and polarization of the resulting radiated beam are given in terms of the modal wavenumber. The dispersion relations of the transverse modes may exhibit stopbands, resulting from coupling to counter propagation modes, including higher diffraction orders. The open radiation stopbands typical of leaky wave antennas, however, are absent. By simulating a finite array we showed that these two modes are efficiently excited by circularly polarized sources of opposite handedness, and that the propagation and radiation properties agree with those predicted for an infinite array. Results were generalized to "tilted" twisted arrays, which have additional radiation mechanisms, and to twisted surfaces.

Twisted arrays could find applications as waveguides and radiators with tunable phase velocity, and as polarization-sensitive filters and couplers. Although the focus of this chapter is on resonant waveguiding structures, the general behavior found should characterize a general class of linear structures having both discrete and helical periodicities.

5.7 Appendix

As discussed in chapter 3, the periodic Green's function $\mathbf{G}(\mathbf{r}, L, k_0, k_{z0})$ has an infinite number of branch cuts in the complex k_{z0} plane that must be accounted for when solving Eq.(5.5). The Floquet modes have longitudinal wavenumbers $k_{zm} = k_{z0} + 2\pi m/L$ and transverse wavenumbers $k_{\rho m} = (k_0^2 - k_{zm}^2)^{1/2}$, having branch

cuts with branch points at $\pm k_0 + 2\pi m/L$. Recall that these branch cuts are necessarily found in all representations of the periodic Green's function. A set of dispersion relations can in general be defined on different Riemann sheets. However, only solutions on specific Riemann sheets that correspond to physically excitable modes should be considered.

For twisted arrays in which the particles have principal axes transverse to the array axis, Eq. (5.6) involves two Green's functions, $G^{\pm} = G_{xx}(\mathbf{0}, L, k_{z0} \pm \phi_0/L)$, whose linear phase shift factors differ by a translation of $2\phi_0/L$. The resulting determinant has branch points in the k_{z0} plane at $k_{zbm}^{+} = \pm k_0 + 2\pi m/L - \phi_0/L$ and $k_{zbm}^{-} = \pm k_0 + 2\pi m/L + \phi_0/L$, as shown in Fig. 5-9. For dense arrays with large twist rates (approximately $2\phi_0/L > k_0$), all solutions of Eq. (5.6) are found on the top Riemann sheet, on which $\mathrm{Im}\{(k_0^2 - \beta^2)^{1/2}\} < 0$. Fig. 5-9(a) shows, in the complex k_{z0} plane, the solutions $\pm\beta^{\pm}$ and branch cuts for the array considered in Fig. 5-3 (with twist rate $\phi_0 = 80^{\circ}$) at a free-space wavelength of $550\mathrm{nm}$. This array is characterized by a large rotation rate, and all of the traveling wave modes are slow waves that do not radiate. Note that in all the solutions are found close to the branch points. As the twist rate ϕ_0/L decreases, however, the two branch points on each side of the origin approach each other. At around $\phi_0/L \approx k_0$, the β^- and $-\beta^-$ modes become leaky-wave modes. For smaller twist rates (roughly $\phi_0/L < k_0/2$) β^- and $-\beta^-$ move to the bottom Riemann sheets

defined for the $m = 0$ branch cuts of G^+ and G^- respectively, while β^+ and $-\beta^+$ remain on the top Riemann sheet. This is the case in Fig. 5-9(b), which shows the branch cuts for the same infinite array analyzed in Fig. 5-2 but with twist angle $\phi_0 = 30^o$

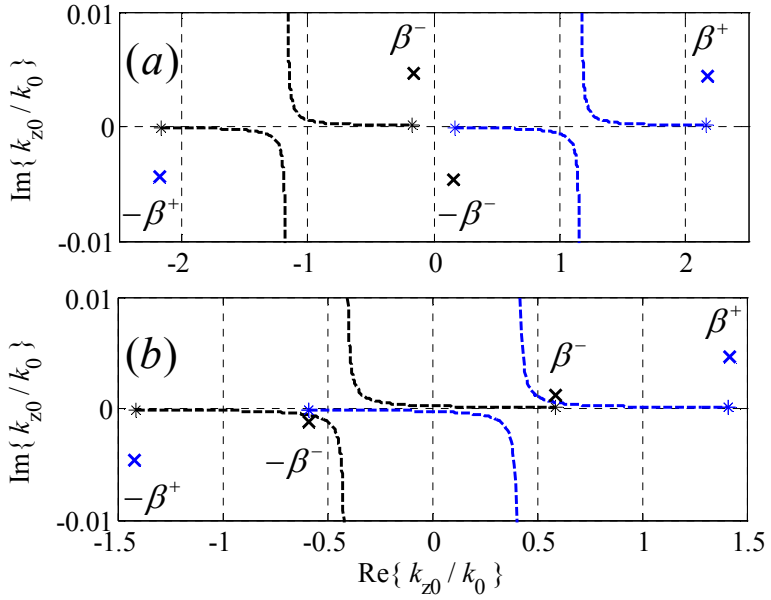

Fig. 5-9 Branch cuts and solutions of Eq. (5.6) in the complex k_{z0} plane for the infinite arrays considered in Fig. 5-2 and Fig. 5-3, corresponding to rotation increments (a) $\phi_0 = 30^o$ and (b) $\phi_0 = 80^o$ respectively. (To enhance visibility, the branch cuts are plotted for a value of k_0 with very small imaginary part.)

For the case of tilted twisted arrays, there are three independent solutions in the complex k_{z0} plane. In addition to the branch cuts described above for the transverse twisted array, there are now branch cuts with branch points at $\pm k_0 + 2\pi m/L$, resulting from the presence of the periodic Green's function component G_{zz} in Eq. (5.5). The details of which Riemann sheets each solution is found on are somewhat involved, and

may depend on both the twist rate ϕ_0 / L and the tilt angle θ_0. This discussion is therefore omitted.

5.8 Acknowledgements

The text of Chapter 5 is, in part, a reprint of the material as it appears in the following publication: Derek Van Orden and Vitaliy Lomakin, "Fundamental electromagnetic properties of twisted linear arrays", IEEE Transactions on Antennas and Propagation, Vol 59, 2824-2833 (2011). The dissertation author was the primary researcher and the co-author listed in this publication directed and supervised the research which forms the basis for this chapter.

Chapter 6 Conclusion

This dissertation presents Green's function formulations for the study of the propagation and radiation properties of periodic electromagnetic structures. Chapter 3 introduced a new spectral representation for the free-space periodic Green's function for linear arrays. For observation points near the array axis, it offers significant advantages in computation speed over existing acceleration schemes, and also lends itself to asymptotic expressions for the fields near the array axis. Chapter 4 extends this transverse spectral approach to the case of linear arrays near surfaces. The resulting representation is the only one known to achieve high accuracy on or near the surface interface and periodicity axis. Like the free-space Green's function, it is expressed in terms of distinct field types characterizing the system, including guided waves supported by the surface and Floquet modes. In addition to fast evaluation, this representation allows a physical understanding of the ways in which different field types couple to each other. Both of these Green's function representations can accelerate the computational simulation of periodic systems using the Method of Moments. Chapter 5 introduced a new class of periodic system, characterized by discrete helical periodicity, and derived a Green's function for the case of small scatterers. This structure displays many interesting properties, and supports two transverse modes that are easily excited by circularly polarized sources with different handedness. One is a slow, bound wave, while the other can radiate into elliptically polarized beams at broadside and circularly polarized beams at endfire.

The applications of this work are numerous. The free-space periodic Green's function representation, on its own, can accelerate the analysis of any linear periodic

system in electromagnetics, including gratings, waveguiding structures, and antennas. It is furthermore an important component to solving for the complete Green's function in other environments, such as near surfaces or in waveguides. The Green's function for a periodic array on a surface is a particularly important case, as many periodic structures are manufactured on dielectric substrates, such as printed circuit boards and silicon wafers. Because such systems are compact and inexpensive, they are frequently encountered in many applications of periodic structures, and are frequently found in microwave and light-wave circuits. The physical understanding facilitated by this representation could be helpful in design consideration for all of these classes of structures. Finally, twisted arrays could offer polarization selectivity to any of the periodic devices mentioned above. This could be useful in designing new types of filters and couplers for the transmission of electromagnetic signals. It also has applications to leaky-wave antennas, for which full tunability of the radiated beam at broadside remains a fundamental problem. The basic functionalities of twisted arrays could be realized by adding a discrete periodicity to any type of helical structure, such as helical antennas and chiral optical fibers.

References

[1] B. A. Munk and G. A. Burrell, "Plane-wave expansion for arrays of arbitrarily oriented piecewise linear elements and its application in determining the impedance of a single linear antenna in a lossy halfspace," *IEEE transactions on antennas and propagation,* vol. 27, pp. 331-343, 1979.

[2] C. Balanis, *Antenna Theory: Analysis and Design*, 3rd ed.: Wiley, 2005.

[3] W. H. Weber and G. W. Ford, "Propagation of optical excitations by dipolar interactions in metal nanoparticle chains," *Physical Review B,* vol. 70, pp. 125429-1, 2004.

[4] A. Alù and N. Engheta, "Theory of linear chains of metamaterial/plasmonic particles as subdiffraction optical nanotransmission lines," *Physical Review B,* vol. 74, p. 205436, 2006.

[5] M. Quinten, A. Leitner, J. R. Krenn, and F. R. Aussenegg., "Electromagnetic energy transport via linear chains of silver nanoparticles," *Optics Letters,* vol. 23, pp. 1331-1, 1998.

[6] M. L. Brongersma, J.W. Hartman, and H.A. Atwater, "Electromagnetic energy transfer and switching in nanoparticle chain arrays below the diffraction limit," *Physical Review B (Condensed Matter),* vol. 62, pp. 16356-9, 2000.

[7] D. Van Orden, Y. Fainman, and V. Lomakin , "Optical waves on nanoparticle chains coupled with surfaces," *Optics Letters,* vol. 34, pp. 422-424, May 2009.

[8] V. Lomakin, M. Lu, and E. Michielssen, "Optical wave properties of nano-particle chains coupled with a metal surface," *Optics Express,* vol. 15, pp. 11827-11842, 2007.

[9] S. A. Tretyakov, S. Maslovski, and P.A. Belov, "An analytical model of metamaterials based on loaded wire dipoles," *IEEE transactions on antennas and propagation,* vol. 51, pp. 2652 - 2658 2003.

[10] L. B. Felsen and N. Marcuvitz, *Radiation and Scattering of Waves*. Englewood Cliffs, N.J.: Prentice-Hall, 1973.

[11] A. F. Peterson, S.L. Ray, and R. Mittra, *Computational Methods for Electromagnetics*. Piscataway, N.J.: IEEE Press, 1997.

[12] A. W. Mathis and A. F. Peterson, "A comparison of acceleration procedures for the two-dimensional periodic Green's function," *IEEE Trans. Antennas Propagat.,* vol. 44, pp. 567-571, 1996.

[13] S. Singh and R. Singh, "Efficient computation of the free-space periodic Green's functions," *IEEE Trans. Microwave Theory Tech.,* vol. 39, pp. 1226-1229, 1991.

[14] P. Wynn, "On a device for computing the e_m(S_n) transformation," *Math Tables Aids Comput.,* vol. 10, pp. 90-96, 1956.

[15] A. L. Fructos*,* R.R. Bois, F. Mesa, and F. Medina, "Application of the Kummer's transformation to the efficient computation of 3-D Green's function with one-dimensional periodicity in homogeneous media," in *URSI Nat. Radio Sci. Meeting*, San Diego (CA), 2008.

[16] G. Valerio*,* P. Baccarellli, P. Burghignoli, and A. Galli, "Comparative Analysis of Acceleration Techniques for 2-D and 3-D Green's Functions in Periodic Structures Along One and Two Directions," *IEEE Trans. Antennas and Propagat.,* vol. 55, pp. 1630 - 1643 2007.

[17] M. E. Veysoglu*,*E. Murat, H.A. Yueh, R.T. Shin, and J.A. Kong, "Polarimetric passive remote sensing of periodic surfaces," *J. Electromag. Waves Appl. ,* vol. 5, pp. 267-280, 1991.

[18] H. Rogier, "New series expansions for the 3-D Green's function of multilayered media with 1-D periodicity based on perfectly matched layers," *IEEE Trans. Microwave Theory Tech.,* vol. 55, pp. 1730-1738, 2007.

[19] H. Rogier and D. D. Zutter, "A fast converging series expansion for the 2-D periodic Green's function based on perfectly matched Layers," *IEEE Trans. Microwave Theory Tech.,* vol. 52, pp. 1199-1206, 2004.

[20] P. P. Ewald, "Die berechnung optischer und elektrostatischen gitterpotentiale," *Ann. der Phys. ,* vol. 64, pp. 253-287, 1921.

[21] K. E. Jordan*,*G.R. Richter, and P. Sheng, "An efficient numerical evaluation of the Green's function for the Helmholtz operator on periodic structures," *J. Comp. Phys.,* vol. 63, pp. 222-235, 1986.

[22] V. G. Papanicolaou, "Ewald's method revisited: rapidly convergent series representations of certain Green's functions," *J. Comp. Anal. Appl.,* vol. 1, pp. 105-114, 1999.

[23] A. Kustepely and A. Q. Martin, "On the splitting parameter in the Ewald method," *IEEE Microwave Guided Wave Lett.,* vol. 10, pp. 168-170, 2000.

[24] S. Oroskar,D.R. Jackson, and D.R. Wilton , "Efficient Computation of the 2D periodic Green's function using the Ewald method," *J. Comp. Phys.,* vol. 219, pp. 899-911, 2006.

[25] F. Capolino*, et al.*, "Efficient computation of the 2D Green's function for 1D periodic structures using the Ewald method," *IEEE Trans. Antennas Propagat.,* vol. 53, pp. 2977-2984, 2005.

[26] F. Capolino*,* D.R. Wilton, and W.A. Johnson, "Efficient computation of the 3D Green's function for the Helmholtz operator for a linear array of point sources using the Ewald method," *J. Comp. Phys. ,* vol. 223, pp. 250–261, 2007.

[27] G. Kobidze*,* B. Shanker, and D.P. Nyquist, "Efficient integral-equation-based method for accurate analysis of scattering from periodically arranged nanostructures," *Phys. Rev. E,* vol. 72, p. 056702, 2005.

[28] I. Stevanovic and J. R. Mosig, "Periodic Green's function for skewed 3-D lattices using the Ewald transformation," *Microwaves Optical Tech. Lett.,* vol. 49, pp. 1353-1357, 2007.

[29] F. T. Celepcikay*,* D.R. Wilton, D.R. Jackson, and F. Capolino, "Choosing splitting parameters and summation limits in the numerical evaluation of 1-D and 2-D periodic Green's functions using the Ewald method," *Radio Sci.,* vol. in press, 2008.

[30] W. C. Chew, *Waves and fields in inhomogeneous media*. New York: IEEE Press, 1995.

[31] I. S. Gradshteyn and I. M. Ryzhik, *Table of Integrals, Series, and Products*. San Diego, CA: Academic Press, 2000.

[32] E. D. Palik, *Handbook of Optical Constants of Solids*: Academic Press, 1998.

[33] S. Li*,* D. Van Orden, and V. Lomakin, "Fast Periodic Interpolation Method for Periodic Unit Cell Problems," *IEEE transactions on antennas and propagation,* vol. 58, pp. 4005-4014, 2010.

[34] R. E. Collin and F. J. Zucker, *Antenna Theory: Part 2*: McGraw-Hill Education 1969.

[35] A. A. Olinear and R. C. Johnson, *Leaky-Wave Antennas, Antenna Engineering Handbook*, 3rd ed.: New York: Mcgraw-Hill, 1993.

[36] B. Munk, *Frequency Selective Surfaces: Theory and Design*. New York: John Wiley and Sons, Inc., 2000.

[37] N. Engheta and R. Ziolkowski, *Metamaterials: Physics and Engineering Explorations*. Piscataway, NJ: Wiley-IEEE press, 2006.

[38] A. F. Peterson*, et al.*, *Computational Methods for Electromagnetics*. New York: IEEE Press, 1998.

[39] H. Rogier, "New Series Expansions for the 3-D Green's Function of Multilayered Media With 1-D Periodicity Based on Perfectly Matched Layers," *IEEE transactions on Microwave Theory and Techniques,* vol. 55, pp. 1730-1738, 2007.

[40] G. Valerio*,* D.R. Jackson, and A. Galli, "The Array Scanning Method for the Computation of 1D-Periodic 3D Green's Functions in Stratified Media," in *IEEE AP-S URSI*, Toronto, 2010.

[41] M. I. Aksun and R. Mittra, "Derivation of closed-form Green's functions for a general microstrip geometry," *IEEE transactions on Microwave Theory Tech,* vol. 40, pp. 2055-2062, 1992.

[42] D. Van Orden and V. Lomakin, "Rapidly convergent representations for 2D and 3D Green's functions for a linear periodic array of dipole sources," *IEEE Trans. Ant. Propagat.,* vol. 57, pp. 1973-1984, July 2009 2009.

[43] S. Podilchak*,* A.P. Freundorfer, and Y. Antar, "Planar Leaky-Wave Antenna Designs Offering Conical-Sector Beam Scanning and Broadside Radiation Using Surface-Wave Launchers," *IEEE antennas and wireless propagation letters,* vol. 7, pp. 155-158, 2008.

[44] S. Chandrasekhar, *Liquid Crystals*. Cambridge: Cambridge University Press, 1977, 1994.

[45] C. Oldano*,* E. Miraldi, and P. Taverna Valabrega, "Dispersion relation for propagation of light in cholesteric liquid crystals," *Physical Review A,* vol. 27, p. 32913299, 1983.

[46] H. L. Ong, "Wave propagation in cholesteric and chiral smectic-C liquid crystals: Exact and generalized geometrical-optics-approximation solutions," *Physical Review A,* vol. 37, pp. 3520-3529, 1987.

[47] A. Papakostas, A. Potts, D.M. Bagnall, S.L. Prosvirnin, H.J. Coles, and N.I. Zheludev, "Optical Manifestations of Planar Chirality," *Physical Review Letters,* vol. 90, 2003.

[48] B. Bai, Y. Svirko, J. Turunen, and T. Vallius, "Optical activity in planar chiral metamaterials: Theoretical study," *Physical Review A,* vol. 76, pp. 023811-1, 2007.

[49] G. Shvets, "Optical polarizer/isolater based on a rectangular waveguide with helical grooves," *Applied Physics Letters,* vol. 89, p. 141127, 2006.

[50] I. V. Semchenko, S.A. Khakhomov, S.A.Tretyakov, and A.H. Sihvola, "Microwave analogy of optical properties of cholesteric liquid crystals with local chirality under normal incidence of waves," *J. Phys. D: Appl. Phys.,* vol. 32, pp. 3222-3226, 1999.

[51] R. Mittra, "Wave Propagation on Helices," *IEEE transactions on antennas and propagation,* vol. AP-11, pp. 585-586, 1963.

[52] N. Engheta and P. Pelet, "Modes in Chirowaveguides," *Optics Letters,* vol. 14, pp. 593-595, 1989.

[53] V. I. Kopp, V.M. Churikov, J. Singer, N. Chao, D. Neugroschl, and A.Z. Genack, "Chiral Fiber Gratings," *Science,* vol. 305, pp. 74-75, 2004.

[54] A. Z. Genack, V.I. Kopp, V.M. Churikov, J. Singer, N. Chao, and D.A. Neugroschl, "Chiral fiber Bragg gratings," in *Proceedings of the SPIE-The Inernational Society for Optical Engineering*, Denver, CO, USA, 2004, pp. 57-64.

[55] G. Shvets,S. Trendafilov, V.I. Kopp, D.A. Neugroschl, and A.Z. Genack., "Polarization properties of chiral fiber gratings," *J. Opt. A: Pure Appl. Opt.,* vol. 11, p. 074007, 2009.

[56] A. Govyadinov and V. Markel, "From slow to superluminal propagation: Dispersive properties of surface plasmon polaritons in linear chains of metallic nanospheroids," *Physical Review B,* vol. 78, pp. 0354031-12, 2008.

[57] P. Baccarelli, S. Paulotto, D.R. Jackson, and A.A. Oliner, "A New Brillouin Dispersion Diagram for 1-D Periodic Printed Structures," *IEEE transactions on Microwave Theory and Techniques,* vol. 55, pp. 1484 - 1495 2007.